UNIVERSITY OF
LIVERPOOL

Development, impact and longevity of fractures in magmatic, volcanic and geothermal systems

Thesis submitted in accordance with the requirements of the University of Liverpool for the degree of Doctor of Philosophy

by

Anthony Lucien Henri Lamur

March 2018

"Quand on file une histoire à un copiste pour qu'il en fasse trois exemplaires, que ça va lui prendre trois mois, et qu'ça va couter la peau des fesses, c'est pas pour raconter le temps qu'il fait ou c'que vous avez bouffé à midi, hein ! Il faut qu'ça pète !"
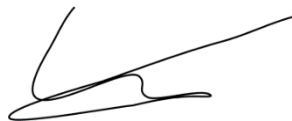
Arthur, *Kaamelot, Livre III*

Declaration of authorship

I, Anthony Lamur, declare that this thesis entitled "Development, impact and longevity of fractures in geothermal and volcanic systems" and the work presented in it are my own. I confirm that:

- This thesis was completed as part of a research degree at the University of Liverpool;
- The material contained in this thesis has not been presented, nor is currently being presented, either wholly or in parts, for any other degree or qualifications;
- Where I have consulted published studies, this has always been clearly referenced;
- Where the work was part of a collaborative effort, I have made clear what others have done and what I have contributed myself;
- Parts of this thesis have been submitted for publication or have been published as:
  - Lamur, A., Kendrick, J. E., Eggertsson, G. H., Wall, R. J., Ashworth, J. D., and Lavallée, Y., 2017, The permeability of fractured rocks in pressurised volcanic and geothermal systems: Nature Scientific Reports.
  - Lamur, A., Lavallée Y., Iddon, F. E., Hornby, A. J., Kendrick, J. E., Von Aulock, F. W., Wadsworth, F. B., accepted, Disclosing the temperature of columnar jointing in lavas: Nature Communications.
  - Lamur, A., Kendrick, J. E., Wadsworth, F. B., Lavallée, Y., submitted, Timescales of fracture healing and strength recovery in magmatic liquids: Geology.

Signed:

Anthony Lamur

13th March 2018

Abstract

The migration of fluids in the Earth's crust embodies the last stage of the internal heat release of our planet. Either spectacularly expressed at the surface through volcanic activity, or more subtly as internal hydrothermal circulation, this phenomenon involves the upwards motion of fluids and magmas that contribute to more efficient heat transfer. On one hand, volcanic eruptions result from the movement of buoyant magmatic liquids towards the surface. On their way up, these magmas cool down, crystallise and upon decompression, build up an internal pressure that dictate the eruptive style: Effusive when the internal pressure is released as it builds up; explosive when the internal pressure accumulates until it is able to fracture the magma. In nature, the shift from effusive to explosive activity is often periodic, reflecting cycles of pressure accumulation and relaxation in the conduit. On the other hand, hydrothermal circulation results from the infiltration of water, of meteoric or magmatic origin, into the rocks making up the crust. Higher temperatures at depth and/ or due to the presence of a magmatic body, trigger the formation of convective cells in which chilled, denser water percolates downwards then heats up, losing density before moving back upwards. Importantly, the circulation of both hydrothermal fluids and magmatic liquids is controlled by the presence of fractures in the crust and the permeability of the surrounding rocks.

In this thesis, I first investigate how fractures affect the localisation of fluids in fractured porous rocks through permeability measurements, both at atmospheric pressure and at shallow confining conditions (<30 MPa; ~1 km depth). I demonstrate that the impact of fractures is greater at lower porosities as the permeability is greatly increased. In more porous rocks, higher pore connectivity means that macro-fractures affect the permeability less significantly, as at least some of the fluid flows through the pre-existing connected porous network. I further demonstrate that, during confinement, most of the mechanical closure occurs at shallow conditions (<5 MPa; ~200m depth) for the porosity range tested. In addition, I show that mechanically shutting a fracture does not seal the permeable pathways, and that the fractured system is unable to retrieve the same permeability as the intact system. I then develop an analytical solution for the permeability of variably porous, fractured systems as a function of depth before numerically solving it. I complement this work with two "case studies" in which tensile fractures form and open or heal, and link this to the system permeability evolution through time and the implications for magmatic, volcanic and geothermal systems.

In the first scenario, tensile fractures open in a cooling magmatic body to form columnar joints in a basalt. Because the temperature at which cooling joints form remains elusive, causing a lingering scientific debate, I develop a novel type of mechanical testing and show for the first time that, in basaltic systems, these macro-fractures form purely in the elastic regime. This is further supported by the use of the rock's thermo-mechanical characteristics (namely thermal expansion and tensile strength) to model the tensile stress build-up upon cooling and, once formed, the evolution of the fracture width between two columns. Applying the analytical solution for fractured systems permeability defined earlier, I further model the permeability evolution of a columnar jointing magmatic body, important for the understanding of fluid migration during drilling close to magmatic chambers.

Finally, in magmas, the entrapment of exsolving gases, during ascent, force the accumulation of stress in the liquid, building pore pressure and potentially resulting in magmatic fragmentation. Consequently, the accumulated stresses can then be dissipated at times longer than the relaxation timescale of the melt, allowing fractures to heal and the system to recover strength lose permeability. Using synthetic glasses in a newly designed experimental setup, I show that the time required to start the healing process is proportional to the relaxation timescale of the melt. I further demonstrate that the kinetics of fracture healing involve two distinct stages. The first stage sees the fracture walls viscously deforming to dissipate excessive energy along the fracture plane (wetting regime), while the second stage consists of the diffusive exchange of elements across the fracture interface (diffusive regime). I finally surmise that the cyclic activity of persistently active silicic volcanoes could be explained by dynamic permeability and strength variations of material due to repeating fracture and healing cycles.

Overall, I show that the development and longevity of fractures have significant impacts on the localisation of fluid flow, highlighting that fractures significantly contribute to the development of anisotropy in magmatic, volcanic and geothermal environments. A better understanding of the longevity of fractures in these systems is of prime importance in the mitigation of hazards associated to volcanic eruptions, but also in the development of cheaper, more efficient geothermal energy.

Résumé

Le transport de fluides dans la croute terrestre constitue la dernière étape du refroidissement interne de notre planète. Que ce phénomène soit exprimé spectaculairement à la surface sous forme d'éruptions volcaniques, ou plus subtilement à travers la circulation internes de fluides hydrothermaux, il nécessite la migration de magmas ou de fluides vers la surface, contribuant ainsi à une perte de chaleur plus efficace. D'un côté, les éruptions volcaniques sont générées par le transfert de liquides magmatiques, moins denses que les roches encaissantes, vers la surface. En remontant, ces liquides refroidissent, cristallisent et, durant leur décompression, relâchent leurs gaz, générant une surpression qui gouverne le style éruptif : Éruption effusive quand la surpression est relâchée aussi rapidement qu'elle ne se créée ; éruption explosive quand la pression interne s'accumule au point de pouvoir fracturer le magma. Souvent, le style éruptif est caractérisé par un changement continu et périodique d'activité, reflétant l'accumulation cyclique de surpression au sein du conduit volcanique. D'autre part, la circulation de fluides hydrothermaux provient de l'infiltration de fluides, d'origine météorique ou magmatique, dans les roches de la croute terrestre. Durant leur infiltration, la température de ces fluides augmente sous l'effet du gradient géothermique, ou de par la présence d'un réservoir magmatique en profondeur. Ce changement de température génère la formation de cellules convectives où les fluides froids et denses percolent vers le bas, et les fluides chauds, moins denses migrent vers la surface. Principalement, la migration de ces fluides hydrothermaux, ou liquides magmatique est contrôlée par la perméabilité des roches et la présence de fractures.

Dans cette thèse, je m'intéresse premièrement à l'impact des fractures sur la localisation de l'écoulement fluide à travers une variété de roches volcaniques. Pour ceci, je mesure leur perméabilité à pression atmosphérique ainsi qu'à faible confinement (<30 MPa ; ~1km de profondeur). Je montre que l'impact des fractures est accru dans les roches ayant une porosité faible. Dans les roches plus poreuses, la connectivité des pores augmente et contrôle une partie de l'écoulement fluide, réduisant ainsi l'impact des fractures sur la perméabilité. Je démontre ensuite que la fermeture mécanique d'une fracture, se produit principalement à des conditions de confinement très faibles (<5 MPa ; ~200 m de profondeur). Après quoi je développe une solution analytique contraignant l'évolution de la perméabilité, dans des systèmes fracturés, avec la profondeur, avant de résoudre numériquement ce modèle mathématique. Je couple ensuite ce travail à deux « cas d'études » dans lesquels des fractures en tension (ou fentes)

s'ouvrent ou se ressoudent, avant de modéliser l'évolution de la perméabilité avec le temps de systèmes contenant ces fentes.

Dans le premier cas, les fentes s'ouvrent pendant le refroidissement d'un réservoir magmatique pour former des orgues basaltiques. Depuis plusieurs années, la température à laquelle se forment ces joints columnaires reste indéterminée, générant un débat scientifique animé. Dans cette thèse je développe une nouvelle approche expérimentale afin de contraindre une fenêtre de température pour leur formation. Je montre pour la première fois que les orgues basaltiques se forment dans un régime purement élastique. De plus, je supporte ce résultat avec un modèle thermomécanique (utilisant la force maximum en tension et l'expansion thermique des roches) qui détermine l'accumulation de contrainte en tension, ainsi que l'évolution de l'ouverture d'une fracture entre deux colonnes pendant le refroidissement. Finalement, en appliquant la solution analytique pour la perméabilité d'un système fracturé, défini plus tôt, je calcule l'évolution de la perméabilité d'un réservoir magmatique développant des orgues basaltiques, pendant le refroidissement.

Dans le second cas, les fractures, ouvertes par l'accumulation de contraintes dans un liquide magmatique, peuvent se ressouder quand le temps de relaxation du liquide est dépassé. Afin d'étudier ce processus, je développe une nouvelle approche expérimentale et démontre que la soudure ne commence qu'après un temps caractéristique, proportionnel au temps de relaxation du liquide. J'établis ensuite que la cinétique du phénomène est constitué de deux régimes distincts. La première étape voit la déformation visqueuse des parois de la fracture l'une contre l'autre (régime de mouillage), alors que la seconde partie voit l'échange d'éléments par diffusion de part et d'autre du plan de fracture (régime de diffusion). Je conclus finalement que l'activité cyclique souvent observée sur certains volcans siliciques peut être expliquée par la variation dynamique de la perméabilité et de la cohésion du système à travers l'ouverture et la soudure répétitive de ces fractures.

De manière générale, je montre que le développement et la longévité des fractures a un impact sur la localisation de l'écoulement fluide, montrant ainsi que ces fractures contribuent largement au développement de l'anisotropie des systèmes magmatiques, volcaniques et géothermiques. Ainsi, une meilleure compréhension de la longévité des fractures dans ces environnements est primordiale dans la réduction des aléas liés au phénomène volcanique, et est toute aussi importante pour le développement de centrales géothermiques plus rentables, réduisant ainsi le coût de l'énergie géothermique.

Contents

x

List of figures

Chapter 4

Chapter 5

Chapter 6

Chapter 7

List of tables

Acknowledgements

"But… There are no volcanoes in Liverpool": Relatively true statement that comes my way relatively often, and it's also relatively true that I was, at first, rather doubtful about coming to Liverpool to study experimental volcanology. However, the group I met and got to work with is definitely the best environment I could have hoped for.

The first, and special, mention has to go to my mentor, Yan Lavallée whose multilinguism has suggested the next few lines: Yan, I truly pense que tu es un amazing scientist, sometimes turning into something like an enchanteur (although bien meilleur que Merlin dans Kaamelot), always able de me motiver, même dans mes pires moments de doutes. I cannot thank you enough pour ton aide and your friendship, but also, and most certainly, for your guidance et ta supervision. I wish that I will be able de collaborer avec toi pour de longues années (and also race you on Sunday nights), et tu sais que "c'est pas faux!".

To Jackie, whose supervision, help, support and friendship through good and bad moments have been truly remarkable. Thank you for spending so much of your time correcting my English, it definitely feels like you're always putting everyone else first. Also, weirdly enough, thank you for being the least English, English person I know, by always expressing your opinion, even when we come to a disagreement! I wish our collaboration will be long and fruitful so that I can continue learning from you, but also start repaying you for all the efforts and advices you keep giving relentlessly (as for Yan I also wish to keep racing you on Sundays for a long time).

Then comes the rest of EViL:

Becky, the first of the "freed from desire crew", at first field assistant in Mexico, you grew, probably through coffee breaks in the lab, and despite your ~~Irish~~ Scottish accent, into a true friend. One of those you know distance will not change a thing and I cannot express enough gratitude for it!

Oliver, thank you so much for being a companion throughout my whole PhD. I think I can answer you here: I also wish we will never be stuck in a wet tent, at the top of a volcano ever again, but I truly wish we'll get to share tents or rooms again.

Jenny, the second of the "freed from desire crew", I don't even know how that happened. Thank you for those last few months, your arrival at the end of my PhD has brought much more than I would have expected.

Paul, thank you for beating me so often and easily at snooker, we should go again soon, right? I wish also to thank you for the long discussions we had and for your understanding of chemistry, you definitely helped a lot and I cannot wait to push our collaboration further.

To Felix, Guðjón, Adrian, Amy, and Josh, thank you for the discussions we had or continue having, I wish we'll continue doing great science together for a long time.

Just external to EViL, Fabian and Rick, thank you for your guidance and collaboration at various stages during my PhD.

My time in Liverpool could not have been as valuable as it has been without the presence of John, Joe G., Júlia, Pepe, Silvio, Nawal (aka. Provençal le Gaulois) ma compagne de taverne, Arthur (aka. coquine), Simon, Caroline, Stephan, Joe A., Mike, Gary, Dan, Ludo, Janine, James H., Delphine, Juliette, Samir, Jessie, Adrien, Noémie, Florianne, Hugo, Héloïse, Amélie, Anaëlle. Whether you welcomed me here, went for long nights out (or for a run for the healthier option), or for the discussions we had, I am grateful to all of you.

Ensuite, à ma famille: Maman, Cindy, Dylan, Tim, Jules et Damien. Je sais que mon choix de continuer en volcanologie a été difficile à comprendre et que le fait que je sois loin de vous a été difficile. Malgré tout, vous n'avez jamais cessé de me supporter dans mes choix, et il n'y a jamais eu un moment durant lequel je n'ai pas pensé à vous pendant mes jours loin de vous. Vous êtes ce que j'ai de mieux et je n'y serai jamais arrivé sans vous. Ensuite, Pépère, toi qui as toujours cru en moi, je ne peux que dédier l'aboutissement de toutes mes études à ta mémoire.

Viennent ensuite les personnes qui m'ont toujours soutenu ou apporté leur aide : Anna, les Bibiche(s) du M2, et spécialement Baptiste, Marco, Morgui, Poinpoin, Angèle et Dimitri (ainsi qu'Emmy et Basile), Rémy, Mickaël, merci de m'avoir supporté et encouragé tout au long de mon cursus universitaire.

Chapter 1:

Introduction

1.1. Motivation

Volcanic activity is a fearsome and mesmerising showcase of the dissipation of the Earth's internal heat that, over the centuries has inspired myths, legends, religions and art. Since as early as ancient Greece, volcanoes were revered and volcanic phenomena were explained by Hepheastus, the god of fire and volcanoes, hammering his anvil to forge weapons and armours for the gods in Olympus. Today, volcanoes continue to be revered and are, as such, undoubtedly important in the life of many ethnicities around the world. Volcanoes are also thought to have had a major impact on early life development (e.g. Martin et al., 2008), atmospheric evolution (e.g. Kasting, 1993) and contribute, to the sustainability of the 800 million people living within their vicinity (e.g. Brown et al., 2015) by providing rich and fertile soils (e.g.Sigurdsson et al., 2015). Furthermore, the flow of hot fluids (magmas, gases) provide unique environments for the formation of ore deposits and the exploitation of geothermal energy, from which society can benefit.

However, the unpredictability of volcanic eruptions also pose a threat on both a local scale and, as witnessed in 2010 with the Eyjafjallajökull eruption, on a regional to global scale. Despite the development of warning systems that couple geochemical analyses and geophysical monitoring (e.g. at Sakurajima volcano) our ability to predict volcanoes remains limited. This limitation is imparted to the fact that a knowledge of the magma's physico-chemical properties as well as an understanding of the state of stress within magmatic, volcanic and geothermal systems are pre-requisites better constrain models used to forecast eruptions. Both of which depend on many independent factors such as regional tectonic stresses (e.g. Gudmundsson, 2006) and structures (Gudmundsson and Loetveit, 2005), rock and magma strength and its evolution with changes in temperature, pore pressure and melt viscosity (e.g. Cas and Wright, 2012). Furthermore other variables, such as meteoric water infiltration can rapidly redistribute stress fields, modifying edifice stability (e.g. Day, 1996; López and Williams, 1993) and eruptive activity unpredictably (e.g. Elsworth et al., 2004).

Understanding how one or several of these parameters influence the stress distribution and evolution within the magmatic, volcanic and hydrothermal systems will help us better constrain the amplitude of volcanic events and subsequent hazards across different scales. Furthermore, in an evolving economic and political context, the desire for the use of fossil fuel energy is declining, while the drive and need for clean, renewable energy is growing increasingly stronger. One of the many alternatives resides in the exploitation of geothermal and hydrothermal fluids through the development of cheaper, more productive, geothermal energy (for instance, the creation of Enhanced Geothermal Systems (EGS)), to produce electricity. Improving our understanding of how these fluids are distributed and flow through the Earth's crust and within volcanic edifices, is key to maximise production rates at reduced drilling costs.

1.2. Heterogeneities in magmatic, volcanic and geothermal settings

1.2.1. Review of fluid flow in volcanic and geothermal environments

The Earth's crust, including volcanic edifices are extremely anisotropic environments, in which complex interplay between constantly evolving stresses and rocks with different mechanical properties and emplacement histories create heterogeneities (stratification, folding, faulting and fracturing, porosity) at all scales (Fig. 1-1). As such, and as many geological phenomena, fluid flow is scale invariant (e.g. Turcotte, 1997). For instance, at large scales, metamorphic reactions, can result in extensive heterogeneities that can alter both stress and fluid distribution in the crust (e.g. Amadei, 1996; Dragoni and Magnanensi, 1989; Wheeler, 2014). Similarly, tectonic faults and their damage halos (Fig. 1-1; Caine et al., 1996) create complex permeability structures (e.g. Faulkner, 2004; Sun et al., 2011) that can force stress fields to rotate (Faulkner et al., 2006) and localise fluid flow, be that magma forging its way through weakened pathways (e.g. Bonaccorso et al., 2013; Magee et al., 2013; Sigmundsson et al., 2015), or hydrothermal fluids exploiting permeable pathways (e.g. Curewitz and Karson, 1997; Rowland and Simmons, 2012).
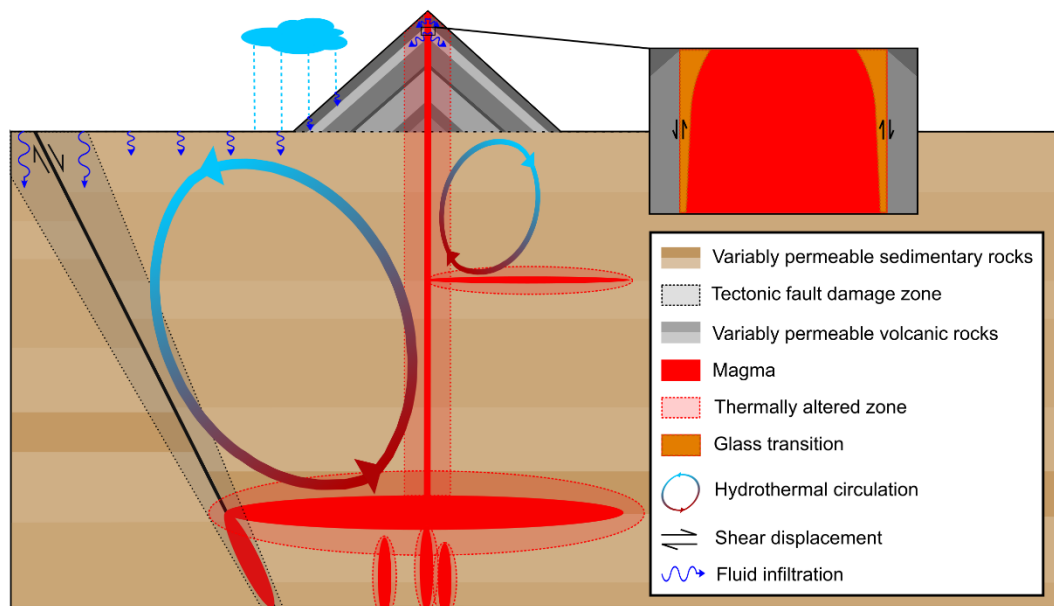
Figure 1-1. Possible geometric relationship between hydrothermal circulation, tectonic faults, magmatic plumbing systems and their associated damage zones.

While an extensive body of work exists on fluid flow around tectonic faults or in large sedimentary basins, similar concepts are yet poorly understood in smaller and highly dynamic magmatic, volcanic and geothermal systems.

For instance, while the successive emplacement of variably porous lavas flows and fragmented material layers creates an environment in which fluid flow would bare similar characteristics to that of fluid migration in large scale sedimentary basins (e.g. Bjørlykke, 1993), only few studies focussed their attention on pore pressure build up in volcanic edifices (e.g. Day, 1996; López and Williams, 1993). In these systems, each constituting unit has a characteristic strength and permeabilities that result from complex interplay between crystal growth, volatiles exsolution and viscosity changes during decompression and cooling of the magmatic melt (e.g. Blundy and Cashman, 2001; Cashman and Blundy, 2000; Costa, 2005; Hess and Dingwell, 1996; Mader et al., 2013; Melnik and Sparks, 1999). As such, highly porous/ permeable units allow fluids to flush through the system, while low porosity/ permeability units enhance the likelihood of fluid accumulation and pore pressure build-up (e.g. Farquharson et al., 2016). This results in lowering the effective stress (Reid, 2004) and, under the same shear stress conditions, in approaching the failure envelope of the material (Jaeger et al., 2009), increasing the possibility of fracture development (Fig. 1-2) that can lead to rupture (e.g. Day, 1996; Reid, 2004), thus forming smaller scales fault planes.
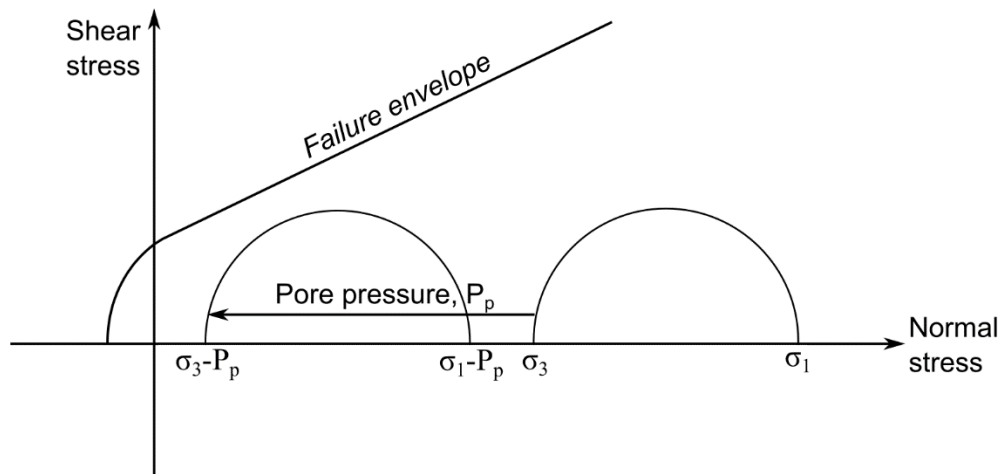
Figure 1-2. Mohr circles showing that increasing pore pressure reduces the effective stress, bringing the material closer to its failure envelope

Additionally, the migration of pockets of magma, or dykes, through the Earth's crust and the volcanic edifices (Lister and Kerr, 1991; Turcotte, 1982) can alter the stress field in their vicinity whether their propagation depends on the presence of pre-existing heterogeneities (faults, stratification) in the crust/ edifice or on the ability of the dyke to fracture the host rock itself. On one hand, dykes propagating through rocks with different fracture toughness can be deviated, accelerated, fully stopped (e.g. Gudmundsson and Loetveit, 2005; Maccaferri et al., 2011), or turn into sills (Fig. 1-1), promoting magmatic storage (e.g. Kavanagh et al., 2006; Kavanagh and Pavier, 2014). While on the other hand, dykes are also able to propagate and carry over-pressurised fluids by localising tensile stress at their tips and compressive stress along their walls (e.g. Wiederhorn et al., 2011), fracturing the host rock and causing in rapid stress changes in their vicinity (e.g. Gudmundsson and Loetveit, 2005). Furthermore, the quick thermal changes induced by the transport of hot melts in dykes can also alter the mechanical properties of the host rock (e.g. Brown et al., 2007) through the formation of macro-fractures (e.g. Browning et al., 2016) or high-temperature metamorphic reactions (e.g. Bakker et al., 2015; Dragoni and Magnanensi, 1989; Heap et al., 2013; Meredith and Atkinson, 1983; Mollo et al., 2012), thus affecting the permeability of the volcanic and geothermal systems.

Despite the knowledge that tensile (e.g. Gudmundsson and Brenner, 2009; Phillips et al., 2013) and shear fractures (e.g. Lavallée et al., 2012a; Neuberg et al., 2006; Tuffen and

Dingwell, 2005) are commonplace in volcanic and geothermal systems, the permeability of rocks remains commonly expressed as a function of connected porosity and described in relation to effective pressure (e.g. Blower, 2001; Bourbie and Zinszner, 1985; Farquharson et al., 2015; Klug and Cashman, 1996; Mueller et al., 2005). Previous studies have shown that the permeability of rocks increases non-linearly with porosity (Fig. 1-3; e.g. Ashwell et al., 2015; Benson et al., 2006b; Blower, 2001; Brace et al., 1968; Dasgupta et al., 2000; Eichelberger et al., 1986; Heap et al., 2015b; Klug and Cashman, 1996; Mueller et al., 2005; Saar and Manga, 1999; Sruoga et al., 2004) and decreases non-linearly with increasing effective pressure (e.g. Bernabé, 1986; Morrow et al., 1986). The results presented in these studies support the Kozeny-Carman relationship (Carman, 1937, 1956; Costa, 2006; Kozeny, 1927), suggesting that the permeability is controlled by micro-structures (micro-cracks and pore connectivity) and the tortuosity of the porous medium (e.g. Bernabé et al., 2010; Brace et al., 1968; Burdine, 1953; Hansen and Skjeltorp, 1988; Kushnir et al., 2016).
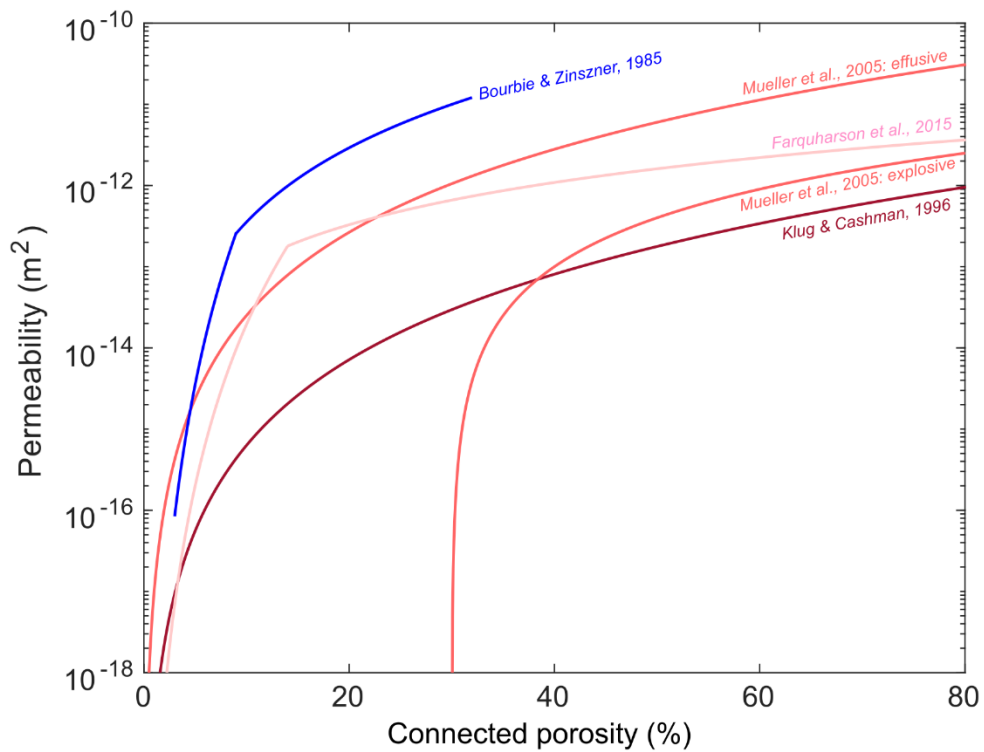
Figure 1-3. Empirical permeability-porosity relationships obtained for sandstone (blue: Bourbie and Zinszner, 1985) and volcanic rocks (dark red: Klug & Cashman,1996; red: Mueller et al., 2005; pink: Farquharson et al., 2015)

However, while in other lithologies, tensile fractures, or joints, have been shown to increase the permeability in the direction of the fracture plane (e.g. Aydin, 2000; Brown and Bruhn, 1998; Lucia, 1983; Matthäi and Belayneh, 2004; Walsh, 1981), only few studies have been quantitatively assessing the impact of such fractures on the localisation of fluid flow in volcanic rocks (Heap and Kennedy, 2016; Nara et al., 2011). Despite a growing knowledge on the development and longevity of fractures in volcanic and geothermal systems (see section 1.2.2), the current use of porosity as the main control on the fluid flow in this environments still hinders our ability to link the different signals associated to volcanic unrest, or geothermal exploitation.

1.2.2. *Development and longevity of fractures*

Any material, when subjected to sufficient stress and strain, is able to fracture (Anderson, 1905; Griffith, 1920). Ashby and Sammis (1990) described that, in heterogeneous materials, tensile micro-fractures nucleate around pores, crystals and pre-existing micro-cracks, forming "wings" that propagate away from the heterogeneities (the "wing-crack model"), parallel to the direction of the maximum stress (Fig. 1-4). Once tensile micro-cracks are formed, further deformation of the material can then lead to the development of macro-cracks (Bobet and Einstein, 1998; Shen et al., 1995; Tang and Kou, 1998). Healy et al. (2006) described in detail how the local stress field influences this progression, elaborating the description to polymodal fault patterns in triaxial settings. More recently, Lavallée et al. (2013) showed that a similar progression of tensile micro-fracturing, followed by coalescence and shear macro-fractures is plausible in deforming magmas (as the interstitial melt may be forced to respond elastically and rupture at high stress/strain rates).
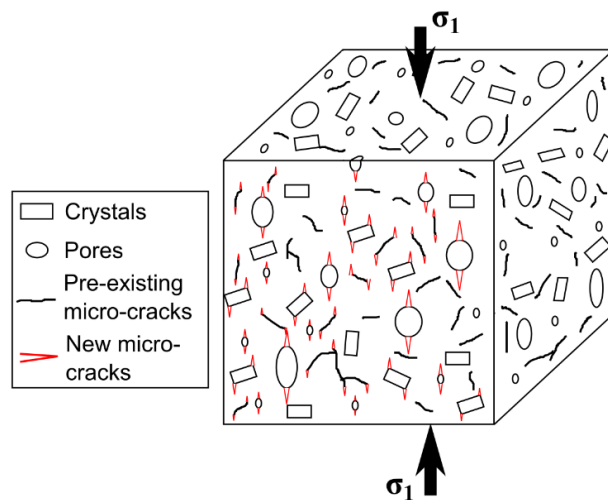
Figure 1-4. Wing-crack model (Ashby & Sammis, 1990) for the formation of tensile micro-cracks, in the direction of the maximum principal stress, around heterogeneities.

The deformation of a magmatic liquid (silicate melt) can lead to the crossing of the glass transition (Fig. 1-5; Dingwell, 1996). Silicate melts are visco-elastic bodies whose response (viscous and elastic) to an applied stress at a given temperature is strain rate dependent. At low rates, the Maxwell theory of viscoelasticity predicts a Newtonian response, where the material deforms to relax the stress after a characteristic, frequency-dependent, relaxation timescale, proportional to the viscosity of the melt, resulting in a viscous response of the liquid (Dingwell and Webb, 1989). At higher rates, non-Newtonian behaviour arises as the material cannot deform fast enough, forcing elastic response to relax the accumulating stress (Webb and Dingwell, 1990). Thus, the rate dependence of a magma to relax a stress plays an important role in understanding whether a magma is susceptible to fracture, or flow, and dictates whether a volcano may erupt explosively, or effusively, respectively.
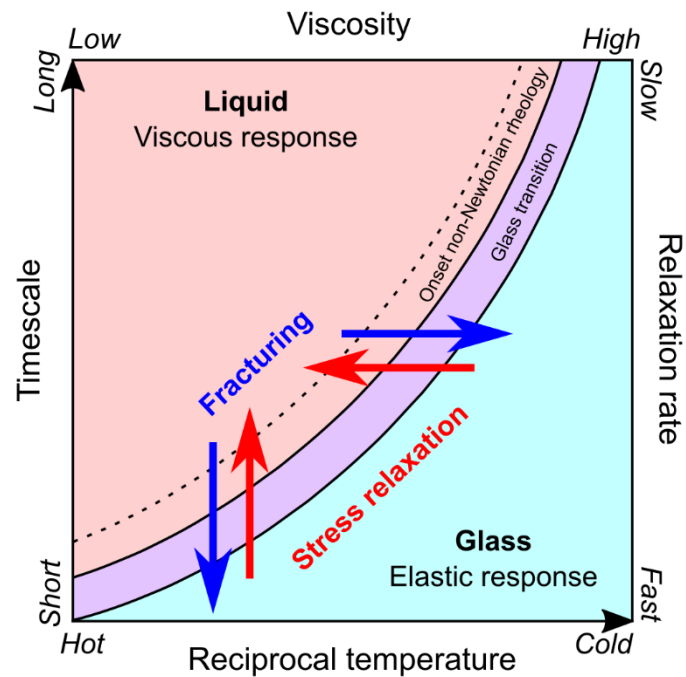
Figure 1-5. The glass transition expressed in a reciprocal temperature – timescale field (and conversely in a viscosity – relaxation rate field), where decreasing the temperature/ timescale over which the stress is applied may favour fracturing (blue arrows). Inversely, increasing the temperature/ timescale favours the relaxation of the applied stress by the melt (red arrows). Modified from Dingwell (1996).

Importantly, the presence of heterogeneities in magmas affect how the stress (and resulting strain) is distributed and fundamentally control the rheology (viscosity and strength) of the deforming material. In three-phase melts (crystals, pores, liquid), the presence of pores and crystals can concentrate stress, which produces locally high strain rates able to fracture the melt (Lavallée et al., 2008). For instance, both Bubeck et al. (2017) and Griffiths et al. (2017) have shown that pore geometry, direction with respect to the maximum stress and distance from one another directly control the strength of the rock. Additionally, crystals can accommodate deformation by deforming both elastically and plastically (e.g. Asaro, 1983; Deubelbeiss et al., 2011; Kendrick et al., 2017). Thus complicates fracture propagation and potentially hinders our ability to utilise geophysical signals (e.g. seismicity and deformation) to forecast rupture in magmatic, volcanic and geothermal settings (Vasseur et al., 2015).

The state of stress, and fracturing, in a rock not only depend on mechanically applied stresses but also on thermal stresses (e.g. Fortin et al., 2011; Menéndez et al., 1999). For example, upon heating or cooling, randomised, isotropic networks of micro-cracks have been shown to develop in basalts (e.g. Browning et al., 2016; Vinciguerra et al., 2005) and granites (Simmons

and Cooper, 1978). The formation of micro-fractures due to thermal stressing has been ascribed to a complex interplay between 1) differential thermal expansion of the heterogeneities (e.g. Meredith et al., 2001); 2) strain localisation along preferred crystallographic orientation in minerals (Meredith and Atkinson, 1983); 3) volumetric changes associated to a phase transition (e.g. α-β transition in quartz; Glover et al., 1995); 4) volumetric change of pore fluid upon temperature variations (Knapp and Knight, 1977). Moreover, given fast enough cooling rates, thermal cracking, can result in the formation of columnar joints in magmatic bodies (see Chapter 5). In such scenarios, locally high strain rates in a random network of micro-cracks may favour the growth and coalescence of the micro-cracks, forcing them to organise into polygonal sets of tensile macro-fractures. This mechanism has been proposed to occur, either by crossing of the glass transition of a crystallising melt (Lore et al., 2000a; Phillips et al., 2013; Ryan and Sammis, 1981a) or through the coalescence of micro-fractures in a fully crystalline material (Goehring and Morris, 2005).

Finally, Griffith (1920) also stated that the fracturing phenomenon is reversible, and as such fractures developed in both natural and synthetic melts and rocks have the ability to recover strength through healing (Jud et al., 1981; Tuffen et al., 2003) or sealing (Beeler and Hickman, 2004; Dobson et al., 2003a; Dobson et al., 2003b; Parry, 1998). Specifically, both fracture sealing and healing require high temperatures and diffusion of elements, and differ in the sense that sealing involves mineral precipitation in the fracture from a saturated melt (e.g. Fredrich and Evans, 1992; Olsen et al., 1998), whereas healing involves a first stage of viscous deformation during which the fracture walls wet one another and a second stage in which diffusive exchange across the fracture interface (Jud et al., 1981; Wool and O'Connor, 1981) is dominant. As a result, both processes are not instantaneous, and relics can often be seen in the rock record (Fig. 1-6).
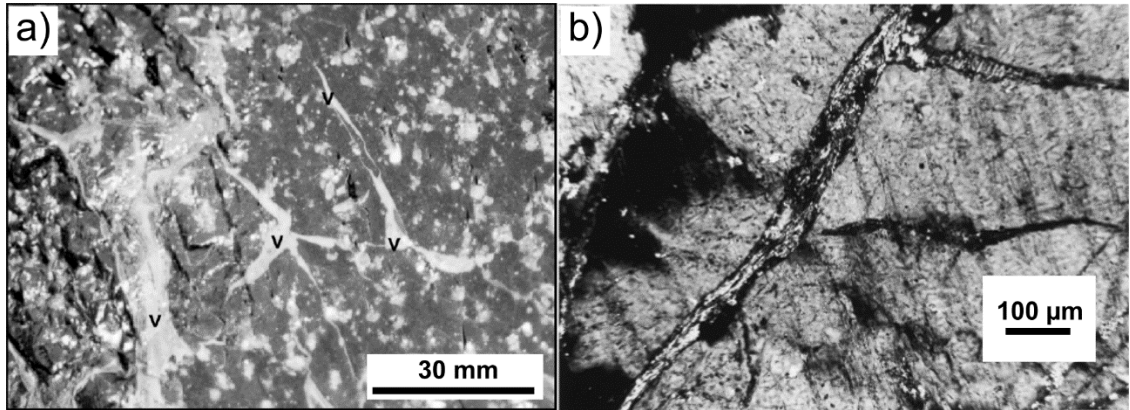
Figure 1-6. a) Healed fractures (v) in an obsidian, from Tuffen and Dingwell (2005); **b)** Fractures in feldspar crystals sealed by mineral precipitation (muscovite), from Parry et al. (1998).

Both fracture healing and sealing impose important controls on the evolution of stress and fluid flow in volcanic and geothermal systems as they have the ability to shut fractures and regain strength. For instance, Tuffen et al. (2003) suggested that repeated fracture and healing cycles could explain flow banding and cyclic seismicity observed at silicic volcanoes. They further proposed that the time required to complete a fracture-healing cycle equals the sum of the fracturing time, the relaxation time, and the time for viscous relaxation to occur. In geothermal systems, the precipitation of minerals from pressurised, saturated fluids force the permeable pathways to seal and fractures to become inactive to exploitation (Batzle and Simmons, 1977; Caulk et al., 2016). Consequently, understanding the development, longevity and impact of these fractures on the permeability of volcanic and geothermal systems is of prime importance to improve our models of volcanic activity and to help the exploitation of hydrothermal systems and the development of Enhanced Geothermal Systems (EGS).

1.3. Aims of the thesis

Here, by creating a set of uniquely designed experiments, I investigate the development, evolution and longevity of tensile fractures with temperature as well as characterising their impact on fluid flow in pressurised volcanic and geothermal systems.

Firstly, as the permeability-porosity-pressure relationships are relatively well described in the literature, I aim to broaden the understanding of the impact of fractures on the permeability of volcanic rocks with varying porosities at different effective pressures. By doing so, I discuss the consequences of permeability anisotropy and the creation of high pore pressure regions in volcanic edifices and geothermal systems (see Chapter 4)

While the formation of columnar joints in basaltic bodies results from the coalescence of micro-cracks into polygonal macro-fractures, when they form is still subject to debate. It is proposed that columnar joints formation occurs 1) In a crystallising magma where high strain rates may force the melt to cross its glass transition, nucleating fractures (Lore et al., 2000a; Phillips et al., 2013; Ryan and Sammis, 1981); or 2) In fully crystalline rock (Goehring and Morris, 2005). In this work, I aim to resolve the magnitude of cooling necessary for the build-up of tensile stress required to generate mode-I tensile cracks in basalt as well as to model the permeability evolution of a columnar jointing body as a function of temperature. As columnar joints can develop in lava flows and sills, I also discuss the implications for pore pressure distribution around columnar jointed reservoirs, both in the crust and the edifice (see Chapter 5).

Finally, the timescale for fracture healing in silicate melts remains relatively unconstrained. In this thesis, I refine the concept of Tuffen et al. (2003) using standard glasses at controlled conditions to determine the kinetics of the fracture healing process, including timescale and strength recovery, before discussing how it may contribute to repetitive cycles of eruptive and quiescent activity (see Chapter 6).

1.4. Structure of the thesis

This thesis explores the role of fractures in a range of volcanic materials, examines the development of cooling joints and describes the time-dependent healing of fractures in silicate melts. After this introductory chapter, Chapter 2, "Equipment", presents a detailed description of the two uniaxial presses and the hydrostatic ($\sigma_1 = \sigma_2 = \sigma_3$) core holder used for the data collection of this study, presented in Chapters 4 to 6.

This is followed by Chapter 3, "Methods and materials", which presents a brief description of the standard methods (Brazilian test, Young's modulus determination, porosity and steady-state permeability measurements) used in the study. Further details, particularly of the new methods developed herein, are presented in Chapters 5 and 6.

The key research concepts and findings of this study are then presented in Chapters 4 to 6. These chapters have all been written as stand-alone manuscripts for publication, therefore some repetition of material undoubtedly occurs as key concepts are re-introduced. For readability and conciseness, some modifications were made to the versions prepared for submission, in that the figures and subheadings were re-numbered for continuity within the thesis and all references have been compiled at the end of the thesis. Each of these chapters starts with the publication status of the manuscript and all contain their own abstract and conclusions. They are ordered so that the general concept of fluid flow in fractured environments is explained (Chapter 4) and then followed by two "case studies" in which fractures open (Chapter 5) and heal (Chapter 6). In detail, Chapter 4 introduces the results of permeability measurements of a wide range of volcanic rocks, both before and after fracturing, quantifying the impact of fractures on fluid flow in volcanic and geothermal settings. Chapter 5 then concentrates on the conditions for the development of fractures through columnar jointing (cooling fractures), in basaltic rocks. Finally Chapter 6 focuses on the mechanics and timescales of fracture healing in volcanic systems. Both Chapter 5 and 6 relate to Chapter 4 in that fluid flow is deeply influenced by the longevity of fractures in such extreme environments.

Chapter 7 synthesises the results presented in Chapters 4 to 6 and discusses possible implications and future directions for this work.

Finally, following the bibliography, a series of 4 appendices present, first, how the compliance of the loading column is taken into account during mechanical testing, followed by the supplementary material of the manuscripts presented in Chapters 4, 5 and 6, respectively. Again here, the numbering of figures and equations has been altered to match the format of the thesis.

Throughout this thesis, equations have been formatted so that **vector variables** are written in **bold**, while *scalar variables* and *constants* are written in *italics*.

Chapter 2:

Equipment

2.1. Uniaxial presses

The mechanical data presented in this work was collected using two different uniaxial presses capable of deforming material both at ambient (room) and high temperature. Each press is driven by a servo-controlled electric actuator and mounted with a load cell to control/ monitor the load rate and amplitude, a furnace to perform high temperature (up to 1200 °C) experiments and an axial Linear Variable Differential Transformer (LVDT) to control/ monitor the deformation rate and amplitude (the characteristics of each press are further described in sections 2.1.1 and 2.1.2). Finally, both presses run under the same operating system described in section 2.1.3.

2.1.1. Instron® 8800

This high temperature uniaxial press was built by Instron® in 1985 as a 1362 model, with a 100 kN Dynacell load cell. In 2013, it was retrofitted with an 8800 FastTrack tower to gain control and accuracy in strain measurements as well as to perform dynamic cyclic tests. The basic setup consists of a rigid frame to which the load cell and a fixed cylindrical piston are attached at the top, while the bottom part of the frame contains the motor and an electric actuator which drives the vertical motion of a piston to apply deformation to a specimen loaded between the compression platens. This press is set for compressive testing, and allows for a maximum axial sample deformation of 100 mm and accommodates maximum sample diameter of 75 mm in diameter. Additional support brackets hold a cylindrical, 3 zone split furnace for high temperature experiments (Fig. 2-1).
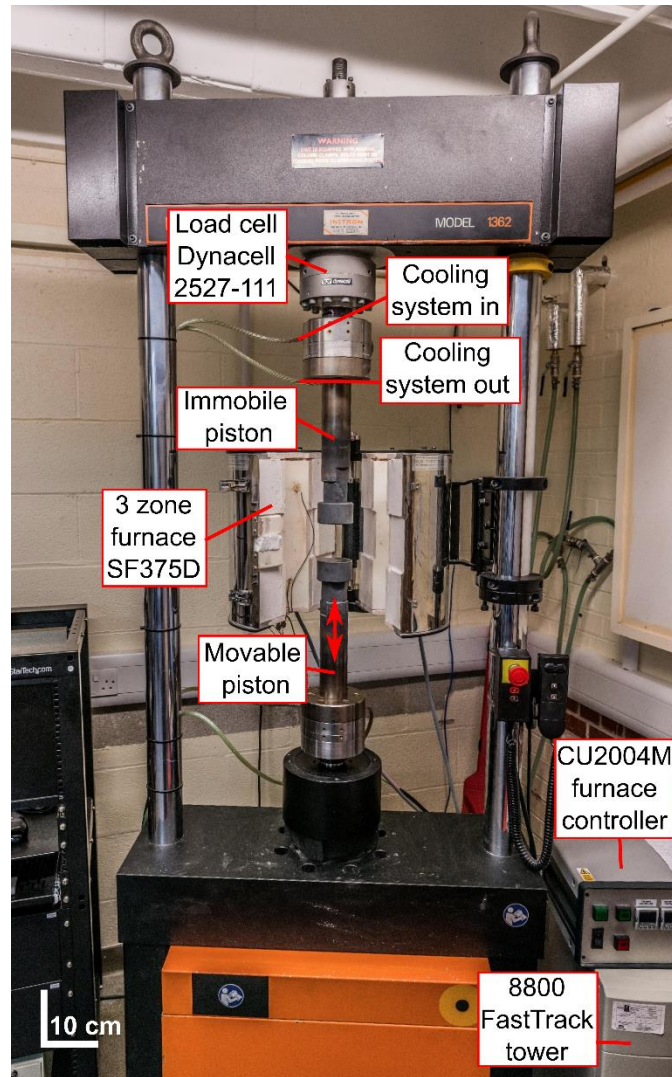
Figure 2-1. Labelled photograph of the Instron 8800 uniaxial press equipped with a SF375D split furnace.

The load cell mounted on this press is a Dynacell model 2527-111 with a 100 kN capacity. It comprises an auto-tuned accelerometer installed directly on the load axis, compensating for acceleration differences in the loading column and reducing both amplitude (static and fatigue tests) and phase shifts (dynamic tests) between the cell and the controller. As a result, this cell has a sensitivity of 1.6 to 2.4 mV/V, conferring both an accuracy of ±0.1% of the full load capacity. Importantly, the sensitivity of the cell is not affected by temperature changes (±0.002% per ºC) within the compensated temperature range of 0 to +50 ºC, removing the need for cell calibration to atmospheric conditions. During high temperature experiments, the cell is kept in the compensated temperature range by an external cooling system, ICS chiller, fitted in a hollow ring between the piston and the load cell and circulating chilled water to

keep the temperature of the load cell between 15-20ºC. This cell is automatically calibrated to meet the standard requirements of ISO 75001/1 Class 0.5, ASTM E4, EN10002 Part 2, JIS B7721, B7733 and ISO 10002 Part 2.

The press is controlled by a multi-axes 8800 FastTrack system, each axis being able to receive two channels. In this setup, the system is mounted with a single axis, where one channel is used to power a radial LVDT (Linear Variable Differential Transformer) and the other controls the axial deformation. To create a vertical motion in the loading column, the controller dispenses precise electrical input to a motor that generates a torque through a belt-pulley system. The torque is then amplified by an electric actuator, triggering the rotation of a vertical bolt that converts the rotation into linear motion, moving the bottom piston (Fig. 2-2). The setup allows accurate control of experimental conditions and control between loads of 100 N and 100 kN, at strain rates comprised between 10^{-6} and 10^{-1} s^{-1} and on samples <75 mm diameter.
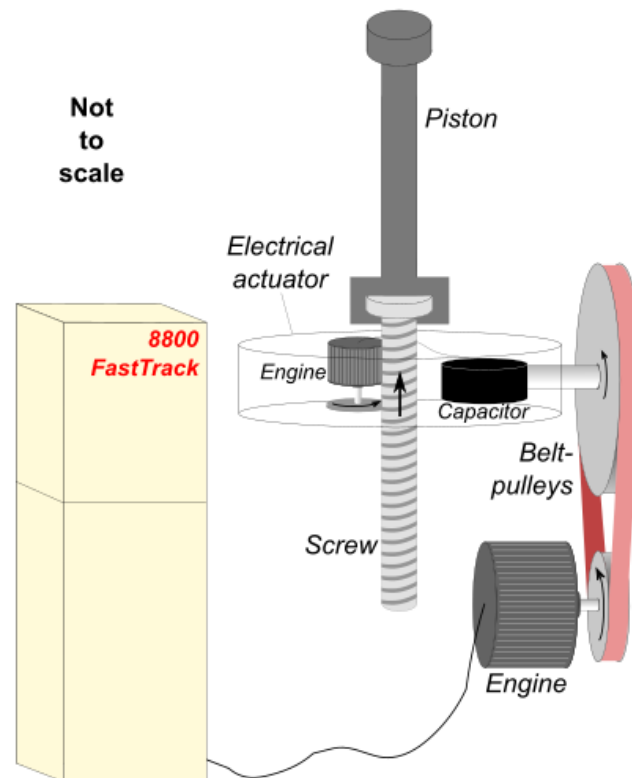
Figure 2-2. Diagram of the mechanisms driving the Instron 8800. The FastTrack tower supplies the electrical input required by the main engine that drives a belt-pulley system. This generates electricity in the capacitor of the electric actuator that is used to convert a horizontal torque to a vertical, linear motion of a screw, driving the piston up or down.

The 3 zone split furnace, model SF375D, was developed and recently refurbished by Severn Thermal Solutions Ltd. Each zone is independently monitored by a N-type thermocouple and controlled by a Eurotherm 3216 instrument, all mounted in a CU2004M controller. This system allows designable temperature profiles up to 1100 ℃ (maximum temperature of the heating elements), with four ramps (heating or cooling; heating rate 0.1 ℃/h to 20 ℃/min) and four dwell periods (up to 99 h each), on each zone independently, limiting heat loss around the sample by preventing strong thermal gradients between the internal zone and the exterior of the furnace. Overheating conditions (heating elements maximum temperature or required experimental conditions) are prevented by an additional Eurotherm 3216i which cuts the power supplied to the furnace if a user-defined maxima is exceeded. The maximum temperature of the elements coupled with the furnace insulation (reinforced oxide ceramic) allow a maximum sample temperature of 1000 ℃ (± 2 ℃).

2.1.2. *Instron*® *5969*

In this study, the benchtop press, model 5969, developed by Instron® has been used in true tension only, but the setup allows for quick changes from true tension to compression. The basic setup consists of two grips (or pistons in compression setup) installed in a vertical frame. The bottom grip is fixed to the base platen of the press, while the top grip is attached to a crosshead allowing a total vertical displacement of 1.2 m (without grips, 86 cm with grips). The grips can fit a range of jaw faces which can accommodate different sample geometries and width (10 – 16 mm diameter). Additional support brackets hold a single zone split furnace for high temperature experiments (Fig 2-3a).

The 5969 uniaxial press developed by Instron® is an all-integrated system which meets the standard requirements of ASTM E3, ISO 9513 and EN 10002-4. The press used in this study records data simultaneously on load, extension and strain channels at rates up to 1 kHz and is mounted with a 50 kN load cell, model 2580-203, that allows accurate load measurements over the whole load range. The load accuracy of this model, when used with this system, is ± 0.5% of the reading between 5 N and 50 kN. The position accuracy of the frame is ± 0.001 mm or ± 0.05 % of displacement, whichever is greater, allowing accurate strain measurements. The motion of the crosshead is driven by the same type of mechanism as the 8800 press in that the electrical input is converted to a mechanical output through a set of belt-pulley systems, motor and electric actuator that generate a torque. The difference resides in the fact

that for the benchtop press, the torque is transferred to a linear vertical motion in two vertical bolts located in the frame. This provides accurate experimental conditions between 5 N and 50 kN, at displacement rates of 0.001 to 600 mm.min^{-1} (equivalent strain rates of 10^{-6} and 10^{1} s^{-1}).
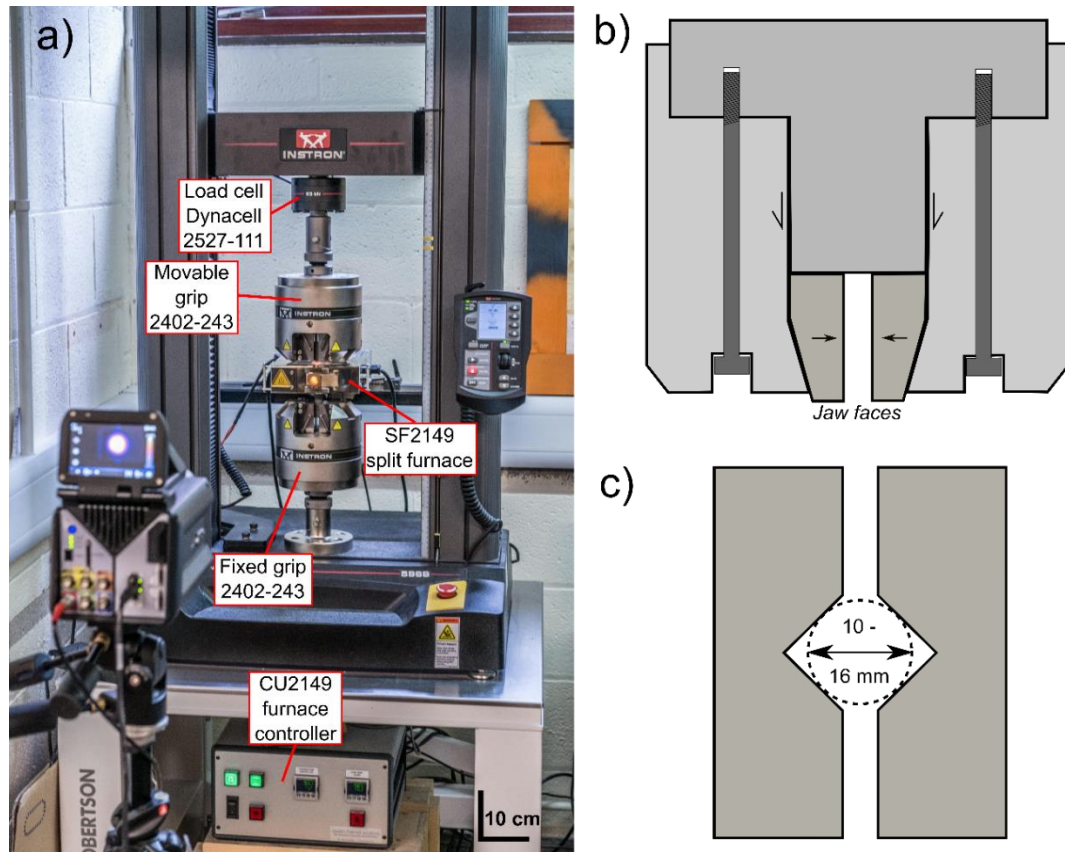
Figure 2-3. a) Labelled photograph of the Instron$^{®}$ 5969 benchtop press equipped with a SF2149 split furnace; **b)** Schematic representation of a 2402-243 mechanical tension grip; **c)** Top view diagram of the V-serrated jaw faces. The dashed circle shows the sample geometry in the jaw faces.

The grips (model 2402-243) in this setup are 170 mm high and 172 mm wide, with a total weight of 26 kg (each), acting as a heat sink, reducing the need of an external cooling system. They are equipped with V-serrated jaw faces (model 2703-546) that are forced down a V-shaped neck against the sample by a piston driven out of the grips (Fig. 2-3b). These jaw faces can accommodate samples between 10 and 16 mm in diameter (Fig. 2-3 c).

High temperature experiments are conducted with the help of a single zone split furnace, model SF2149, developed by Severn Thermal Solutions Ltd (Fig. 2-3a). It is mounted on fixed

slide support brackets that allow vertical positioning along the whole frame length. Temperature is controlled by an R-type thermocouple communicating to a Eurotherm 2216E controller, and monitored for overheating conditions (maximum heating elements temperature or set experimental conditions) by another R-type thermocouple communicating to a Eurotherm 2116i controller. Both controllers are installed in a CU2149 control unit, also developed by Severn Thermal Solutions Ltd. The setup allows designable temperature profiles up to 1400 ºC (maximum temperature of the heating elements) with four ramps (heating or cooling; heating rate 0.1 ºC/h to 20 ºC/min) and four dwell periods (up to 99h). Insulation, using refractory ceramic fibre, grants a maximum sample temperature of 1250 ºC ($\pm$ 2 ºC) over the 3 cm high homogeneously heated zone.

Table 2-1. Main characteristics of the different uniaxial presses used in this study

	Instron 8800	Instron 5969 (%)
Test type	Compressive	Compressive & True tension
Deformation range	100 mm	Up to 860 mm with tension grips
Sample diameter	Up to 75 mm	10 – 16 mm
Load capacity	100 kN	50 kN
Accuracy	$\pm$ 0.1% of full load capacity	$\pm$ 0.5% of the reading
Accurate load range	100 N – 100 kN	5N – 50 kN
Strain rates	$10^{-6} – 10^{-1}$ s-1	$10^{-6} – 10^{1}$ s-1
Sample temperature	Up to 930 ºC	Up to 1250 ºC
Used in chapters	4 & 5	5 & 6

2.1.3. Operating system

Both uniaxial presses described in sections 2.1.1 and 2.1.2 are operated through Bluehill® 3, a software designed by Instron®. It is directly compatible to the 5969 system used in this study. On the 8800 press, a virtual console is further present to increase the accuracy and control of the deformation and load. Bluehill® 3 provides a powerful monitoring and operating environment through a designable graphical user interface. A pre-defined methods library allows to set up and perform standard tests, such as compression or true tension experiments, at user-defined conditions. These tests can be performed at constant rate (loading/ deformation or strain rate, load/ position holds, etc.). More complex tests can also be designed using a test profiler and saved as a new method. A test profiler consists of a number of different steps with a set of constant conditions read by the controlling system (Fig. 2-4). Once the conditions for a step are fulfilled, the controller moves on to the next step. As a result, Bluehill® 3 offers a simple way to perform highly customisable, dynamic, deformation tests. Finally, it also includes a "Specimen Protect" feature that applies a definable constant load on the sample and that can be set both before the beginning and at the end of a test. This feature is used during sample loading to protect from accidental stressing and damage.
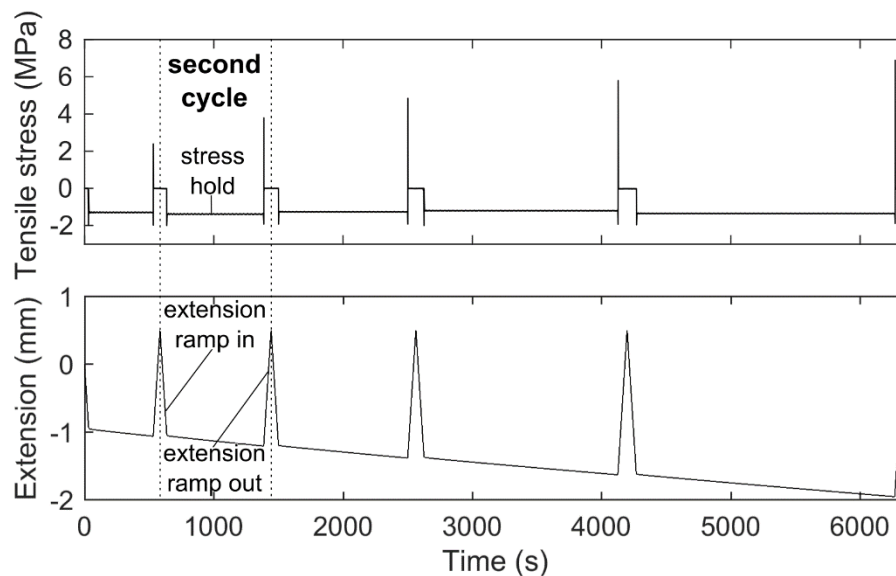
Figure 2-4. Cyclic test profiler during which cycles of extension control (ramp in, towards contact of the two samples; ramp out towards the load cell) and stress hold periods were repeated to replicate fracture and healing cycles.

2.2. Hydrostatic core holder

The pressure vessel used in this work was developed by Sanchez Technologies in 2014. The basic design consists of an open-ended, flat-bottomed, cylindrical cell, closed by a removable plug to which one piston is attached. The flat-bottomed side is pierced to let a second flared piston move on a horizontal axis within the cell. As a result, hydrostatic conditions ($\sigma_1 = \sigma_2 = \sigma_3$) are applied by injecting silicon oil inside the pressure vessel. Additionally, both pistons are pierced by a cylindrical hole along-axis and connected to external pumps in order to apply pore pressure (Fig. 2-5). This apparatus was used to measure permeability in Chapter 4 and 5.
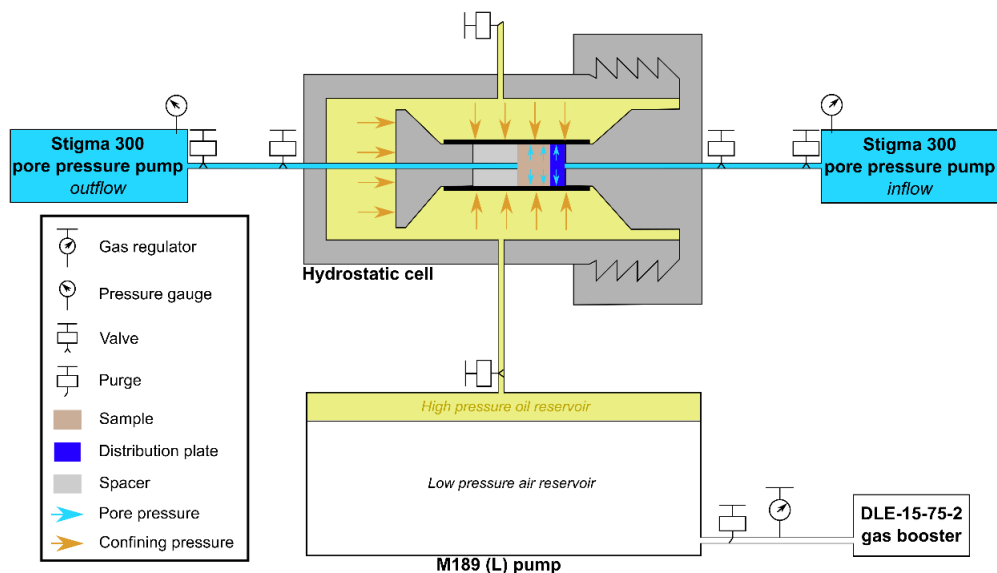
Figure 2-5. Hydrostatic core holder used in this study, in which two servo-controlled pumps can control either fluid flow or pressure differential to measure the permeability. The sample assembly consists of a pore distribution plate at the inflow side of the sample and a spacer to ensure hydrostatic conditions on the sample, at the outflow side.

All constituents of the pressure cell are made of laminated precipitation-hardening stainless steel. The cylindrical cell (diameter: 84.2 mm; length: 172.5 mm long; wall thickness: 39 mm) is closed by a 114 mm thick plug that connects via a saw-tooth-shaped thread. As a result, the pressure vessel is capable of sustaining a confining pressure of 200 MPa, but has been tested at a maximum allowable working pressure (MAWP) of 228.6 MPa in accordance with the High Pressure Safety Code (High Pressure Technology Association, 1975). The confining pressure is applied by injecting a low viscosity silicone oil (10 cSt; ~0.01 Pa.s), PMX-200 from Xiameter®, with a M189 (L) hydraulic unit from MAXIMATOR GmbH. This pump is

driven by a pneumatic system able to supply a maximum pressure of 23 MPa to the pressure vessel according to the pressure intensifier principle. In this setup, the hydraulic fluid (silicone oil) is contained in a small sliding reservoir connected to the pressure vessel. The oil reservoir is itself contained in a larger tank in which air at much lower pressure is injected (Fig. 2-6). The low pressure tank therefore forces the small sliding pressure tank outwards and the size ratio between the two reservoir results in forcing a small pressure over a smaller surface to concentrate the stress. In this setup, the pressure ratio is 1 : 660 (oil : air), the air supply being comprised between 0.1 MPa and 0.35 MPa, converts to oil pressures of 0.6 and 23 MPa.

In order to reach higher confining conditions, the air supply has been coupled to an air driven gas booster, model DLE 15-75-2, also developed by MAXIMATOR GmbH. This gas booster has a pressure ratio of 1 : 100, allowing a theoretical maximum air pressure of 35 MPa or a theoretical maximum oil pressure of 2300 MPa in the pressure cell.
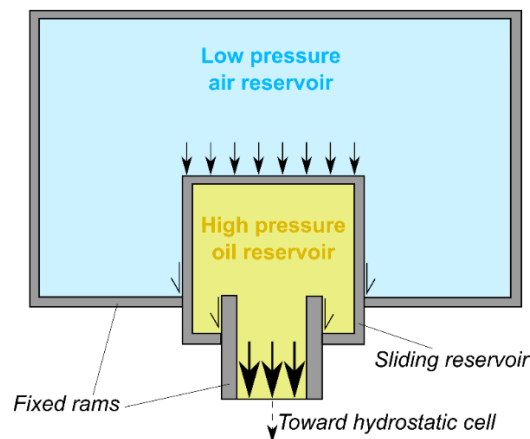
Figure 2-6. Pressure amplifier schematic view. A small sliding oil reservoir in a bigger, low pressure air reservoir is mounted between two fixed rams. The sliding motion and smaller volume compress the oil by concentrating the stress, resulting in the development of a high pressure oil reservoir.

The pore pressure system is driven by two pumps, model Stigma 300, developed by Sanchez Technologies. These pumps can hold up to 300 ml of pore fluid (distilled water in this study) and can operate at constant flow rates of 0.01 ml/min to 110 ml/min with an accuracy of ±0.1% of the set flow rate. They operate at an accuracy of 0.1% of the reading between pressures of 0.1 MPa and 100 MPa. The pumps are connected to the pressure vessel via high pressure hardened stainless steel pipes, able to sustain 200 MPa of pressure, that directly connect to both pistons (Fig. 2-5).

Chapter 3:

Methods and materials

This section presents the methods and materials (standard glasses) used throughout this thesis. It is worth noting that all compressive tests presented in this chapter (Brazilian tensile test, Young's modulus determination and parallel plate viscometry) have been corrected for deformation in the loading column. The so-called compliance method to account for loading column deformation is presented at the end of this thesis, in Appendix 1 (See Appendix. I).

3.1. Brazilian test

The Brazilian disc test is a widely used technique for determining indirect tensile strength of material due to the difficulty of performing true tension testing (Li and Wong, 2013). This standard method (ASTM, 2008) consists of diametrically deforming a disc in a uniaxial compressive setup (Fig. 3-1). The specimen should have a thickness-to-diameter ratio between 0.2 and 0.75 and a diameter which is at least 10 times larger than the biggest heterogeneity (pore or crystal). In all studies here, the materials are considered homogeneous until failure, in cases where an heterogeneity larger than a 10th of the diameter is found, mechanical results are discarded.
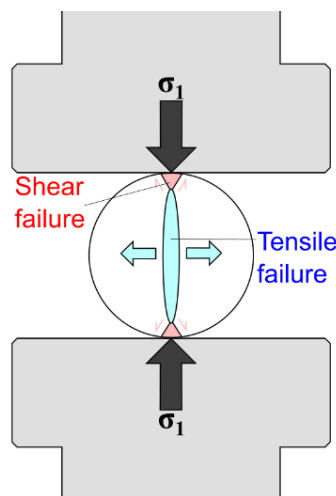
Figure 3-1. Tensile and shear stresses distribution in a Brazilian disc, modified from the version by Li and Wong, 2013.

Based on Griffith Fracture Criterion (Griffith, 1920), diametrically compressing a disc should induce tensile fracturing propagating from the centre towards the contact points with the loading pistons. Despite long debates on whether or not fracture initiation occurs at the centre or further away in the sample (see Li and Wong (2013) for a review), this method develops a single mode I tensile macro-fracture between the two loading pistons (Fig. 3-1). Occasionally a set of conjugated shear fractures can develop close to the loading points (Li and Wong, 2013).

The tensile strength of the rock, σ_T (Pa), can be calculated using (ASTM, 2008):

$$\sigma_T = \frac{2P}{\pi D t} \tag{3.1}$$

where P is the applied load (N), D and t are the sample's diameter and thickness (m), respectively.

In this study, this method was used in both Chapter 4 and 5. In Chapter 4, the tensile strength was not recorded as this technique was used solely to produce a clean tensile fracture through a set of 77 samples with porosities ranging from 1.2 to 41.7 %. The samples discussed in this manuscript were cored to a 26 mm diameter and cut to a thickness of 13 mm, giving an aspect ratio of 0.5 in agreement with the ASTM method. Samples were then axially and perpendicularly (with respect to the principal stress direction) wrapped in electrical tape before deformation, in the Instron® 5969 (presented in section 2.1.2), at a constant rate of 0.25 µm.s^{-1} (equivalent strain rate of 10^{-3} s^{-1}). The tape was used to prevent offset of the two halves and the development of shear fractures at the loading points.

In chapter 5, the tensile strength of a basalt at different temperatures is characterised using the Brazilian disc method in the Instron® 8800 press (presented in section 2.1.1). In this manuscript, samples were cored to 40 mm diameter and cut to 20 mm thickness, giving an aspect ratio of 0.5 in accordance with the ASTM method. All samples were deformed at a constant rate of 40 µm.s^{-1} (equivalent strain rate of 10^{-3} s^{-1}). Samples deformed at high temperature (820 - 900 ℃) were left to thermally equilibrate for an hour at the set temperature (to ensure that stress or strain localisation was not due to thermal gradient in the sample), before undergoing a similar strain to the room temperature samples.

3.2. Porosity determination

All porosity values in this study have been determined using an AccuPyc 1340 helium pycnometer developed by Micromeritics. This device measures the skeletal volume of a solid body and can be used to determine the solid density and connected porosity by injecting helium at a known pressure into a chamber with a known calibrated volume. The porosity results presented in Chapter 4 used a 35 cm^3 chamber (3.5×10^{-5} m^3).

To return the skeletal volume of a solid body, a helium pycnometer relies on Archimedes' principle. First, the volume of the empty chamber, V_{ch} (m^3), is calibrated using the ideal gas law:

$$V_{ch} = \frac{nRT}{P} \tag{3.2}$$

where n is the amount of helium (mol), R is the ideal gas constant (~ 8.31 J.mol^{-1}.K^{-1}) and T is the temperature of the gas (K). The pycnometer used in this study injects helium at a set pressure, P, of 21 psig, or $\sim 1.7 \times 10^5$ Pa.

Once the volume of helium in the chamber is calibrated, the chamber is emptied and a sample inserted. The same pressure of helium, 21 psig, is then injected into the chamber, resulting in a volume of helium being "displaced" by the equivalent skeletal volume of solid, V_{skl} (m^3), present in the cup. The ratio of skeletal volume to the volume of a sample equivalent perfect cylinder then returns the amount of voids opened to helium infiltration, or, more commonly, the connected porosity, Φ (%):

$$\Phi = 1 - \frac{V_{skl}}{\pi r^2 h} \tag{3.3}$$

where the volume of a perfect cylinder of radius r (m) and height h (m) is given in the denominator.

Finally, the density of the sample, ρ (kg.m^{-3}), of mass m (kg) is given by:

$$\rho = \frac{m}{V_{skl}} \tag{3.4}$$

This pycnometer returns V_{skl} with an accuracy of $\pm 0.1\%$.

Despite returning the connected porosity (helium being unable to reach the isolated pores), the use of this method remains relevant for this work as only the connected porosity contributes to the fluid flow (Colombier et al., 2017), and represents the vast majority (~95 %) of the porous structure (Mueller et al., 2008).

3.3. TinyPerm measurements

In this study, permeability measurements at ambient (atmospheric) conditions have been conducted using a TinyPerm II apparatus, developed by New England Research Inc. (NER). This handheld permeameter allows quick surface permeability assessment using the transient pulse decay method (Bourbie and Walls, 1982; Brace et al., 1968). A pressure pulse is created at the inflow side of the sample and the time required for pressure recovery (or pulse decay) is a function of permeability. Usually this method uses a positive pressure impulse (i.e. pressure increase at the inflow), however, the TinyPerm apparatus creates a vacuum at the sample surface (i.e. pressure drop at the inflow). This is achieved by pressing a deformable and impermeable rubber nozzle onto the rock surface and removing the air contained in the connected porosity into a syringe (Fig. 3-2). Hence, a good seal between the nozzle and the rock's surface is necessary to obtain an accurate permeability value.
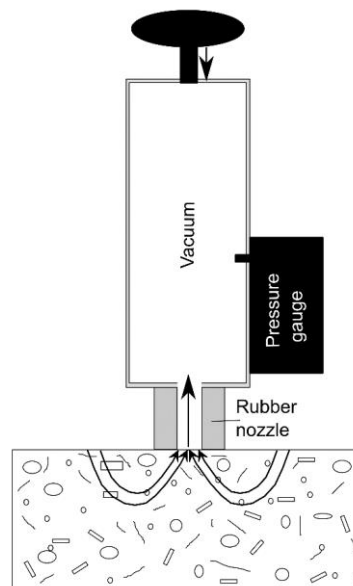
Figure 3-2. Schematic representation of the TinyPerm apparatus. A vacuum is created in the chamber by pressing the handle. The time required to recover the atmospheric pressure is a function of permeability.

The time for pressure recovery is permeability dependent and contrary to servo-controlled pumps where the amplitude of the pulse can be controlled, the amplitude of the vacuum created here is also permeability dependent. As a result, the time for one measurement varies from seconds, for highly permeable samples, to hours, for lower permeability samples (Fig. 3-3).
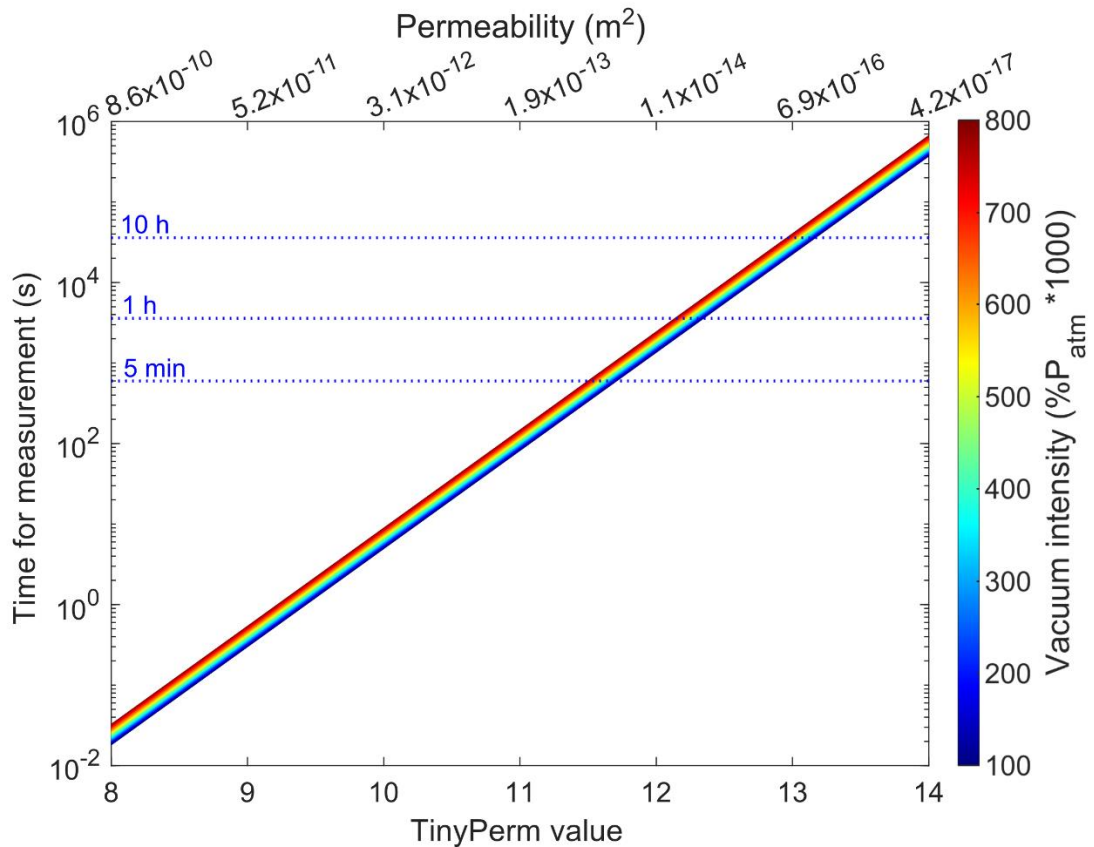
Figure 3-3. Calculated time for TinyPerm measurements of variably permeable samples as a function of vacuum intensity.

The suggested permeability measurement range of this apparatus is 0.01 to 10^4 mD (~10^{-16} to 10^{-10} m^2) according to NER, however, both Filomena et al. (2014) and Grover et al. (2016) have measured lower permeabilities in the lab, concluding that time for a measurement (>30 min) is the limiting factor. Importantly, these published studies, as well as data presented in the Appendix. II, show that this handheld permeameter produces highly repetitive permeability values that are comparable to those obtained on the same samples in laboratory permeameters.

3.4. Steady-state permeability measurements

All permeability measurements presented in Chapter 4 and 5 followed the steady-state flow method and use the calculation developed by Darcy (Darcy, 1856, 1857) that relates flow rate Q (m³.s⁻¹) and permeability k (m²):

$$k = \frac{Q\eta L}{A\Delta P} \tag{3.5}$$

where η is the viscosity of the permeating fluid (Pa.s), L (m) and A (m²) are the sample's length and cross-sectional area, respectively, and ΔP (Pa) is the differential pore pressure between the inflow and the outflow. This method can be applied under confining pressure (P_c) in pressure cells, such as the hydrostatic cell presented in section 2.2.

Steady-state permeability, or Darcian permeability, requires a constant and laminar flow across the sample (which may not always be applicable depending on the porous medium and/ or flow conditions, e.g. at high flow rates). To account for inertial effects, namely turbulence and fluid slippage along pore walls, two corrections can be applied or tested for.

The first correction applied, Forchheimer's correction (Whitaker, 1996), accounts for turbulent flow in the porous medium and generally applies to high Q regimes. This is corrected by looking at the linear relationship between the measured Darcian permeability, k, and Q:

$$\frac{1}{k} = \frac{1}{k_{forch}} + \xi Q \tag{3.6}$$

where k_{forch} is the permeability given by Forchheimer's correction, $\boldsymbol{\xi}$ is a constant defining all geometric and viscous parameters used in Darcy's calculation and is given by the slope of the linear relationship. When $\boldsymbol{\xi}$ is inferior or equal to 0, the flow is laminar and no correction is necessary. On the other hand, the inverse of the intercept of the line provides the correction to apply, k_{forch}.

The Klinkenberg correction (Klinkenberg, 1941) is the second correction applied as it uses the values obtained from Forchheimer's correction. It accounts for fluid slippage along pore walls and is determined by the intercept of the line defined by plotting k_{forch} against the inverse pore pressure, P_p.

Permeability measurements in both Chapter 4 and 5 were all performed by setting a constant ΔP across the samples and monitoring the resultant Q. The ΔP was carefully set to low values so that the flow remained laminar.

In Chapter 4, samples were fully saturated in water, before imposing an average P_p of 1.25 MPa at a set ΔP of 0.5 MPa, across the sample. This was achieved with an inflow pressure of 1.5 MPa and an outflow pressure of 1 MPa. These measurements were performed at a range of effective pressures (P_{eff}; $P_{eff} = P_c - P_p$) varying from 3.75 to 28.75 MPa, at 5 MPa increments. The sample assembly for these measurements consisted of a 26 mm diameter, 13 mm thick sample bound at the inflow by a porous distribution plate that forces homogeneous water distribution in the sample. On the outflow side, a cored stainless-steel spacer was inserted to enhance the contact between the mobile piston and the sample and ensure true hydrostatic conditions. A schematic representation of the sample assembly can be found in section 2.2 (Fig 2-5).

In Chapter 5, an average P_p of 1 MPa at a set ΔP of 2 MPa was induced across the sample after water saturation. This was achieved with an inflow pressure of 2.1 MPa and an outflow pressure of 0.1 MPa. Similar samples to those in Chapter 4 were prepared for this manuscript, only, to fasten water saturation and permeability measurements, the thickness was limited to 8 mm and permeability was measured only at 5 MPa confinement ($P_{eff} = 4$ MPa).

3.5. Young's modulus determination

The Young's modulus (E) of elastic materials can be determined both in tension and compression. This material property linearly relates applied stress (σ) to resultant strain (ε) and is expressed through Hooke's law:

$$\sigma = E\varepsilon \tag{3.7}$$

E can be determined by constraining the slope of the stress-strain curve for materials deforming purely elastically (i.e. within the linear portion of the mechanical data).

This method is used in Chapter 5 to determine the Young's modulus evolution with temperature of a basalt. For each sample, the slope was found for the linear portion of the curve, ignoring the first compactional phase (due to pores and micro-cracks closure) and the later strain hardening stage (where fractures open beyond the yield point).

3.6. Columnar joints experiments

Contrary to the methods presented above, this experimental setup has been specifically designed for the work presented in Chapter 5 and as a result has not been introduced elsewhere in the literature. The basic design of the columnar jointing experiments is that of a true tension test, in which a long rod, dog-boned in its centre to concentrate the stress (ISRM, 1978), is clamped into tension grips. The difference resides in the fact that, here, the tensile stress applied to the sample is not the result of a sample pull (grips moving away from one another) but is the result of thermal contraction in the dog-boned region of the sample, while the grips are locked in position (Fig 3-4; see also Appendix. III, Fig III-2). This setup was designed to re-create the nucleation and propagation of a fracture due to contraction upon cooling between two columns with "immobile" centres.
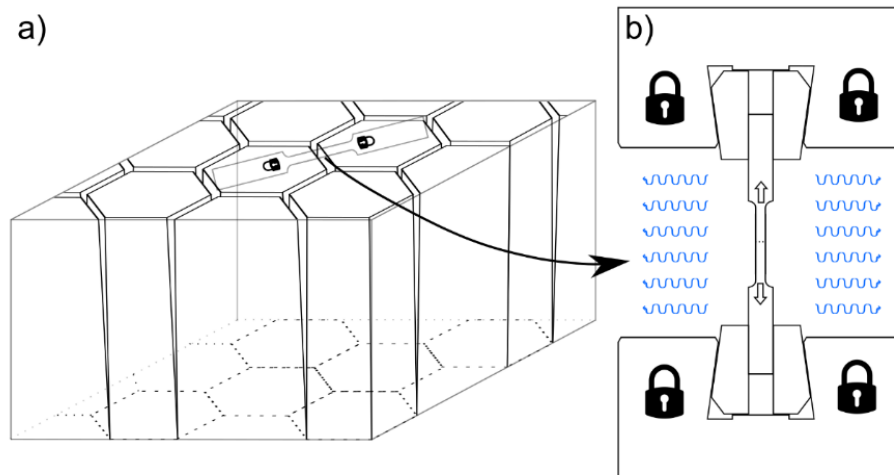
Figure 3-4. a) Experimental geometry in relationship with the formation of a fracture between two columns during columnar jointing. **b)** Experimental setup: the grips are locked in position, while cooling is induced at the centre of the sample (blue arrows), resulting in tensile stress build up (white arrows) and potential failure (dotted line) of the specimen.

More precisely, a columnar joint sample, is a 16 mm diameter, 180-200 mm long rod, dog-boned in the centre to 8 mm diameter and 35 mm long.

The sample was then placed in the Instron® 5969 (section 2.1.2), heated to ~ 980 °C, the solidus temperature of the basalt used in this study, and held at this temperature until thermal equilibration was reached. During the heating phase, the grips were free to move to account for thermal expansion of the sample and setup, without loading any substantial compressive stress. Once thermal equilibrium was reached, the grips were locked in position and the furnace was cooled at a set rate (between 0.05 and 10 °C/min). This cooling forced the dog-boned region to contract while the ends of the rods were kept at their original positions. This resulted in a tensile stress build-up in the dog-boned area that eventually overcome the tensile strength of the rock, resulting in the mechanical failure of the specimen.

3.7. Fracture healing experiments

The fracture healing experimental setup was designed for the work presented in this thesis and has not been introduced elsewhere. These experiments, involve a setup (Instron® 5969) to apply cycles of compression (also termed "contact" or "healing") and tension (or "fracturing"). The sample geometry is a modified version of dog-boned samples described in the previous section, in that the sample is cut at the bottom end of the dog-done. This results in a top, longer cylinder (16 mm diameter, 90-100 mm length) with a 30 m long dog-boned region (8 mm diameter) ground flat using a 30 µm diamond wheel; and a bottom, shorter cylinder (16 mm diameter, 50-60 mm length), ground flat at its top end (Fig. 3-5).
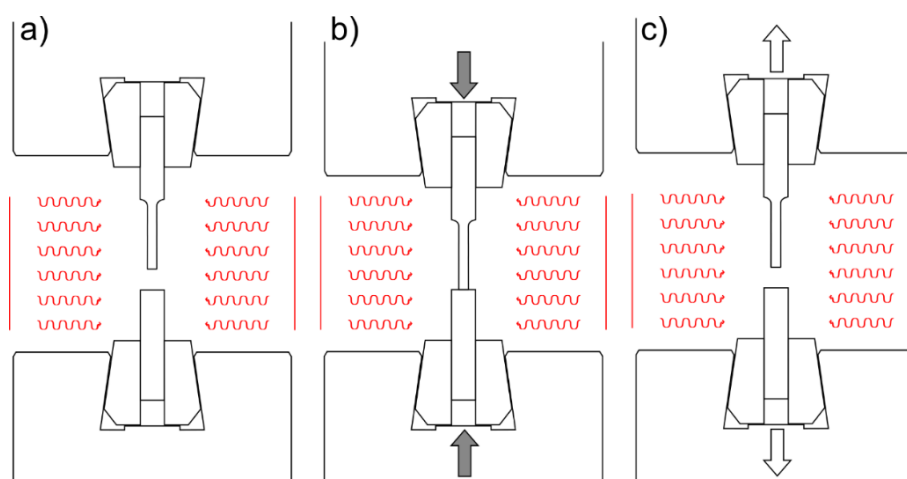
Figure 3-5. Fracture and healing experimental setup. **a)** Glass rods, not in contact, are heated up to the desired temperature (red arrows); **b)** Healing (grey arrows) is induced by forcing the glass rods in contact for a given amount of time; **c)** Fracture of the contact interface (white arrows) is induced by pulling the rods apart from one another.

The mechanics and kinetics of healing in silicate melts, presented in Chapter 6, are unravelled by cyclically compressing these two-part samples against one another at different temperatures (hence different melt viscosities) above their glass transition. The viscosity of the melt is determined using the parallel plate viscometry method (see section 3.8) and the healing/ contact times (compression periods) are set between 0.5 and 15000 s at an initial stress of 1 MPa. Consequently, the maximum contact time, at a given viscosity, is bound to an arbitrary maximum strain of 0.6, after which viscous deformation of the dog-bone is considered too intense for the experiment to continue. At the end of each healing period, the contact interface is fractured at an initial constant strain rate of 10^{-1} s^{-1} and the tensile stress required to fracture is monitored (Fig 3-6). This stress is corrected post-test for contact area change from the viscous bulging of the dog-bone using optical monitoring, and assuming isotropic deformation due to the use of standard glasses (see sub-sections 3.8.1 and 3.8.2 for a detailed description of the glass used).
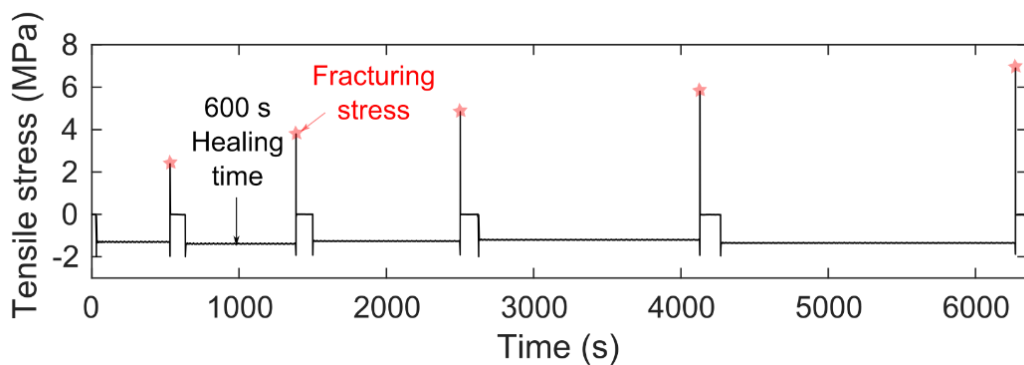
Figure 3-6. Tensile stress profile recorded during cyclic fracture and healing experiments.

3.8. Parallel plate viscometry

This method uses the theoretical work of Gent (1960), and consists of placing cylindrical samples (glass specimens with a 2 : 1 aspect ratio: 32 mm length : 16 mm diameter) between two parallel plates in the Instron® 8800. Here, standard glass samples were brought to high temperature in the three-zone furnace (section 2.1.1); the sample temperature was monitored throughout the test using a thermocouple. The samples were then deformed under three constant load (F) steps of 100, 500 and 1000 N for 1 to 10 minutes, depending on the viscosity of the glass. After the test, the strain rate, $\dot{\varepsilon}$, and sample height, h, evolutions were calculated

using the extension data monitored during the experiment, and viscosity, η, was then calculated using:

$$\eta = \frac{2Fh^4}{3\pi r^2 h_0 \dot{\varepsilon}(h_0 r^2 + 2h^3)}$$

(3.8)

where r and h_0 are the initial sample radius and height, respectively (Gent, 1960). Each test was performed to a maximum strain of 0.3, after which the sample shape was too altered (due to viscous flow (barrelling)) to perform accurate viscosity determination (Hess et al., 2008). The viscosity at a given sample temperature was determined by averaging the results of each constant load steps. This method has been used on the two standard glasses described in the next sub-sections and calibrated using the DURAN borosilicate glass 3.3 (further expressed as SDGS) by comparing the results obtained here to those provided by the company, Schott Duran®.

3.8.1. DURAN borosilicate glass 3.3

This borosilicate standard glass, developed by Schott Duran®, has been used for the majority of the healing experiments presented in Chapter 6 and, as discussed earlier, to assess the calibration of the data used to compute the viscosity using the parallel plate viscometry method (section 3.8). It was chosen for its affordability while at the same time meeting international standard requirements (ISO 3585, ASTM E438 Type I, class A). In addition, the glass was able to be sourced as 15 cm long, 16 mm diameter glass rods, which reduced sample preparation time.

This chemical composition of this glass, constrained by Schott Duran, is given in Table 3-1:

Table 3-1. Oxides content of the SDGS borosilicate glass, as communicated by the company, Schott Duran.

Oxide	Mass fraction (%)
SiO_2	81
B_2O_3	13
$Na_2O + K_2O$	4
Al_2O_3	2

The viscosity of this glass, η_{SDGS}, was measured here, using the parallel plate viscometry method, at 8.15×10^{11} Pa.s at 568 ºC, in good agreement with the viscosity of 10^{12} Pa.s at 560 ºC measured by the company. Further viscosity measurements were then performed to constrain the arrhenian dependence of viscosity of the glass within the temperature range of interest (Fig. 3-7), returning:

$$\eta_{SDGS} = a\mathrm{e}^{(b/T)} \tag{3.9}$$

where T is the temperature in ºC, $a = 3.073 \times 10^{-5}$ and $b = 21330$. This relationship was then used to determine the melt viscosity during healing experiments.
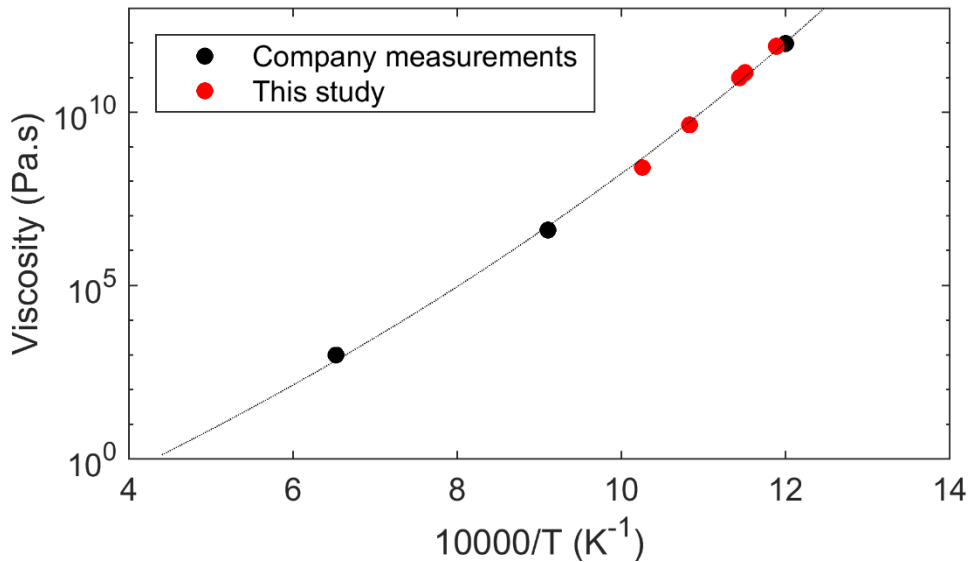
Figure 3-7. Arrhenius plot showing the temperature dependence of viscosity of the SDGS borosilicate glass. The black dots were given by the company (Schott Duran); the red dots were measured, in this study, using the parallel plate viscometry method.

3.8.2. NIST SRM-717a

This Standard Reference Material (SRM) 717a developed by the National Institute of Standards and Technology (NIST) is a borosilicate glass that was also used to perform healing experiments. The dependence of viscosity, η_{NIST}, with temperature, T, of this glass is certified by NIST to be:

$$\eta_{NIST} = 10^{-c + d/(T-e)} \tag{3.10}$$

where $c = 2.5602$, $d = 4852.2$ and $e = 192.462$. This non-arrhenian relationship was determined using the viscosity measurements of 7 collaborating laboratories (Fig. 3-8), and used in this study to determine the viscosity of the melt during healing experiments.
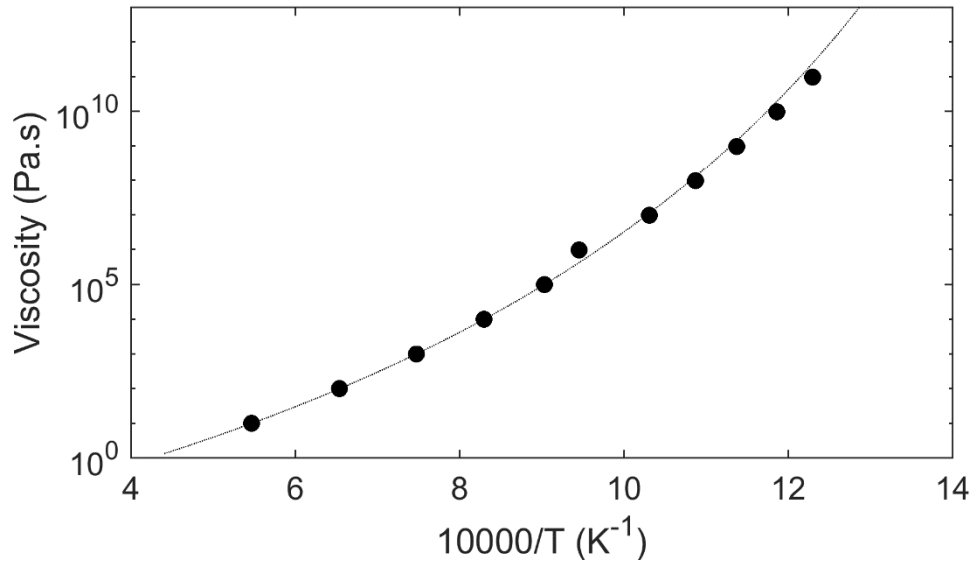
Figure 3-8. Arrhenius plot showing the temperature dependence of viscosity of the NIST borosilicate glass, as given by the company, NIST.

The chemical composition communicated by NIST is given in Table 3-2:

Table 3-2. Oxides content of the NIST borosilicate glass, as communicated by the company, NIST.

Oxide	Mass fraction (%)
SiO_2	68
B_2O_3	18.5
K_2O	8
Na_2O	1
Al_2O_3	3.5
Li_2O	1.0

"C'qui compte, c'est les valeurs!"

Perceval, *Kaamelot, Livre II*

Chapter 4:

The permeability of fractured rocks in pressurised volcanic and geothermal systems

In this Chapter, I characterise the impact of macro-fractures in variably porous volcanic rocks, at different confining conditions. This Chapter then forms the basis for the permeability calculations, and implications discussed in Chapters 5 and 6.

Publication status

Authorship: Anthony Lamur[1], Jackie E. Kendrick[1], Guðjón H. Eggertsson[1], Richard. J. Wall[1], James D. Ashworth[1], Yan Lavallée[1]

Affiliations:

[1] Experimental Volcanology Laboratory, Department of Earth, Ocean and Ecological Sciences, University of Liverpool, 4 Brownlow Street, L69 3GP, United Kingdom

Paper abstract

The connectivity of rocks' porous structure and the presence of fractures influence the transfer of fluids in the Earth's crust. Here, we employed laboratory experiments to measure the influence of macro-fractures and effective pressure on the permeability of volcanic rocks with a wide range of initial porosities (1-41 vol. %) comprised of both vesicles and micro-cracks. We used a hand-held permeameter and hydrostatic cell to measure the permeability of intact rock cores at effective pressures up to 30 MPa; we then induced a macro-fracture to each sample using Brazilian tensile tests and measured the permeability of these macro-fractured rocks again. We show that intact rock permeability increases non-linearly with increasing porosity and decreases with increasing effective pressure due to compactional closure of micro-fractures. Imparting a macro-fracture both increases the permeability of rocks and their sensitivity to effective pressure. The magnitude of permeability increase induced by the macro-fracture is more significant for dense rocks. We finally provide a general equation to estimate the permeability of intact and fractured rocks, forming a basis to constrain fluid flow in volcanic and geothermal systems.

4.1. Introduction

The storage and transport of fluids in the Earth's crust is of primary importance for our understanding of georesources and geohazards. In volcanic settings, fluids both circulate in hydrothermal reservoirs (Aydin, 2000) commonly exploited for geothermal energy, and drive magma ascent and volcanic eruptions (Collinson and Neuberg, 2012; Gonnermann and Manga, 2007; Kendrick et al., 2013). Better constraints of how fluids are transported in these systems will help define more accurate models, which in turn could lead to enhanced geothermal exploitation as well as improved prediction of volcanic eruptions.

All materials are inherently permeable, as permeability expresses either the diffusion speed at a molecular level or the capacity of a porous structure, at macroscopic level, to carry fluid flow. The permeability of rocks has been central to an extensive body of geoscientific studies since the early efforts of Darcy (Darcy, 1856, 1857) and is often described in terms of its relationship to porosity (Anovitz and Cole, 2015; Clavaud et al., 2008; Wright et al., 2009; Yokoyama and Takeuchi, 2009). In pursuit of a simple model constraining laminar flow in

conduits, the Kozeny-Carman (Carman, 1937, 1956; Gueguen and Dienes, 1989; Kozeny, 1927) relationship, or modifications therof, can commonly be employed to explain that permeability increases non-linearly as a function of porosity for a wide range of rocks (Costa, 2006; Dasgupta et al., 2000; Farquharson et al., 2015; Klug and Cashman, 1996; Mueller et al., 2005; Nakamura et al., 2008; Rabbani and Jamshidi, 2014; Saar and Manga, 1999). This equation describes the evolution of the permeability-porosity relationship by applying a coefficient dependent on the dominant conduit geometry controlling the fluid flow, namely tubular (connected pores) or planar (cracks) conduits (Bernabé et al., 2010; Kushnir et al., 2016). Previous experimental studies have invoked the existence of a percolation threshold for explosive volcanic products around 30% porosity (Blower, 2001; Klug and Cashman, 1996; Mueller et al., 2005), below which rocks are considered impervious to fluid flow, while the percolation threshold for porous media has been mathematically modelled to 59.27% in 2D (Sukop et al., 2002) and to 31.16% porosity in 3D (Stauffer and Aharony, 1994); with circular, and spherical pores, respectively). However, other efforts have demonstrated that fluid flow is promoted at lower porosities by fractures (Ashwell et al., 2015; Dobson et al., 2003a; Gaunt et al., 2014; Heap and Kennedy, 2016; Kendrick et al., 2016; Lavallée et al., 2013; Mueller et al., 2005), and hence it may not be appropriate to incorporate a percolation threshold when describing the relationship of porosity and permeability. Rather, it may be necessary to use several Kozeny coefficients (Costa, 2006) due to the presence of vesicles (bubbles) and fractures (Dasgupta et al., 2000; Klug and Cashman, 1996; Rust et al., 2004; Saar and Manga, 1999), and their evolution through multiple processes [including: vesiculation (Walsh and Saar, 2008), shearing (Ashwell et al., 2015; Okumura et al., 2010; Shields et al., 2014), fracturing (Kendrick et al., 2013; Laumonier et al., 2011; Lavallée et al., 2012a), cooling (Heap et al., 2014b)] that force pore coalescence. To describe this complexity Farquharson et al. (2015) proposed that the power law describing the permeability-porosity relationship can be decomposed into two regimes; a dense regime (<14 vol.% pores) for which the permeability is controlled by the connectivity of micro-fractures in the rock and a porous regime (>14 vol.% pores) for which vesicles control fluid flow. Such change points have been noted in other lithologies (Bourbie and Zinszner, 1985), and yet these relationships still fail to capture the fluid flow in natural volcanic environments (and associated hydrothermal/ geothermal systems), which is channelled through structurally complex pathways, containing highly variable, heterogeneous, and anisotropic porous networks, overprinted by complex fracture networks that enhance connectivity across all scales (Lee et al., 2001; Mourzenko et al., 2011; Sibson, 1994; Wannamaker, 2005). The effect of fractures on the overall permeability of a rock depends on the fracture's characteristics (Walsh, 1981); e.g., size,

roughness), the fracture system's geometry (Aydin, 2000; Chen et al., 1999) i.e., direction of the fault with respect to the fluid flow), whether the fracture system is dilatant versus compactional (Nguyen et al., 2014; Rutqvist, 2015; Zhang and Sanderson, 2002), and whether the fracture has in-filled fragmental material (Kendrick et al., 2016; Wadsworth et al., 2016; Wang et al., 2016). The presence of fractures can induce permeability anisotropy by opening localised pathways for fluid flow (Aydin, 2000; Chen et al., 1999; Farrell et al., 2014; Lavallée et al., 2013; Rutqvist, 2015; Walsh, 1981), for example, as observed along the shear margins of ascending magma (Gaunt et al., 2014). Even prior to macroscopic failure, the nucleation, propagation and coalescence of micro-fractures as material is loaded (and strained) increases the permeability, and permeability anisotropy of rocks (Loaiza et al., 2012; Simpson et al., 2001). The development of permeability anisotropy through damage accumulation (Benson et al., 2007; Nasseri et al., 2014; Schubnel and Gueguen, 2003) can alter intrinsic properties of geothermal, hydrothermal and magmatic reservoirs, including the mode of heat transfer/ fluid flow (Fairley, 2009). To understand the impact of macro-fractures, Lucia (1983), modelled the permeability of a system made of impermeable cubic samples separated by fractures with variable widths and determined that fracture spacing has a significant impact on the permeability of the system. In light of the importance of fractures on the development of permeable fluid flow, we hereby present the results of a series of experiments tackling the effect of fractures on permeability in rocks with variable initial porous structures (and starting permeabilities) and model the extensive dataset by adapting this cubic method (Lucia, 1983) to account for fluid flow through fractured rocks.

4.2. Material and methods

In order to assess the influence of fractures on permeability of rocks with a range of initial permeable porous networks (consisting of micro-fractures and vesicles), we selected a variety of extrusive volcanic rocks from six volcanoes (Ceboruco, Mexico; Volcán de Colima, Mexico; Krafla, Iceland; Mount St. Helens, USA; Pacaya, Guatemala; Santiaguito, Guatemala), and tested their permeability, both intact and fractured, as a function of effective pressure (calculated as the difference between the confining pressure and the average pore pressure).

70 cylindrical rock discs, 26 mm diameter and 13 mm thick were cored and prepared from the samples collected. The porosity of each disc was then calculated using quantification of the samples' volume (based on their dimensions) and determination of the samples skeletal volume using an AccuPyc 1340 helium pycnometer from Micromeritics with a 35 cm³ cell (providing sample volumes with an accuracy of ±0.1%). Permeability of the variously porous (1.2-41.7 vol. %) samples was then measured under ambient pressure, using a handheld TinyPerm II mini-permeameter (Filomena et al., 2014; Grover et al., 2016) from New England Research Inc., which utilises the pulse decay method by imposing air flow (746.13 ml) through an aperture of 8 mm (in contact with the sample). This method provides rock permeability determination with an accuracy >0.2 log units of permeability at low porosities, to 0.5-1 log units at higher porosities (verified by our dataset which includes 6-10 repeats of each measurement, see Appendix. II). Then, for a subset of 7 samples (with porosities spanning 1.2 to 30.0 vol. %), the permeability was measured as a function of confining pressure (5-30 MPa, at 5 MPa increments) using the steady-state flow method in a hydrostatic pressure cell developed by Sanchez Technologies. Here, confining pressure was applied by silicon oil, and water flow was induced by applying a pore pressure (ΔP) of 0.5 MPa (inflow of 1.5 MPa and an outflow of 1 MPa) across the sample (i.e., at an average pore pressure of 1.25 MPa), and the flow rate (Q) was measured and used to compute the permeability (k) using Darcy's law:

$$k = \frac{Q\mu L}{A \Delta P}$$

(4.1)

where μ is the water viscosity, L is the sample thickness and A is the sample cross-sectional area (Darcy, 1856, 1857). A further six unconfined measurements were made in the hydrostatic cell for direct comparison with the ambient pressure measurements of the TinyPerm (see Supplementary Fig. A. II-2). In these measurements, a ΔP of 0.015 MPa (inflow 0.17 MPa and outflow at atmospheric pressure of 0.155 MPa) was used, and the samples were double-jacketed to prevent fluid loss (as the inflow exceeded the confining pressure). All specimens (70 measured at ambient pressure and 7 measured under confined conditions) were then axially and perpendicularly wrapped in electrical tape before being fractured using the Brazilian tensile testing method (Nara et al., 2011) at a displacement rate of 0.25 µm.s⁻¹ (equivalent strain rate of 10⁻³ s⁻¹) in an Instron® 5969 uniaxial press. This technique generally induces one well-defined axial, tensile fracture through a diametrically-compressed cylinder (Yanagidani et al., 1978). [Note that the tape was used to prevent dislocation or shearing of the two main fragments generated by tensile testing and only samples with well-defined macro-fractures were employed in permeability analysis]. Following this, the permeability of all 70 fractured samples was measured with the TinyPerm

and for the aforementioned 7 samples (initially selected for permeability measurements in the hydrostatic cell) the permeability was again measured as a function of confining pressure in the hydrostatic cell.

The relative permeability change induced by the presence of a fracture was further modelled using the theoretical formulation developed for a fractured body by Lucia (1983) and modified herein for the effect of a variably permeable host material. Finally, thin sections of the rocks were prepared using a fluorescent dyed epoxy for microstructural analysis using a UV light source in reflected mode in a DM2500P Leica microscope.

4.3. Results

4.3.1. Permeability at ambient pressure

We observe that permeability varies as a function of porosity, increasing by approximately four orders of magnitude (at ambient pressure) for intact samples across the range of porosities tested (1.2-41.7 %; Fig. 4-1). This non-linear relationship between permeability (κ) and porosity (Φ), can be described by:

$$\kappa = 3 \times 10^{-17} \Phi^{3.11} \tag{4.2}$$

which constrains the dataset with a coefficient of determination (R^2) of 0.75. This relationship agrees well with that described in previous studies (Klug and Cashman, 1996; Mueller et al., 2005), and suggests that it is not necessary to fit this dataset with two regressions.

Using Brazilian tensile tests, we imparted a macro-fracture which resulted in a net increase in permeability for all porosities tested (Fig. 4-1). Across the range measured, the variability in permeability as a function of porosity (four orders of magnitude prior to fracturing) decreased to less than 2 after imparting a macro-fracture (Fig. 4-1). The permeability of the fracture-bearing rocks (κ_{fr}) is porosity independent and equals:

$$\kappa_{fr} = 6 \times 10^{-12} \pm 0.5 \log \text{unit} \tag{4.3}$$

Ultimately, the presence of a fracture modifies the relationship between permeability and porosity, with the permeability of fractured porous samples falling across a much narrower range than the permeability of the intact samples (i.e. much less sensitive to the initial rock

porosity; Fig. 4-1). In detail, we note a relative increase in permeability of up to four orders of magnitude by imparting a fracture, as noted in previous work (Heap and Kennedy, 2016; Nara et al., 2011). This increase is most pronounced for samples with low initial porosity (≤ 11 vol. %). Contrastingly, the permeability of the more porous rocks (≥ 18 vol. %) increases only slightly due to the presence of a macro-fracture, while intermediate porosity samples (11-18 %) show variable behaviour.
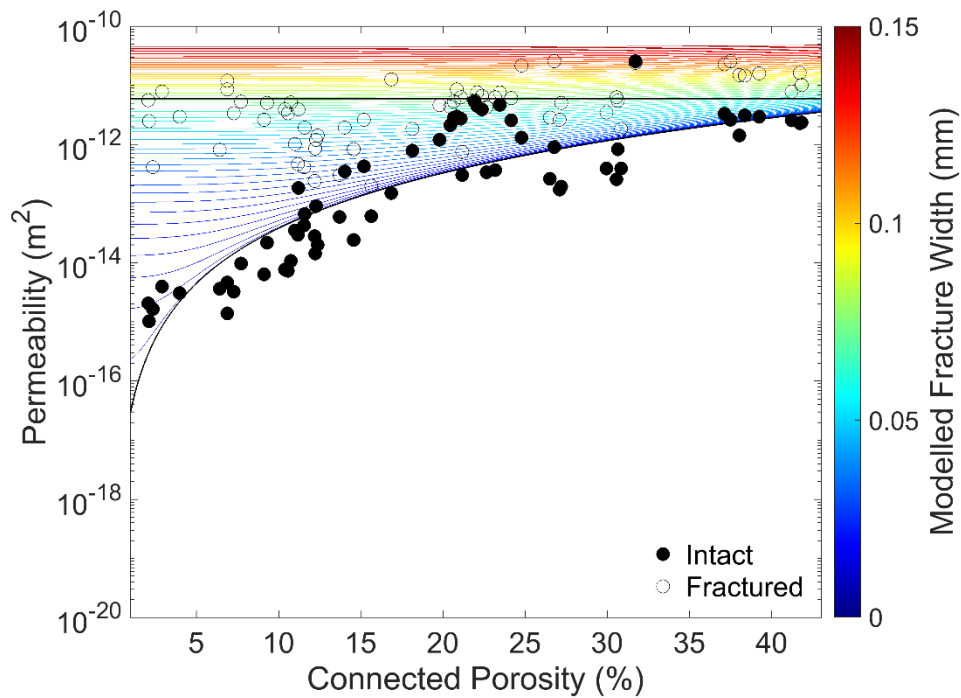
Figure 4-1. The permeability of intact and fractured rocks. Permeability-porosity relationships (black lines) for both intact (solid circles) and fractured (open circles) samples at ambient pressure. Coloured lines represent the modelled permeability of fractured rocks as a function of fracture width and rock porosity, derived from eq. 4.6 (See Fractured rock permeability analysis section). The convergence of the permeability values for intact and fractured samples at high porosities indicates that the effect of a fracture on permeability lessens with porosity increase, where the fluid flow is dominated by increasingly high pore interconnectivity. The data and model suggests that the fractures experimentally generated are ca. 0.06–0.07 mm wide.

4.3.2. Permeability at variable effective pressures

For the subset of samples measured in the hydrostatic cell, the permeability of intact and fractured rocks decreases non-linearly with increasing effective pressure (Fig. 4-2; see also Supplementary Fig. A. II-1). When plotting the data from the hydrostatic cell in porosity-permeability space, we observe similar trends to that measured at atmospheric pressure (Fig. 4-1; 4-3a; Supplementary Fig. A. II-3). We demonstrate a generally good agreement between

measurements made using the handheld TinyPerm device and the hydrostatic cell by conducting a targeted set of measurements at ambient pressure in the hydrostatic cell (see Supplementary Fig. A. II-2).
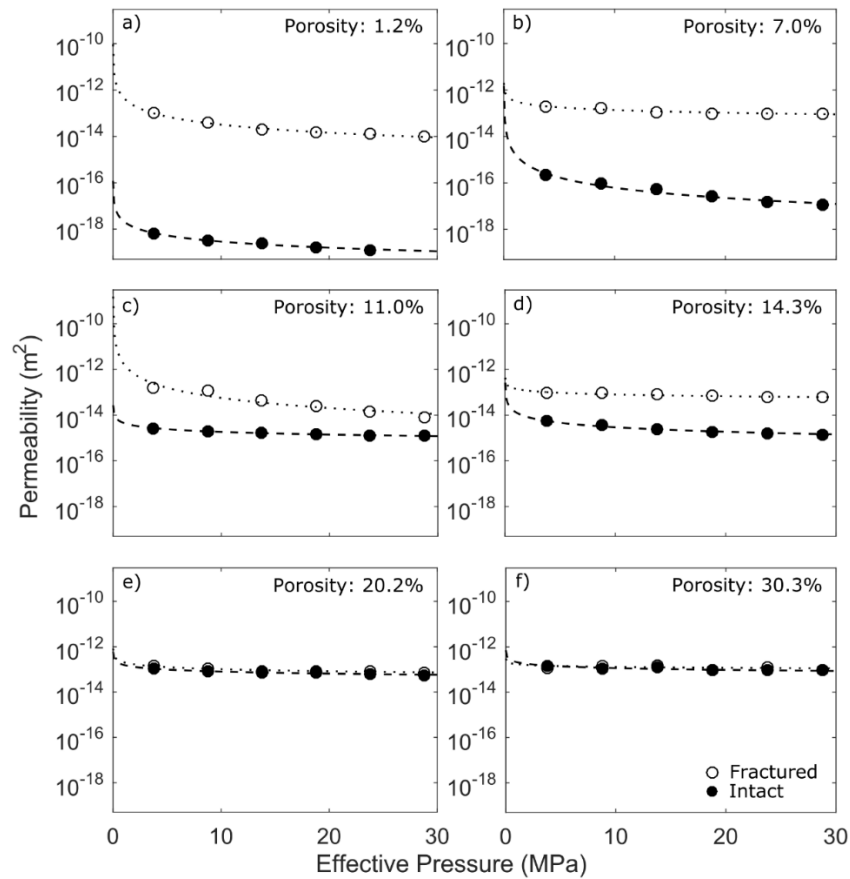
Figure 4-2. Rock permeability as a function of effective pressure. The data show the relationship between permeability and effective pressure for 6 of the 7 samples (intact and fractured) with (a) 1.2% porosity, (b) 7.0% porosity, (c) 11.0% porosity, (d) 14.3% porosity, (e) 20.2% porosity, and (f) 30.3% porosity. The impact of fracturing on a system's permeability is much more pronounced at lower porosities than at higher porosities. Results show that the effect of a fracture on permeability is dampened with an increase in effective pressure (beyond ca. 5–10 MPa), as shown by extrapolation of the best fit (dotted and dashed curves) of the permeability dataset conducted with the pressure vessel (circles). The last sample tested (porosity very close to the sample in (e)) is shown in Supplementary Figure A. II-1.

The influence of a macro-fracture on the permeability of the rocks tested here is similar at higher effective pressures as it is at atmospheric pressure, with the permeability increase that results from fracturing being more significant in the initially denser rocks (Fig. 4-3a). We further see that the influence of effective pressure on permeability is most pronounced in the densest rocks (≤ 11% porosity), while more porous rocks (≥ 18%) are less susceptible to

changes in pressure (Fig. 4-2, 4-3a); this supports previous studies, which examined the influence of pore closure under confining pressure on a range of rock types, suggesting the process is dominated by the closure of micro-fractures (Armitage et al., 2011; Benson et al., 2006a; Benson et al., 2005; Heap et al., 2015a; Kendrick et al., 2013; Wong, 1982; Zhu and Wong, 1997).
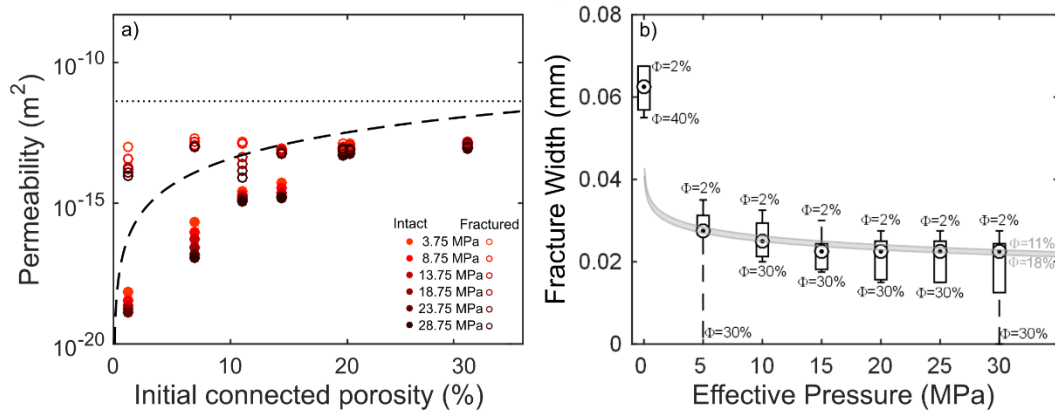
Figure 4-3. Permeability – porosity – effective pressure relationship for intact and fractured rocks. (a) Distribution of permeability and connected porosity data compiled as a function of effective pressure (darker colours represent higher pressures). The dashed and dotted curves display the best fits obtained for the intact and fractured samples, respectively, at ambient pressure (from Fig. 4-1). The measurements conducted at pressure trend towards those made at ambient pressures suggesting fracture closure even under modest confinement. (b) Boxplot showing the modelled fracture widths generated in samples with different porosities (Φ) and calculated evolution at different effective pressures. The grey zone displays the fracture width – effective pressure region for the porosity range 11–18 vol. %, using a least squares regression. The circles show the median of the fracture width distribution obtained by finding the closest value of the best fit, at each pressure step, to the calculated fracture width for our range of porosity.

4.3.3. Microstructures in intact samples

Microstructural analysis was conducted on thin sections impregnated with fluorescent green-dyed epoxy (highlighting the porous network of the rocks) to assess the reasons for the relative impact of a fracture on volcanic rocks at low and high porosities (Fig. 4-4). The rocks tested here were chosen for their chemical and mineralogical distinctions so as to widen the applicability of the findings of the influence of the porous network on permeability across a range of volcanic rocks and environments. The porous networks of the densest rocks (Fig. 4-4a, b) are dominated by an intricately connected network of micro-fractures, linking the vesicles present in the rock (Brace et al., 1968). Close examination of the photomicrographs show no overall preferential alignment (i.e., anisotropy) of the microfractures, but do highlight

preferred fracture developments along planes of weakness in phenocrysts. In contrast, the porous networks of the more porous rocks (Fig. 4-4c, d) appear dominated by the connectivity of vesicles of different sizes and shapes. These porous rocks exhibit few microfractures, and those which are present are primarily developed in phenocrysts (Fig. 4-4c, d). Such a contrasting architecture of the porous networks in dense and porous volcanic rocks has been observed in other studies (Heap and Kennedy, 2016; Heap et al., 2016; Kushnir et al., 2016) and may be at the origin of the non-linearity in permeability-porosity relationships discussed in previous studies (Farquharson et al., 2015; Heap et al., 2016; Kushnir et al., 2016) and in the relative effect of a fracture on the permeability of rocks as observed here. As such, we seek to test the applicability of fracture permeability modelling to describe the permeability relationships constrained in our experiments.
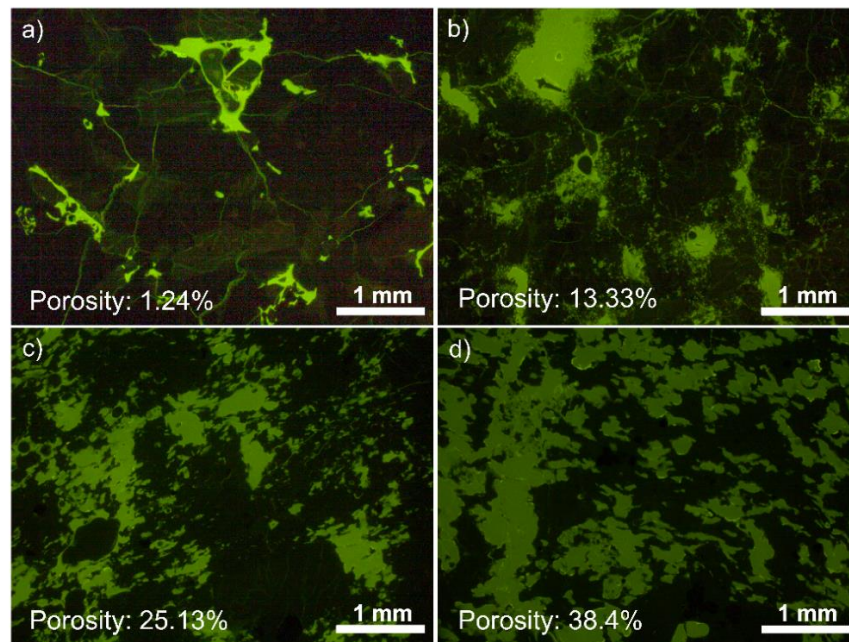
Figure 4-4. Microstructures of the permeable porous networks. Photomicrographs of 4 samples with varying connected porosities impregnated with green dyed, fluorescent epoxy, examined under UV light. (a) The connectivity of the densest rock, an andesite from Ceboruco (CBD_0; 1.2% porosity) is primarily controlled by micro-fractures; (b) The porous network of a Colima andesite with an intermediate porosity (COL_P2; 13.3%) showing a higher number of vesicles, connected to each other by micro-fractures; The connectivity of the more porous rocks from Ceboruco, (c) an andesite with 25.1% porosity (CBD_6); (d) an andesite with 38.4% porosity (CBD_10) is observed to be primarily controlled by vesicle coalescence.

4.3.4. Fractured rock permeability analysis

The permeability of fractures as a function of width can be modelled using the early work of Lucia (1983), in which the geometrical proportion of a fracture set arrangement is applied to a cubic body. The relationship is based on the principal of a pressure differential (ΔP) across a fracture with given length (L) and width (w), according to:

$$\Delta P = \frac{12\mu vL}{w^2} \tag{4.4}$$

where μ and v are the viscosity and velocity of the fluid flowing through the fracture, respectively. Lucia (1983) later modified the equation to obtain a system permeability (κ_s) formulation, which includes the area of the fracture as well as the surrounding rock:

$$\kappa_s = \frac{1}{12}\frac{A_f}{A_s}w^2 \tag{4.5}$$

where A_f and A_s are the cross sectional areas of the fracture and the sample, respectively. Considering the host rock permeability (κ_Φ), our cylindrical sample geometry and the near rectangular fracture geometry (produced in this study through Brazilian tests), Equation 4.5 can be further modified to:

$$\kappa_s = \kappa_\Phi + \frac{1}{6}\frac{w^3}{\pi r} \tag{4.6}$$

in which κ_Φ is the permeability of intact samples (each at a given porosity) and r is the aperture radius of the permeameter (i.e., 4 mm for the TinyPerm and 13 mm for the hydrostatic cell).

Using this relationship, we model the macro-fracture width (i.e., the coloured curves in Fig. 4-1) for rocks with different initial porosities and permeabilities. The permeability measurements on fractured samples coincide with the modelled permeability for rocks hosting a fracture of some 0.06-0.07 mm wide. We apply this analysis to the permeability obtained at each effective pressure (Fig. 4-3a, Supplementary Fig. A. II-3), to constrain the evolution of fracture width as a function of effective pressure. The boxplot (Fig. 4-3b) shows the modelled fracture widths for our range of porosities with increasing pressure. All boxes have been defined by finding the closest modelled fracture width to each permeability measurement at each effective pressure (see Fig. 4-1 and Supplementary Fig. A. II-3). The analysis suggests that the fracture closes non-linearly with effective pressure (Fortin et al., 2011), corresponding to the measured non-linear decrease in permeability, with most of the fracture closure

occurring within the first 5 MPa of confinement for all samples, irrespective of initial porosity (Fig. 4-3b).

In light of this constraint, and given the knowledge of the bulk fracture density (volume of macro-fracture/ volume of host rock), we rewrite the above permeability equations to provide a general formulation for the permeability of a fractured system (κ_s) as a function of the permeability of the intact system (κ_Φ), bulk fracture density (ρ_f), average fracture length ($\bar{l}$) and width ($\bar{w}$) over an area of interest (A_i):

$$\kappa_s = \kappa_\Phi + \frac{\rho_f \bar{l} \bar{w}^3}{A_i} \tag{4.7}$$

This formulation, expresses the permeability evolution of the intact system and constrains the impact of fractures on the overall permeability of the system. We can further expand this formulation to include the empirical description of the effect of effective pressure on the permeability of the intact rock (Eq 4.8) as well as on the fracture width (Eq 4.9.; see equations S2-7 in A. II.)

$$\kappa_\Phi = \left(2.93 \times 10^{-12} P_{eff}^{-1.07}\right) \Phi^{\left(1.64 P_{eff}^{0.06}\right)} \tag{4.8}$$

And

$$w = \left(2.33 \times 10^{-22} P_{eff}^2 - 2.67 \times 10^{15} P_{eff} + 3.39 \times 10^{-7}\right) \Phi^{\left(5 \times 10^{-4} P_{eff}^{-0.174}\right)} \tag{4.9}$$

where P_{eff} is the effective pressure in Pascals and each coefficient has different pressure dependent unit described in Supplementary Information (see A. II). Thus we can rewrite Equation 4.7 to:

$$\kappa_s = \left(2.93 \times 10^{-12} P_{eff}^{-1.07}\right) \Phi^{\left(1.64 P_{eff}^{0.06}\right)} +$$

$$\frac{\rho_f \bar{l} \left[\left(2.33 \times 10^{-22} P_{eff}^2 - 2.67 \times 10^{15} P_{eff} + 3.39 \times 10^{-7}\right) \Phi^{\left(5 \times 10^{-4} P_{eff}^{-0.174}\right)}\right]^3}{A_i} \tag{4.10}$$

providing us with an empirical description of rock permeability as a function of effective pressure, porosity, fracture density and geometry to be tested in various applications.

4.4. Discussion

Understanding the permeability of volcanic rocks, and especially fractured volcanic rocks, is crucial to our models of fluid flow in shallow volcanic and hydrothermal systems (Collinson and Neuberg, 2012; Edmonds et al., 2003). Here, a combination of extensive permeability testing and fluid flow modelling is used to demonstrate the ability to simulate the permeability of intact and fractured rocks and of fracture closure with confinement. In our fitting of the permeability-porosity relationship, we employed a single power law (as demonstrated by previous studies; (Dasgupta et al., 2000; Klug and Cashman, 1996; Mueller et al., 2005; Rust et al., 2004; Saar and Manga, 1999) as the regression is sufficient to fit the non-linear dataset accurately, without the need to invoke a change point. From microstructural examination (Fig. 4-4), we find that the connectivity of the porous network evolves due to the interplay of micro-cracks and few vesicles at low porosity, to enhanced pore interconnection at 11-18 % porosity (an observation which may share similarities with previously invoked change points; (Farquharson et al., 2015) and finally more complete coalescence at porosities ≥ 18 %. We emphasise that the porosity-permeability relationship of volcanic rocks results from a succession of processes undergone by the magma and the rock (i.e., vesiculation and pore collapse, fragmentation, sintering, shearing, cooling, contraction, etc) and as a result the porosity-permeability relationship does not describe a single generation mechanism, but rather reflects a combination of the above, which may have differing importance at different porosities. As permeability measurements accrue and widen the scatter at all porosities, evidence suggests that a simple power law, with acknowledgement of the scatter, remains an effective means to estimate the permeability of volcanic systems with wide ranging porous structures.

Across the range of porosities tested, the presence of a macro-fracture increases the permeability of volcanic rocks, although to different degrees, depending on the porosity of the rock. The impact of fractures on the resultant system permeability is greatest for low porosity rocks, where permeability can increase by up to four orders of magnitude (Fig. 4-1), which can be ascribed to a decrease in the tortuosity of the dominant fluid pathway by addition of a macro-fracture (Nara et al., 2011). This increase in permeability as a result of fracturing has previously been noted (Eggertsson et al., 2017; Heap and Kennedy, 2016; Wang et al., 2016). Here, we show that the initial porosity of the samples has little influence on the resultant

system permeability once a fracture is introduced. Matthäi and Belayneh (2004) classified the influence of a fracture on a rock permeability as either 1) fracture carries all the fluid flow; 2) fracture carries as much fluid flow as the host rock; or 3) fracture has a negligible impact on the permeability. Based on the findings presented here, we relate this classification to the relative magnitudes of permeability changes imparted by a fracture on rocks with different porosities: Regime 1 relates to dense rocks with ≤ 11% porosity; regime 2 to rocks with ~11-18 % pores and regime 3 to the most porous rocks (≥ 18 %), in which the presence of a macro-fracture imparts little change on the permeability of the system (Fig. 4-3). Interestingly, we find that the porosity thresholds for regime changes remain unaffected by changes in effective pressure, although the magnitude of permeability increase by inducing a fracture (i.e. the fracture width) is itself pressure dependent.

We provide an experimentally based, permeability model to describe the permeability of macro-fractured volcanic rocks with a range of existing permeable porous structures, which, using appropriate upscaling techniques (Farmer, 2002; Gavrilenko and Gueguen, 1998; Heap and Kennedy, 2016), may be adapted to a range of geological systems (Lucia, 1983). Utilisation of the simple formulation provided may help constrain or reassess a variety of processes for which an understanding of fluid flow pathways developed via multiple processes is crucial. For example, the percolation threshold of explosive volcanic products (Blower, 2001; Klug and Cashman, 1996; Mueller et al., 2005) may be modified significantly by fracturing. Previous works have demonstrated that outgassing in volcanic materials occurs through a network of fractures that localise and enhance fluid flow (Ashwell et al., 2015; Dobson et al., 2003a; Gaunt et al., 2014; Heap and Kennedy, 2016; Kendrick et al., 2016; Lavallée et al., 2013; Mueller et al., 2005), and gas monitoring at active volcanoes supports heterogeneous degassing models controlled by fractures in often low-permeability host rocks (Edmonds et al., 2003). Further, at the volcano-hydrothermal system of Soufrière Hills volcano (Montserrat), Edmonds et al. (2003) surmise that cyclicity/ fluctuations in gas emissions result from fractures undergoing episodic closure or sealing, leading to permeability changes in regions with high permeability anisotropy near conduit margins (Gaunt et al., 2014; Kendrick et al., 2014b; Lavallée et al., 2013). Our findings concur with these outgassing observations, as pore pressure (hence effective pressure) regulates the permeability of intact and fractured rocks. In this scenario, efficient outgassing may promote the lowering of pore pressure (i.e., effective pressure increase), fostering the ability for fractures to shut and subsequently heal (Tuffen et al., 2003). It must be noted that this sealing will be dependent

upon any fracture infill, which may either form a rigid network serving to maintain the permeable pathway, or may be subject to compaction or sintering, influencing the evolution of permeability (Kendrick et al., 2016; Wang et al., 2016). Sealing may inhibit further fluid flow and promote creation of momentarily impermeable, dense magma plugs (Ashwell et al., 2015; Edmonds et al., 2003; Lavallée et al., 2012b), which may then allow pore pressure build-up (i.e., effective pressure decrease), which if sufficient, may open (or reactivate) fractures or trigger fragmentation (Spieler et al., 2004). Thus, we advise testing of the formulation constrained here in anticipation that it may increase constraints on fluid migration and storage in volcanic, hydrothermal and geothermal systems.

4.5. Conclusions

We present a large permeability dataset, targeted to investigate the effects of porosity, fractures and effective pressure on the permeability of variably porous volcanic rocks. We observe non-linear relationships between porosity and permeability of both intact and fractured rocks as well as between the width of a fracture (and permeability of a fractured rock) and effective pressure. We propose a general formulation to constrain the permeability of intact and fractured rocks as a function of pressure, porosity and fracture density. This study aims to incorporate heterogeneities, such as fractures, in our modelling of the permeability evolution of dynamic and heterogeneous volcanic environments.

Chapter 5:

Disclosing the temperature of columnar jointing in lavas

In this Chapter, I investigate the conditions necessary to form columnar joints in cooling magmatic bodies. I further model the fracture width and permeability evolution using the analytical solution developed in Chapter 4 (Eq. 4.7).

Publication status

Authorship: Anthony Lamur[1], Yan Lavallée[1], Fiona E. Iddon[1,2], Adrian J. Hornby[1], Jackie E. Kendrick[1], Felix W. Von Aulock[1], Fabian B.Wadsworth[3]

Affiliations:

[1] Experimental Volcanology Laboratory, Department of Earth, Ocean and Ecological Sciences, University of Liverpool, 4 Brownlow Street, L69 3GP, United Kingdom

[2] Department of Earth Sciences, University of Cambridge, Downing Street, Cambridge, CB2 3EQ, United Kingdom

[3] Earth and Environmental Sciences, Ludwig Maximilian University – LMU-Munich, Theresienstrasse 41/III, 80333 Munich, Germany

Contributions: All authors contributed to and revised the manuscript for first submission.

- Anthony Lamur: Primary investigator; carried Young's modulus measurements, Brazil tests and columnar jointing experiments; drafted the manuscript and figures.
- Yan Lavallée: Conceptualised the original idea and the experimental setup; helped performing columnar jointing experiments; sampled the columnar joints exposure; Drafted figure 1.
- Fiona E. Iddon: Helped performing dilatometric measurements, some Brazil tests and columnar jointing experiments; surveyed the columnar joint exposure in Iceland.
- Adrian J. Hornby: Performed most Brazil tests.
- Jackie E. Kendrick: Helped performing columnar jointing experiments; surveyed the columnar joints exposure.
- Felix W. Von Aulock: Performed dilatometric measurements.
- Fabian B. Wadsworth: Helped performing some columnar joints experiments.

Paper abstract

Columnar joints are a spectacular feature of volcanic rock, which form by cracking during cooling-induced contraction of lava. Their formation incises permeable pathways allowing efficient hydrothermal fluid circulation. This process, and the resultant geometry, arises from a complex interplay between heat dissipation, contraction and tensile strength of the lava, yet the lack of direct measurements of the formation temperature of such joints has led to ambiguity about the temperature window of jointing, and its impact on fluid flow. Here we develop a novel thermo-mechanical experiment to disclose the temperature of columnar jointing in lavas for the first time. Using basaltic rocks from a lava flow at the base of Eyjafjallajökull volcano (Iceland) we show that contraction during cooling induces stress build up below the solidus temperature (980 °C), resulting in localised macroscopic failure between 890 and 840 °C; that is, 90 to 140 °C below the solidus. This window of undercooling for incipient columnar joint formation is supported by modelling informed by mechanical testing and dilatometric analysis of the expansion coefficient. We demonstrate that columnar jointing takes place well within the solid state of volcanic rocks. By computing the permeability evolution of columnar jointing bodies we find important implications for the construction of permeable networks for fluid flow in volcanic, geothermal and hydrothermal environments.

5.1. Introduction

Columnar joints form by cracking due to cooling-driven contraction of igneous rocks (Kantha, 1981), which result in tensile failure (Degraff and Aydin, 1993). Their presence in the rock record has long represented one of the most awe-inspiring geological features (Laboulais-Lesage, 2004) and their regular geometry has challenged our understanding of pattern ordering during thermal contraction (Goehring and Morris, 2005). To date, the temperature of their formation has remained unconstrained, although it holds thermo-mechanical information key to resolving the cooling history of volcanic rocks (Mattsson et al., 2011; Phillips et al., 2013) and intrusive magma bodies (Carrigan, 1986). Columnar joints are permeable structures that play an important role in fluid circulation in the crust, exerting controls on heat transfer

(Carrigan, 1986; Lister, 1977), resource transport and ore deposition (King et al., 2014), geothermal and hydrothermal reservoirs (Xu et al., 2006) as well as rock alteration, and degradation of rock mechanical properties (Barton et al., 1985).

Columnar joints develop in cooling intrusive and extrusive volcanic rocks, irrespective of their chemical composition or emplacement environments, and have recently been discovered on Mars (Milazzo et al., 2009). Structurally, columnar-jointed rocks classically exhibit two jointing facies: in an idealized system, a cooling unit is characterised by a lower colonnade with linear and parallel columns, and an overlying entablature with curved and irregular columns, which may be superimposed by an upper colonnade (Spry, 1962; Tomkeieff, 1940). In complex bodies stress distribution can disorder column formation (Phillips et al., 2013; Spry, 1962) and occasional absence of the upper colonnade has been attributed to erosion or intense cooling regimes accentuated by abundant water incursion in a flow's interior (Saemundsson, 1970). Colonnades exhibit quasi-hexagonal fracture patterns, bounded by striae (Figure 1), the spacing of which has been shown to scale with column width, likely reflecting the cooling history of the flow (Goehring and Morris, 2008; Grossenbacher and McDuffie, 1995). The quasi-hexagonal fracture geometry has been ascribed to thermal contraction induced by conductive cooling, occasionally enhanced by water infiltration of the fracture network (Budkewitsch and Robin, 1994; Degraff and Aydin, 1993; Goehring and Morris, 2008; Grossenbacher and McDuffie, 1995; Rieter et al., 1987). The hypothesis remains that upon cooling, tensile stress accumulates elastically (Browning et al., 2016), generating a random network of micro-fractures, that slowly develops into a more ordered polygonal set of mode-I tensile macro-fractures (Goehring and Morris, 2005) (Figure 1). The formation of a permeable fracture network then increases the infiltration and transport potential of fluids in the cooling body, contributing to the development of entablature (Forbes et al., 2014). It has previously been proposed that stress build-up and fracturing takes place during rapid cooling beyond the glass transition of the melt inside crystallising lavas (that is, at super-solidus temperatures where lava is still partially molten; Forbes et al., 2014; Lore et al., 2000b; Phillips et al., 2013; Ryan and Sammis, 1981a). Semi-circular petrographic structures, present in some columnar joints, are interpreted to result from melt segregation driven by contraction and fracturing triggered during crystallisation (Kantha, 1981; Symons, 1967). Cross cutting of the semi-circular structure by the fracture has been used to contest fracturing of melt (undergoing the glass transition); instead melt segregation has been

demonstrated to result from changes in the physical and rheological properties of melts during crystallisation (Mattsson et al., 2011). The quenching of melt to glass relies on a relatively rapid cooling rate and predominantly high viscosities which prevent complete crystallisation (Dingwell, 2006); thus the glass transition is more likely to be met in silicic lavas than in mafic lavas. In basaltic lava flows, vitrification is restricted to areas with very rapid cooling: the upper millimetres of a flow emplaced in air (Gottsmann et al., 2004), the fracture surface of entablatures, and in hyaloclastite and pillow lavas erupted in sub-aqueous or sub-glacial environments (Forbes et al., 2014; Nichols et al., 2009; Potuzak et al., 2008). Here, we propose that columnar joints form in the purely elastic regime of rocks; and that further cooling beyond their incipient formation results in fracture opening and therefore constructs and extends the permeable network that channels fluid flow and accentuates heat exchange.
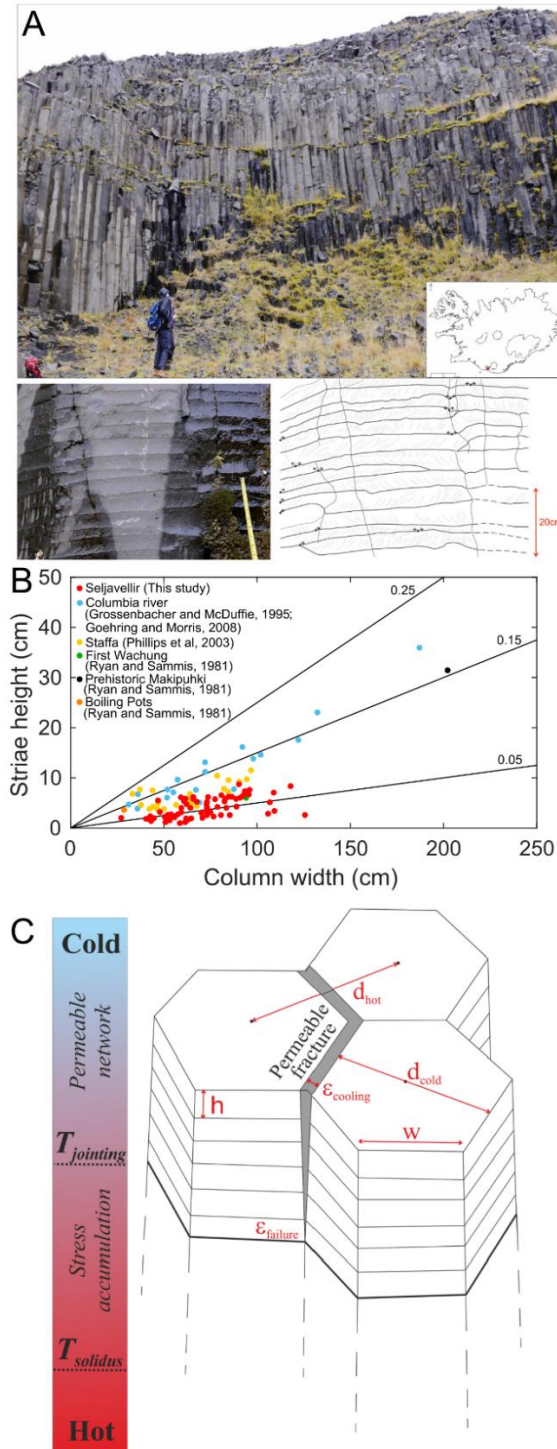
Figure 5-1. Columnar-jointed basalt at Seljavellir. **A)** Columnar joint outcrop locality complemented by a close-up photo and sketch of striae along a colonnade. The exposure is characterised by quadratic to heptagonal cross sectional patterns. The fracture surfaces reveal striae, exhibiting both a rough and smooth portion. **B)** Geometrical relationship between the height of Striae (h) and the width of colonnades (W). The data is plotted against other columnar jointed lavas examined in complementary studies. **C)** Columnar jointing model: The sketch shows that tensile fractures ensue from strain accumulation, induced by thermal contraction ($\varepsilon_{cooling}$) of a length between two focal points (dhot), exceeding the tensile strain limit of the rock ($\varepsilon_{failure}$). The length difference between the columnar joint diameter (d_{cold}) and d_{hot} is the width of the permeable fracture (grey area) available for fluid infiltration.

5.2. Results and discussion

To test the thermo-mechanics of columnar joints we developed a novel experimental setup that allows us to directly observe fracturing in cooling lavas (Supplementary Fig. A. III-1). In the experiment, a tensile fracture is induced by cooling a cylindrical sample of rock from its solidus temperature while locking the ends of the cylinder in position, initially imposing 0 or 5 MPa of normal stress (simulating depth). This setup is designed to simulate elastic stress accumulation by thermal contraction between the static centres of two colonnades. Experiments were conducted on a typical, micro-crystalline basaltic lava from Seljavellir, at the base of Eyjafjallajökull, Iceland (Fig. 5-1A). In nature, the basalt is jointed into colonnades ranging between 30 and 130 cm, and consists of olivine, pyroxene, plagioclase and iron oxide crystals (Supplementary Fig. A. III-2), with a solidus temperature of 980 °C estimated by MELTS (Gaetani et al., 1998) on the basis of the bulk rock chemistry (Supplementary Table A. III-1); this was supported visually by the onset of melting of iron oxides at the starting temperature of the experiments. In the columnar jointing experiments, thermal contraction during cooling resulted in tensile stress build-up during cooling down to temperatures of 890 - 840 °C, regardless of the imposed cooling rate and initial stress (Fig. 5-2). In this temperature range, the tensile stress accumulated (12 - 18 MPa) induced failure, resulting in the creation of a through-going fracture and accompanying stress drop.
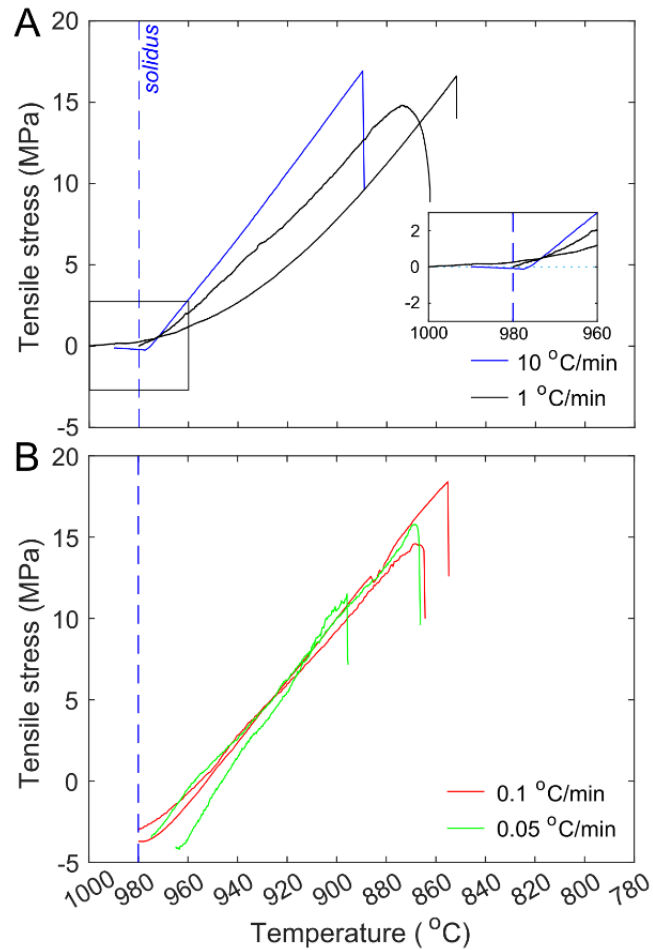
Figure 5-2. Mechanics of columnar jointing. Tensile stress builds up as a rock, locked into a fixed length, cools at a set rate of 0.05 (green), 0.1 (red), 1 (black) and 10 °C.min^{-1} (blue), starting with **A)** no applied normal stress, and **B)** 5 MPa normal stress. The dashed blue line denotes the solidus temperature (980 °C).

To ensure that this temperature window of columnar jointing is realistic, we support our analysis with a dilatometric and mechanical study to assess whether the dynamics of columnar jointing can be explained by comparison of two distinct, static tests. Dilatometric measurements revealed that the expansion coefficient, α, of the basalt tested is isotropic and linear in the temperature range of interest (400 - 980 °C), equating to ~10^{-5} °C^{-1} (Fig. 5-3). Additionally, ambient and high-temperature (820 - 900 °C) uniaxial compressive strength tests conducted at a strain rate of 10^{-5} s^{-1} were used to define the temperature-dependence of the Young's modulus **E** (Fig. 5-4A). **E** was found to evolve according to $\mathbf{E}(T) = 1.371 \times 10^7 T + 2.6157 \times 10^{10}$ in the high-temperature window of columnar jointing (Figure 4B). Finally, ambient and high-temperature (600 - 940 °C) Brazilian tensile tests constrained the tensile strength of our samples to 12 - 21 MPa (Supplementary Fig. A. III-3). Together, these

thermo-mechanical constraints allow us to model the tensile stress build up over a range of undercooling ΔT, via $\boldsymbol{\sigma_T} = \mathbf{E}\alpha\Delta T$ (Jaeger et al., 2009). Our calculations suggest that macroscopic failure would occur at $87< \Delta T <144$ °C, i.e. between 893 and 836 °C (Fig. 5-5) – a temperature window in excellent agreement with the results of columnar jointing experiments developed here (890 - 840 °C; Fig. 5-2).
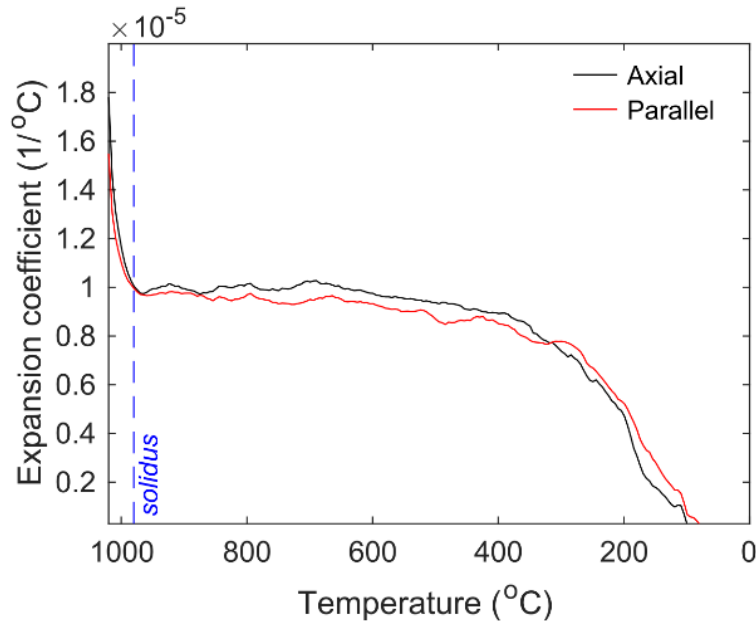
Figure 5-3. Thermal expansion coefficient. Dilatometric measurements showing the linear expansion coefficient of Seljavellir basalt, cored axially and parallel to the column, during cooling from 1000 °C. The dashed blue line denotes the solidus temperature (980 ℃).

Our results are consistent with incipient columnar joint formation at a relatively high temperature, yet within the range at which the magma body is fully elastic. Given that no stress accumulates at temperatures above the solidus (Fig. 5-2A, inset) and that an undercooling (temperature below the solidus) of at least 90 °C is required to induce tensile fracturing, we advance that columnar joints must form and propagate in sub-solidus conditions. This thermal constraint in the sub-solidus regime is in agreement with careful structural and petrographic observations recently put forth (Mattsson et al., 2011), and thus suggest that columnar joints (at least those widespread in basaltic to basaltic-andesite lavas) only require crossing of the glass transition (Ryan and Sammis, 1981a) in fluid-saturated environments.
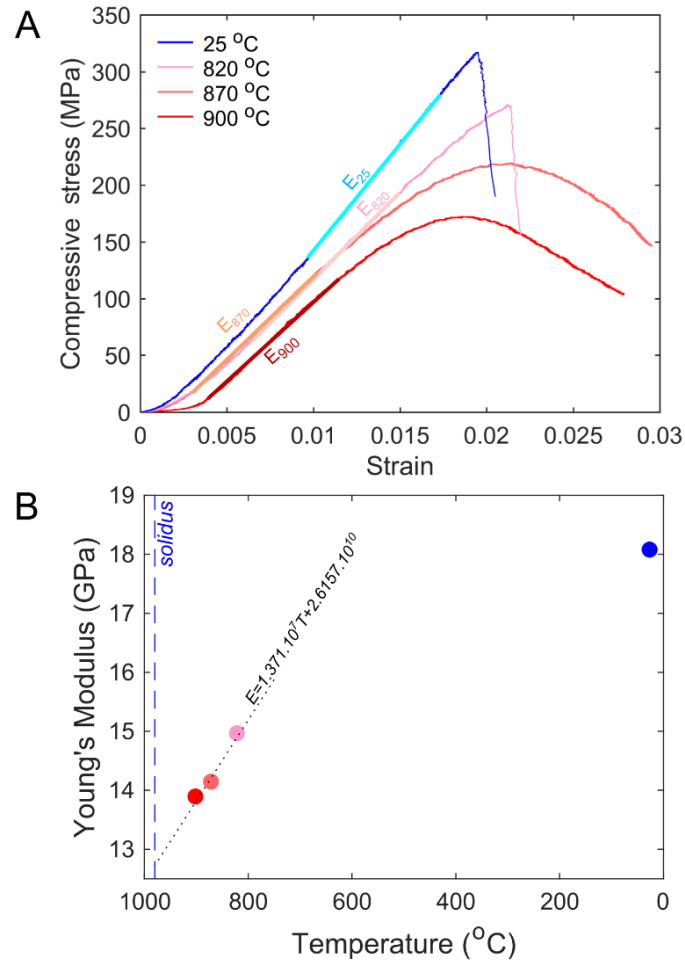
Figure 5-4. Young's modulus variation with temperature. **A)** Mechanical data obtained through uniaxial compressive testing at ambient temperature (blue), 820 (pink), 870 (orange) and 900 °C (red). Young's moduli at different temperatures (E_{25}, E_{820}, E_{870}, E_{900}) are calculated using the linear (elastic) portion of each curve. **B)** Young's modulus values at given temperatures, the change in Young's modulus at high temperature is linear, as depicted by the dotted black line. The dashed blue line denotes the solidus temperature (980 °C).

Studies assessing the thermal history of magma reservoirs, sills and dykes often point towards arguably long cooling timescales if conduction alone is considered, and thus commonly infer the need for external fluid infiltration to increase the cooling efficiency of the magma body (Carrigan, 1986; Degraff and Aydin, 1993; Lister, 1977). The thermo-mechanical constraints introduced here suggest that fluid infiltration may contribute to the thermal budget following columnar joint formation. Here, the data reveal that, after their formation at 890 - 840 °C, fractures would open by continued contraction proportional to an expansion coefficient of ~10^{-5} °C^{-1} down to 400 °C (and at a slower rate below this temperature; Fig. 5-3), thereby constructing the permeable network that allows fluid infiltration in an otherwise largely impermeable rock (measured at 5×10^{-20} m^2 without fractures).
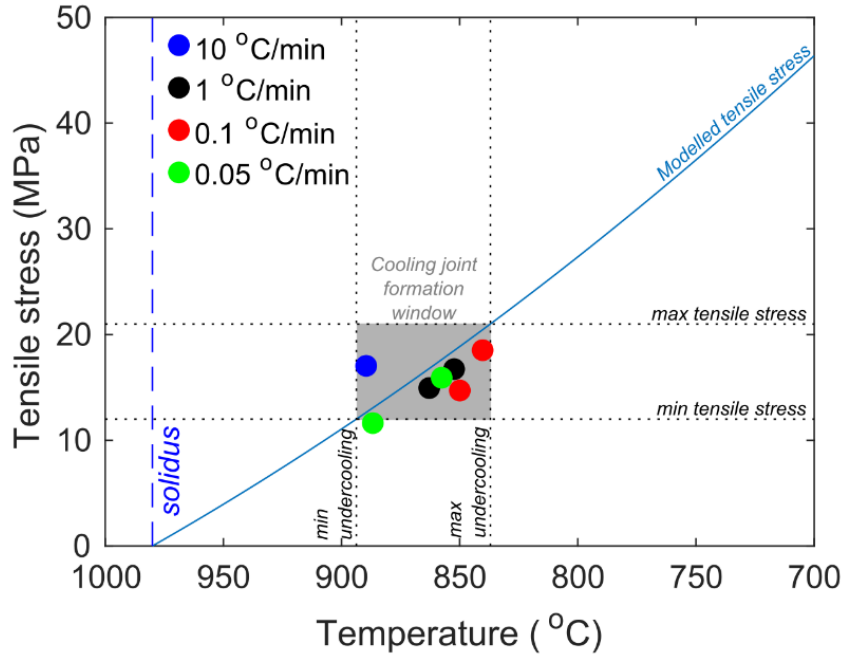
Figure 5-5. Predicted columnar jointing temperature window. The horizontal dotted black lines show the minimum and maximum strength limits obtained through Brazilian tensile tests. The solid blue line shows the calculated tensile stress build-up upon cooling. The intercepts (vertical dotted lines) between the calculated stress curve and the measured strength lines denotes the cooling window necessary to achieve failure. The coloured dots represent the fracturing temperatures achieved during columnar jointing experiments. The dashed blue line denotes the solidus temperature (980 °C).

Using the dilatometric data, we model the evolution of fracture width, **w**:

$$\mathbf{w} = \sum_{T_s}^{0} \alpha_{(T)} d_{hot} [T_s - T] \tag{5.1}$$

where T_s is the solidus temperature window (980 °C), T is the temperature (°C), $\boldsymbol{\alpha}_{(T)}$ the expansion coefficient at a given temperature (°C^{-1}) and d_{hot} is the column size observed at Seljavellir (0.3-1.3 m). Our calculation of the final fracture width shows good agreement with values of 1.9 and 8.3 mm measured in the field (for columns of 0.3 and 1.3 m width, respectively; Fig. 5-6A). Knowing the fracture width at different temperatures allows us to predict the permeability of such a fracture system, $\boldsymbol{\kappa_s}$ (in m^2) at unconfined conditions, using a modified version of equation 7 from Lamur et al. (2017) (eq. 5.2 to 5.9; see also Supplementary Fig. AIII-4):

$$\kappa_s = \kappa_\Phi + \frac{\rho_f \bar{l} \bar{w}^3}{A_i} \tag{5.2}$$

where κ_Φ is the permeability of the intact rock, ρ_f the fracture density, $\bar{l}$ the average fracture length, $\bar{w}$ the average fracture width and A_i the area of interest.

Considering the system shown in Figure 4 and applying it to Seljavellir basalts, we define the following set of parameter. The length of an edge, s, of an hexagon at maximum column width, d_{hot}, is given by:

$$s = \frac{d_{hot}}{2 \cos(\alpha)} \tag{5.3}$$

where $\alpha = 30°$ in a regular hexagon. Hence the length l of a fracture around a column is:

$$l = 6\,s = \frac{3\,d_{hot}}{\cos(\alpha)} \tag{5.4}$$

The fracture density is given by:

$$\rho_f = \frac{N_{col}\,l\,w}{A_i} \tag{5.5}$$

where the number of columns N_{col} is determined by:

$$N_{col} = \frac{total\ area}{area\ of\ one\ column} = \frac{A_i}{2\sqrt{3}\frac{d_{hot}^2}{2}} = \frac{A_i}{\sqrt{3}d_{hot}^2} \tag{5.6}$$

Substituting S3 and S5 into S4, we find that the fracture density is given by:

$$\rho_f = \frac{3\,w}{\sqrt{3}\,d_{hot}\,cos(\alpha)} \tag{5.7}$$

Given that the fracture width evolves following equation 1, we can then rewrite S1 to model the permeability evolution as a function of fracture width and cooling:

$$\kappa_s = \kappa_\Phi + \frac{9\,w^4}{A_i\,\sqrt{3}\,\cos(30°)} \tag{5.8}$$

which can be simplified to:

$$\kappa_s = \kappa_\Phi + \frac{6w^4}{A_i} \tag{5.9}$$

where κ_Φ is the permeability of the intact rock (5×10^{-20} m^{-2}) and A_i is the cross-sectional area of a columnar jointing reservoir (in m^2). Thus, we calculate that the permeability of columnar-jointed magmatic aureoles is highly dependent on the column size, reaching 10^{-14} to 3×10^{-12} m^2 (for the maximal fracture widths considered) in the absence of effective pressure (i.e., difference between confining pressure and pore pressure) near the Earth's surface or in fluid-rich environments characteristic of shallow volcanic, geothermal and hydrothermal systems (Fig. 5-6B). Hence the formation of columnar joints may strongly influence hydrothermal circulation and therefore, the cooling history of magmatic bodies. The permeability gradient

observed along a cooling column would allow sufficient water infiltration to trigger convection-driven cooling (Lister, 1977) and eventually trigger quenching of liquid in the flow core, providing a mechanism for the formation of glass films observed along the entablatures (Forbes et al., 2014).
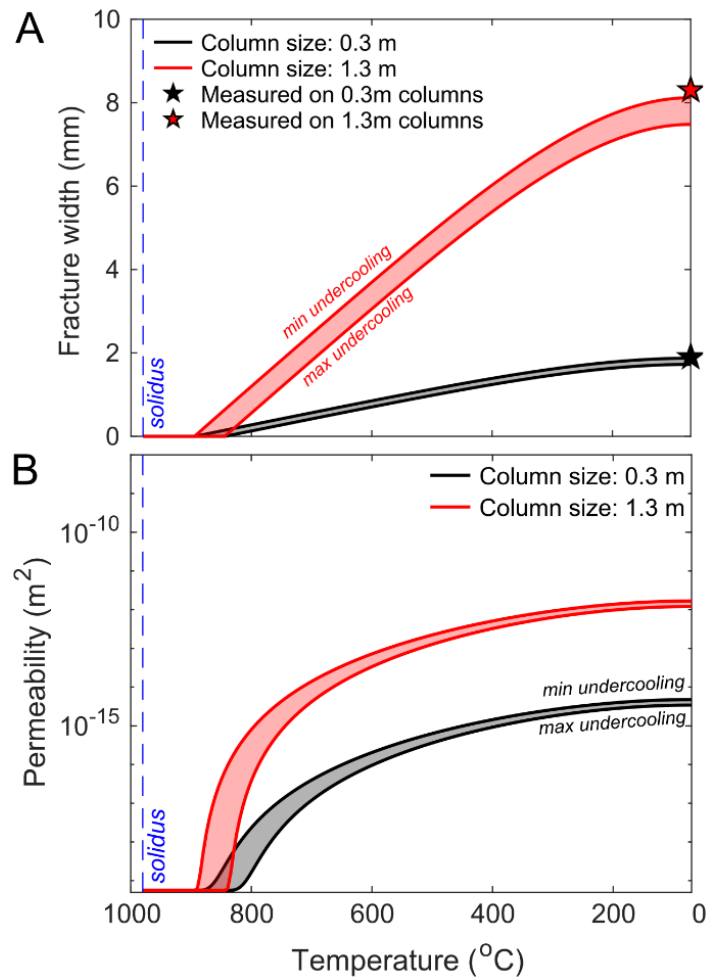
Figure 5-6. Fracture width and permeability evolution of columnar jointed rocks. **A)** Fracture width evolution in a magmatic body developing columns of 0.3 (black) and 1.3 m (red) diameter. The black and red star show the average fracture width, measured in the field, for 0.3 and 1.3 m diameter columns respectively. **B)** Permeability increase due to cooling and induced fracture opening in 0.3 (black) and 1.3 m (red) diameter columns. In both **A)** and **B)** the dashed blue line denotes the solidus temperature (980 ℃).

5.3. Conclusions

This study presents the first direct measurements to show that columnar joints form in the solid state, at high-to-moderate temperatures, which leads to the construction of a permeable network with enhanced further cooling. We urge the integration of the combined thermo-mechanical data into numerical simulations of natural cooling systems to refine the limits of fluid circulation in volcanic, geothermal and hydrothermal environments.

5.4. Methods

Columnar jointing experiments were conducted in a 5969 Instron® press equipped with a custom furnace designed by Severn Thermal Solutions, which permits Infrared (IR) imaging of samples through a sapphire window. For this purpose, 170 mm long samples, 16 mm in diameter were cored out and the central 35 mm length of the sample was ground to a thinner dog-bone geometry with a diameter of 8 mm. During sample heating (at 5 °C.min^{-1}) the grips were allowed to freely retract with sample expansion. Once the temperature equilibrated (after 30 min), the grips were locked in position and the furnace was programmed to cool at set rates of 0.05, 0.1, 1 or 10 °C.min^{-1}, whilst the press monitored tensile stress incurred by sample contraction. A FLIR SC6540 IR thermographic camera imaged sample temperature during cooling.

Dilatometric measurements were performed in a Thermo-Mechanical Analyser 402F1 – Hyperion from Netzsch GmbH. The expansion/ contraction of a 6 mm diameter by 5 mm high cylindrical sample was monitored at a heating/ cooling rate of 2 °C.min^{-1} (up to 980 °C) with a spatial resolution of 0.125 nm, whilst applying 3 mN of load. The sample expansion was corrected for sample holder expansion by subtracting a baseline run on a sample of standard alumina at the same heating/ cooling rate.

Brazilian tests at room and high temperatures were conducted to assess the tensile strength (Mahabadi et al., 2010) in a 8800 Instron® press equipped with a furnace designed by Severn Thermal Solutions. Disc-shaped samples with a diameter of 40 mm and a thickness of 20 mm,

were placed edge-on in the press and heated at 2 °C.min^{-1}. After 1 hr of thermal equilibration at the target temperature, the cylindrical sample was diametrically compressed at a rate of 4x10^{-4} mm.s^{-1} with force and deformation monitored until complete failure.

The temperature dependence of the static Young's Modulus was constrained by conducting a series of uniaxial compressive strength tests in a 8800 Instron® press. Cylindrical samples with a length of 20 mm and diameter of 10 mm were placed between the pistons of the press and heated to desired temperatures (820 – 900 ˚C) at a rate of 2 °C.min^{-1}. Once thermally equilibrated (30 minutes), the cylinders were deformed at a rate of 10^{-5} s^{-1} and stress and strain were monitored. The linear portion of the stress-strain data were used to constrain the static Young's modulus.

The permeability of the rock was measured in a Sanchez hydrostatic vessel, using water pressures (in) of 2.1 MPa and (out) of 0.1 MPa (thus a pore pressure gradient, $\Delta P = 2$ MPa), and 6 MPa confining pressure exerted by oil on a jacketed cylindrical sample (25 mm diameter). Water discharge, Q (in m^3.s^{-1}) was monitored and used to calculate the permeability, κ, via Darcy's equation (Darcy, 1856, 1857):

$$\kappa = \frac{Ql\eta}{A\Delta P} \tag{5.3},$$

where A is the sample cross-sectional area (m^2), l the sample length (m) and η the viscosity of the fluid (0.001 Pa.s for water).

Chapter 6:

Timescales of fracture healing and strength recovery in magmatic liquids

In this Chapter, I investigate the timescale of fracture healing in magmatic liquids and discuss the implications of dynamic permeability variations due to this process on the cyclic activity observed at silicic volcanoes.

Publication status

Authorship: Anthony Lamur[1], Fabian B. Wadsworth[1, 3], Jackie E. Kendrick[1], Yan Lavallée[1]

Affiliations:

[1] Experimental Volcanology Laboratory, Department of Earth, Ocean and Ecological Sciences, University of Liverpool, 4 Brownlow Street, L69 3GP, United Kingdom

[3] Earth and Environmental Sciences, Ludwig Maximilian University – LMU-Munich, Theresienstrasse 41/III, 80333 Munich, Germany

Paper abstract

Cycles of fracture and healing in magma are important controls on outgassing timescales and short-term cyclicity in eruptive behavior at silicic volcanoes. Here, we present experimental results to assess the kinetics and constrain the mechanisms controlling fracture healing, applying it to the longevity of permeable fractures and the recovery of strength in fractured systems. Experiments used two standard glasses at a range of temperatures above their glass transition, at magmatically relevant viscosities of $10^8 - 10^{12}$ Pa.s. Healing occurred when the ends of two hot, plane-parallel rods were pushed against one another under a constant stress. By directly pulling the rods apart we recorded the stress required to fracture the partially healed interface. For contact times less than the viscous relaxation time, the melt interfaces acquire no tensile strength. As the time available for healing is increased, strength non-linearly recovers towards that of unfractured glass. We parameterize the healing kinetics as a two-stage process; (1) first the fracture surfaces must wet one another and (2) diffusion across the interface acts to weld it shut. Both stages increase mechanical strength, with regime 1 viscously limited, and regime 2 diffusively limited. During welding, we observe that micro-pores are trapped along the fracture plane, which may inhibit complete healing and provide a textural record of relict fracture planes in volcanic glass. We conclude that at magmatic conditions, fracture healing is efficient and could rapidly seal outgassing pathways over eruptive timescales, contributing to cyclic behavior associated with recurring gas-and-ash explosions and outgassing events.

6.1. Introduction

Material failure is a key problem in a wide range of science and engineering disciplines (Paterson and Wong, 2005; Webb and Dingwell, 1990) as it is central to our understanding of anthropogenic and natural disasters such as earthquakes and volcanic eruptions. The rupture and strength of geomaterials has been described as a function of material constituents such as crystals, melt (at high temperature), glass (at low temperature) and porosity, as well as of external factors such as temperature and stress conditions (see Paterson and Wong (2005) for a review). Micromechanical models suggest that pores (Sammis and Ashby, 1986) and cracks (Ashby and Hallam, 1986) act as concentrators of stress and are therefore the locus of fracture propagation when the stress overcomes a critical fracture stress (e.g. Isida and Nemat-Nasser, 1987). In shallow volcanic conduits, ascending magma can undergo multiple fracture and

healing cycles (Tuffen et al., 2003), producing diagnostic, cross-cutting relict fracture textures (Goto, 1999; Tuffen and Dingwell, 2005) thought to contribute to outgassing or minor gas-and-ash venting episodes (Kendrick et al., 2016), and which generate low-frequency seismic signals precursory to large eruptions (Neuberg et al., 2006). Despite being central to the occurrence of geophysical and geochemical signals at active volcanoes, there is only limited knowledge of the processes and timescales required to heal fractures in silicate melts (e.g. Yoshimura and Nakamura, 2010b).

In both volcanic and tectonic settings, relict evidence for the healing process has been found in heterogeneities such as trails of fluid inclusions in crystals (Roedder, 1984) or micro-bubbles and microlites (Gardner et al., 2017; Tuffen and Dingwell, 2005) in silicate glasses (see Fig. 6-1).
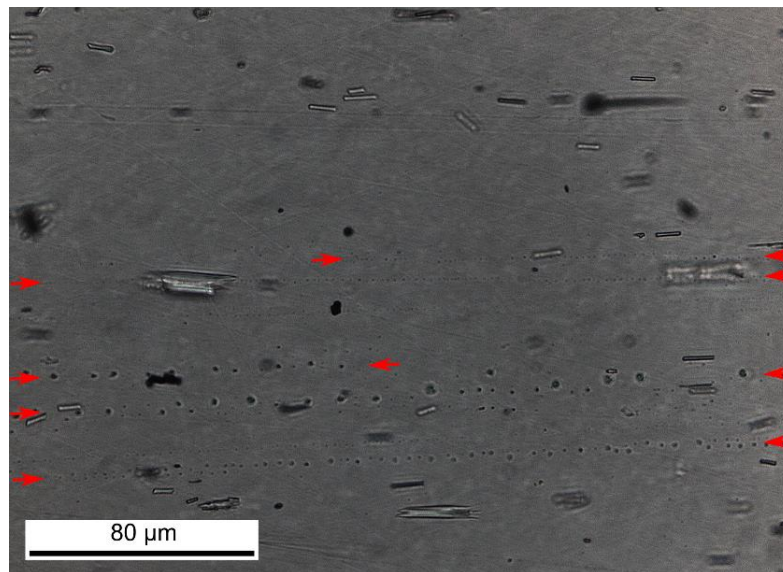
Figure 6-1. Photomicrograph of an obsidian from the big obsidian flow at Newberry volcano, USA, in plane polarised light. Each set of red arrows defines the extent (visible on the image) of linear bubble trails, which represent the occurrence of at least 5 healed fracture planes in the area of interest.

Magmas are viscoelastic materials which readily fracture when imposed shear stresses result in strain rates that exceed the inverse of the viscous relaxation time τ (Webb and Dingwell, 1990). The viscous relaxation time τ is proportional to the viscosity η and shear modulus at infinite deformation frequency G_∞ by:

$$\tau = \frac{\eta}{G_\infty}$$

(6.1),

where G_∞ may be approximated at 10^{10} Pa (Webb and Dingwell, 1990). Unrelaxed elastic behaviour has been noted to occur when strain rates locally exceed $10^{-3}/\tau$ and material failure occurs when strain rates exceed $10^{-2}/\tau$ (Webb and Dingwell, 1990). This strain-rate limit therefore represents a critical parameter to constrain volcanic stresses and timescales from interpretation of fracture events preserved in eruptive products.

The process of fracture healing has been studied for some particular glasses and ceramics (Gupta, 1976; Jud et al., 1981; Michalske and Fuller, 1985; Wool and O'Connor, 1981; Yoshimura and Nakamura, 2010b), salt rocks (Fuenkajorn and Phueakphum, 2011), and quartz crystals (Smith and Evans, 1984). Despite focusing on different systems, these studies suggest that healing involves a time-dependent diffusive exchange of mass across the interface, which manifests as a strength recovery of the contact interface (e.g. Wool and O'Connor, 1981).

The healing process may be complicated by the time-dependent sintering of fragments caught along the fracture plane, as observed in tuffisites found in exhumed conduits (Tuffen and Dingwell, 2005) and extrusive lavas (Cabrera et al., 2011; Castro et al., 2012; Kendrick et al., 2016). Sintering is often driven by surface tension at the liquid-gas interfaces internal to the particulate material and results in an increase in the strength of material (Vasseur et al., 2013), concomitant with a decrease in permeability (Kendrick et al., 2016; Wadsworth et al., 2016). Despite this body of work, there remains no robust description of fracture healing timescales that can be compared with volcanic phenomena and associated signals.

6.2. Materials and methods

We performed fracture healing experiments on two standard borosilicate glasses with well constrained temperature-viscosity relationships: (1) SRM 717a from the National Institute of Standards and Technology (NIST), and (2) SDGS-3.3 from Schott Duran®. First, we measured the tensile strength σ_0 of each glass using direct tensile tests on dog-bone samples (ISRM (1978)) with 8 mm diameter, widening to 16 mm in the grips and 35 mm length, using a 5969 Instron® uniaxial press, adapted with a split furnace from Severn Thermal Solutions. A sample was loaded into the mechanical grips of the press and heated up at 5 ˚C.min⁻¹ until target

temperatures (560 ℃ for NIST and 590, 630, 645, 730 ℃ for SDGS); the sample was thermally equilibrated over a period of 30 min and direct pull was conducted at an axial strain rate of 10^{-1} s^{-1}.

Subsequently, fracture healing experiments were performed on samples in which an artificial fracture was cut through the center perpendicular to the long-axis and the fracture surfaces were ground flat (Fig. 6-2A). The sample pair was then loaded into the mechanical grips of the press and heated up to desired temperature (Fig. 6-2A). The upper sample was forced into contact with the lower sample and a stress of 1 MPa, chosen to reproduce shallow conduit pressures, was held for variable experimental timescales of $0.5 < t < 15000$ s before being pulled apart at a strain rate of 10^{-1} s^{-1}. Here, the measured peak stress required to fracture the partially-healed sample pair was used and compared to the tensile strength of the melt (for a given temperature) as a measure of healing efficiency. Note that we accounted and corrected for the occurrence of viscous bulging of the contact zone by optically monitoring changes in contact area during each test.
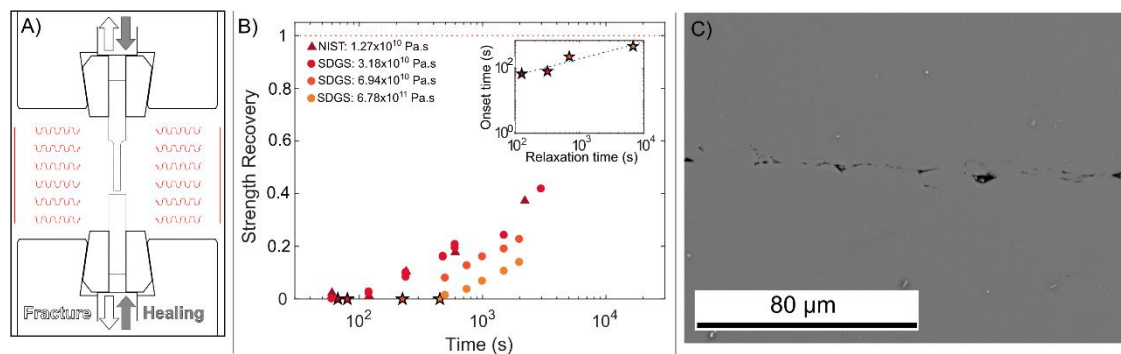
Figure 6-2. A) Experimental setup for cyclic fracture (white arrow) and healing (grey arrow) experiments; **B)** Normalized tensile strength recovered as a function of contact time for experiments on NIST (triangles) and SDSG (circles) melts at different temperatures (and thus viscosities), where 1 represents the tensile strength of the melt measured at high temperature. The stars represent the onset of strength recovery at different temperatures. *Inset:* relationship between the onset time and the relaxation timescale of the glasses. **C)** Photomicrograph of a pore trail trapped along the contact interface for a SDGS sample healed for 600 s at a viscosity of 6.94x10^{10} Pa.s.

6.3. Results and discussion

Tensile strength tests on NIST 717a and SDGS constrained σ_0 of these glasses to be 24.99 ± 1.83 and 32.19 ± 1.24 MPa, respectively (Supplementary Fig. A. IV-1). Fracture healing experiments showed that strength recovery, tracked by σ/σ_0, is non-linearly dependent on time (Fig. 6-2B). We found that within experimental error, σ did not rise above zero until a critical onset time λ_c. In order to predict λ_c for each experiment we found good agreement with the data and fit a purely empirical function $\sigma/\sigma_0 = Aln(t) + B$ and extrapolating to $\sigma/\sigma_0 = 0$. Using the known temperature-dependence of viscosity for the liquids used, and inferring that this onset time is a viscous wetting process related to the relaxation time, we can show empirically that the onset time of strength recovery can be approximated for viscous flat fracture planes as a power-law dependence on the viscous relaxation time,

$$\lambda_c = C(\tau/\beta)^\alpha \tag{6.2},$$

where $C = 58.95$ and $\alpha = 0.51$ are dimensionless and both are determined empirically from our experiments, with $\beta = 1$ s. During this process we show that micrometric pores are trapped along the interface (Fig. 6-2C), possibly preventing the limit $\sigma \to \sigma_0$ being met and providing diagnostic textural evidence for a relict fracture plane.

At times greater than λ_c, σ/σ_0 rises above zero and non-linearly toward unity. We show that if we normalize time by λ_c, we can remove the temperature (or viscosity) dependence of the process, producing a universal trend of $\sigma/\sigma_0 = f(t/\lambda_c)$, consistent with similar processes occurring in polymer liquids at room temperature (Wool and O'Connor, 1981). In Figure 6-3 we show that the slope of the first part of this process after λ_c is approximately 5/4 and the latter part of the process evolves toward a slope of 1/2.
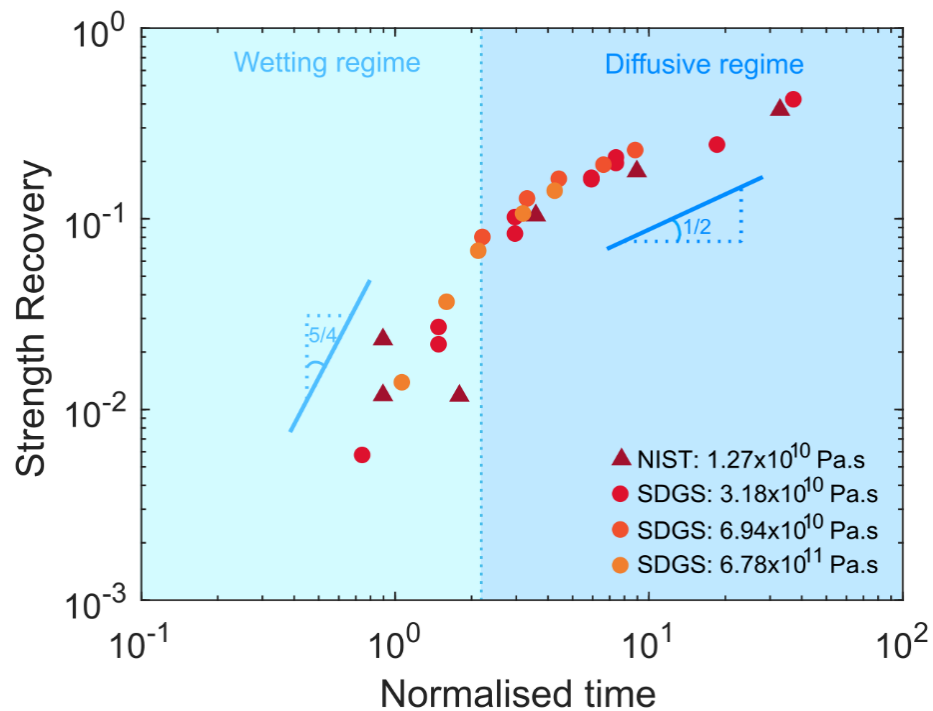
Figure 6-3. Tensile strength recovery against normalised time (t/λ_c). The break in slope shows that healing occurs in 2 stages. The first stage of surface wetting (light blue region), controlled by viscous wetting along the interface, has a characteristic slope of 5/4. The second stage (dark blue region) is governed by diffusive mass exchange across the interface and is described by a slope of 1/2.

Wool and O'Connor (1981) demonstrate that a dependence of normalized strength on time of 5/4 is consistent with theoretical arguments for the early part of a crack-healing process in which the two fracture planes are completing full wetting while also exchanging mass by diffusion. Following this regime the late-stage of the fracture healing process involves a time dependence consistent with a slope of 1/2 (Jud et al. (1981); Wool and O'Connor (1981)). This late-stage is characterized by diffusive exchange of mass once wetting has completed. Here we postulate that the relative length of the initial and late phases scale with the initial fracture roughness, the wettability and the effective diffusivities of cations across the interface. Our experiments demonstrate these theoretical regimes of behavior.

6.4. Implications for silicic volcanic eruptions

Fracture healing may be an important control on the mechanisms of shallow silicic eruptions (e.g. Castro et al., 2012) and flow emplacement (Cabrera et al., 2011). Extensive, connected fracture networks are the primary outgassing pathway in silicic magmas (Berlo et al., 2013; Cabrera et al., 2011; Castro et al., 2014). Fracturing and increased gas release have been argued to be important controls on shifts in eruptive style from explosive to effusive (e.g. Cabrera et al., 2011; Castro et al., 2012; Edmonds et al., 2003; Gonnermann and Manga, 2003; Yoshimura and Nakamura, 2010a). As proposed by Cabrera et al. (2011), and experimentally shown by Yoshimura and Nakamura (2010a), the formation of dense, silicic obsidian might result from repeated fracture-healing cycles. During these cycles, permeability is enhanced through the formation of macro-fractures (e.g. Lamur et al., 2017), allowing rapid outgassing and providing the pore pressure decrease necessary for the collapse of the vesicular magma. At longer timescales, the macro-fracture is relaxed and healed, producing characteristic trails of isolated pores along the fracture interface (Figure 3), reducing the permeability to gas flow , thus allowing the system to build-up pore pressure (e.g. Saubin et al., 2016). The longevity of a fracture is therefore a key constraint on the outgassing time window before pressure can increase again in that area.

Our work has further shown that healing is a kinetic process controlled by the structural relaxation and diffusivity of viscoelastic melts; thus it is essentially stress (or pressure) invariant. The pressure acting on a closing fracture may however impact the solubility of volatiles trapped along the melt interfaces (Zhang, 1999) – shifting from permeability-controlled to diffusion controlled volatile transfer (Yoshimura and Nakamura, 2010a) – which may locally alter the melt viscosity (e.g. Hess and Dingwell, 1996), thereby enhancing healing; yet, this process is kinetically limited. Hence, we propose that the time dependence of strength constrained here is a first-order timescale of relevance to understanding inter-explosion times at a given vent or to interpreting geophysical signals associated with volcanic unrest.

The timescale of fracture healing may be complicated by the presence of particulate material such as volcanic ash trapped along fracture planes or in fracture networks. Sintering of partly crystalline particles (Kendrick et al., 2016) or glass fragments (Vasseur et al., 2013), and compaction welding under stress (Heap et al., 2014a; Quane et al., 2009) occurs over

timescales proportional to the particle size distribution in the fracture, the bulk viscosity of the particles, and the surface tension between the particles and the interstitial pore phase (Wadsworth et al., 2014). Strength recovery through sintering for a range of volcanic ash particle sizes (0.001 – 1 mm) varies as a function of relaxation time (eq. 6.1), as shown in Figure 6-4. The different slopes suggest that pore pressure build-up due to healing/ sealing of the permeable fracture network is temperature dependent, with particle sintering being more rapid than particle-free fracture healing at higher temperatures (i.e., at short relaxation times) and fracture healing being more efficient than sintering in cooler systems (with long relaxation timescales), a factor which could drastically influence sealing of degassing pathways in volcanic systems at different temperatures.
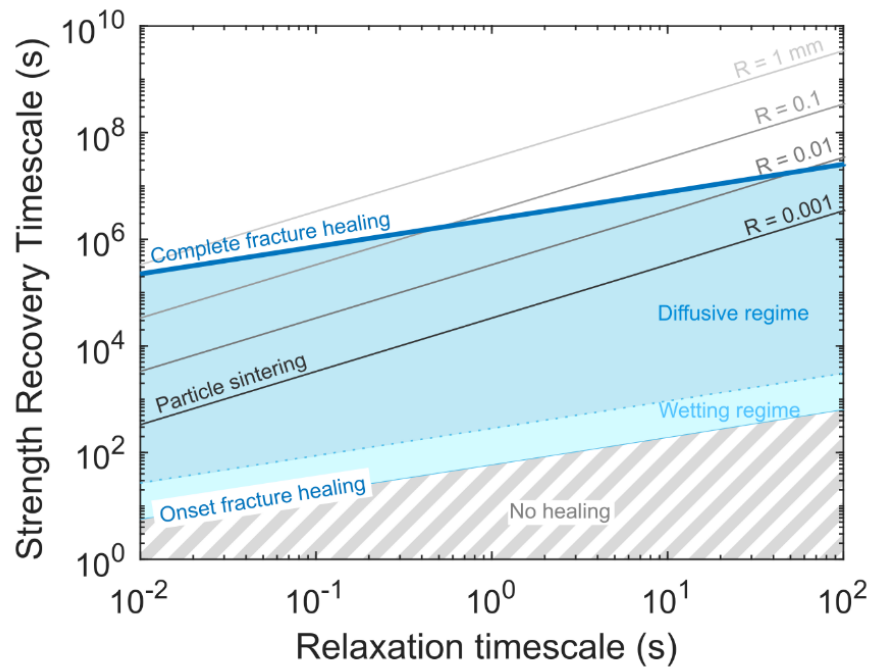
Fig 6-4. Strength recovery timescales for particle-free and particle-bearing fractures as a function of relaxation timescale of the melt. The onset of strength recovery at different viscosities is depicted by the thin blue line, below which no fracture healing is achieved (striped area). The two stages of healing, wetting and diffusive regimes, are respectively shown in light and dark blue, and complete fracture healing is represented by the thick blue line. The full strength recovery of fractures bearing sintering particles (of radius, 0.001<R<1 mm) appear as grey lines, following the relationship by Vasseur et al., (2013). The contrasting relationships suggest that at high temperatures (when relaxation timescales are short) fracture healing is more efficient when particles are present along the interfaces, whereas at low temperature (when relaxation timescales are long) fracture healing is more efficient in absence of particles along the interface.

During ascent, magma shearing can result in spatial variations of viscosity across a conduit, thus affecting the occurrence of fracture healing processes. For example, viscous energy dissipation (Costa and Macedonio, 2003; Mastin, 2005) or frictional heating (Kendrick et al., 2014a) in regions of strain localization near conduit margins can result in locally lower viscosities and thus reduced fracture healing times (Yoshimura and Nakamura, 2010a), as shown here; such variations may lead to variably efficient permeable pathway closure and strength recovery in marginal shear zones, thus affecting outgassing and pressure distribution in volcanic conduits.

6.5. Conclusions

Conducting novel fracture healing experiments on silicate liquids at magmatic viscosities, we demonstrate that healing initiates after a timescale proportional to the melt relaxation timescale (hence viscosity). Beyond this point, healing begins via wetting of the surface, which transitions into a diffusional regime. During this process, soluble volatiles may get trapped as a trail of bubbles, which can get resorbed into the melt at timescales longer than the diffusion timescale of the volatile species, thus impacting the strength recovery magnitude. The findings suggest that at volcanoes, fracture healing, even when partially complete, may be an efficient process contributing to eruptive timescales.

Chapter 7:

Implications and future work

7.1. Summary of results

In this project, I have investigated the development, impact and longevity of fractures in volcanic materials present in magmatic, volcanic and geothermal settings, using a combination of standard methods and new experimental designs that aim at replicating the stress build-up or relaxation in these environments. I have additionally characterised fluid flow in fractured rocks through permeability measurements at atmospheric and low confining pressures to replicate shallow conditions.

In Chapter 4, I demonstrated that fractures play a crucial role in localising fluid flow by increasing the permeability. In detail, I produced a large permeability dataset over a wide range of volcanic rocks with porosities varying from 1 to 42 % and at different effective pressures. While the permeability of intact volcanic rocks shows a similar relationship to porosity as previous studies (Dasgupta et al., 2000; Klug and Cashman, 1996; Mueller et al., 2005; Rust et al., 2004; Saar and Manga, 1999), the permeability of volcanic rocks is drastically enhanced by the presence of a macro-fracture, with an increase of up to 4 orders of magnitude at the low porosity end. On the other hand, at high connected porosities, the permeability only slightly increases or remains similar to that of the intact rock. These results show similarities with those of Heap and Kennedy (2016), in that low porosities rock showing large increase in permeability and that the effect of the fracture is decreased with increasing porosity. I further attributed these changes in permeability to different regimes where the macro-fracture has a different impact, a conclusion similar to that drawn by Matthäi and Belayneh (2004) in their numerical simulation. The regimes I defined showed that at low initial connected porosities (<11 %) pre-existing pore structures dominated by micro-fractures form a tortuous and relatively low permeability network, resulting in the experimentally-imparted macro-fracture carrying all the fluid flow. Between 11 and 18 % connected porosity, I observed that pre-existing pore connectivity (which can be highly variable at this porosity) as well as the macro-fracture (to varying degrees depending on the pre-existing structure)

contribute to the fluid flow. Finally, above 18%, the pore connectivity is developed well enough so that the macro-fracture has little to no effect on fluid flow. These different regimes reflect the interaction of multiple processes (vesiculation, fracturing through shearing, thermal stressing, etc.) to form complex permeable pathways. As such, I concluded that a change in micro-structure cannot be ascribed to a single porosity value (Farquharson et al., 2015) but rather to a porosity range where pore connectivity becomes increasingly dominant over micro-cracks, resulting in the permeability-porosity relationship for volcanic rocks being best described by a single power law, with an acknowledgement of the inherent scatter resulting from diverse formation mechanisms.

Interestingly, when comparing the permeability of intact and fractured samples, I observed that increasing the effective pressure was not sufficient to retrieve the intact rock permeability. In other words, the mechanical closure of a fracture is not able to prevent fluid flow through the fractured system. I used this data to model the fracture width evolution with increasing effective pressure, and show that most of the mechanical closure of the macro-fracture occurs at low effective pressure (<3.75 MPa), and that little further closure occurs up to 28.75 MPa. I finally derived a relationship linking the permeability of a fractured system to the permeability of the intact rock, the fracture density, averaged fracture geometry (width and length) and the contact area with a permeating fluid reservoir at variable effective pressure, to provide a unique solution for the permeability of a body with known dimensions. This relationship has then been used and modified to model the permeability evolution of a columnar jointing magmatic body in Chapter 5.

Chapter 5 examines the temperature window for the formation of columnar jointing in a magmatic body and further models the permeability evolution of a columnar jointed body with hexagonal fractures widening upon cooling. In nature, a cooling magmatic body can develop chilled margins during emplacement in a colder environment (Huppert and Sparks, 1989). Further contraction upon cooling leads to the accumulation of tensile stress that may result in the formation of. Here, I investigated this process using uniquely designed experiments where rods of hot basalt (locked in position by grips) were cooled to induce contraction at the centre of the rods until failure. I demonstrated that columnar joints in basaltic flows/ bodies always form in the elastic regime, as no tensile stress build-up was recorded above the solidus temperature of 980 °C. This contradicts the hypothesis that cooling joints necessarily form by crossing the glass transition of the melt (Forbes et al., 2014; Lore et al., 2000a; Phillips et al.,

2013; Ryan and Sammis, 1981a). Mechanical data also show that, irrespective of the induced cooling rate (0.05 to 10 ℃/min), tensile fractures form between 840 and 890 ℃ (or 90 to 140 ℃ below the solidus temperature) in this basalt. Using a second method, combining thermal expansion and Young's modulus at high temperature to model the stress-strain relationship during cooling, alongside tensile strength data from Brazilian tests, I defined a temperature window for columnar joints formation in this basalt of 836-893 ℃ that correlates well with the mechanical data. This approach implies that knowing the thermal and mechanical characteristics of a rock may help to determine the temperatures at which cooling joints can form. With the temperature window defined, I then computed the fracture width evolution between two columns using the expansion coefficient and calculated the fracture density in a columnar jointed reservoir. Importantly, the final fracture width calculated, at a given column size, matches with fracture widths measured in the field. Hence, I was able to model, by modifying equation 4.7 in Chapter 4, the permeability evolution with temperature of a columnar jointing body of hexagonal fractures widening upon cooling (Eq. 5.2). I showed that from the temperature of formation of the columnar joints, the permeability of the magmatic body drastically increases and that the maximum final permeability is dependent on the column width. This result has important implications for the thermal history of magmatic bodies, as the formation of fractures triggers a positive feedback loop between fluid infiltration (due to enhanced permeability) and development of joints by cooling (due to increased thermal exchanges between the fluids and the magmatic body), promoting stronger advection of the infiltrating fluid and enhancing the cooling of the magmatic body (Marsh, 1989).

As shown in Chapters 1 and 5, macro-fractures in magmatic, volcanic and geothermal systems, can form in both rocks and hot, viscous liquids (Lavallée et al., 2008). In Chapters 4 and 5, I showed that these fractures contribute significantly to fluid flow and that mechanical closure is insufficient to retrieve intact rock permeability values. However, field evidence has shown that fractures can seal or heal (Castro et al., 2012; Tuffen and Dingwell, 2005). Consequently, in Chapter 6, I present the results of fracture healing experiments, in standard borosilicate glasses, specifically designed to improve the understanding of the mechanics and kinetics (i.e. timescales) required for a fracture to heal. By monitoring the strength recovery of a flat (fractured) interface as a function of contact time, I showed that timescales for fracture healing and strength recovery are viscosity and diffusion dependent. After the work of Tuffen et al. (2003), fracture healing in magmatic liquids was thought to start as soon as the time of contact exceeded the relaxation timescale of the melt. Here, I demonstrated that fracture healing starts

after a characteristic time proportional to the relaxation timescale. After this characteristic time, the healing process occurs in two distinct stages, with the first 10 % of strength recovery are dominated by viscous flow along the fracture interface (wetting regime), followed by diffusive exchange across the fracture plane (diffusive regime). The work I present in chapter 6 helps to refine the timescales of repeating fracture-healing cycles through the quantification of strength recovery and the longevity of permeable fractured pathways in magmatic, volcanic and geothermal systems. The constraint defined here using silicate liquids, is directly applicable to fracture healing in magmatic systems, but also to other fractured systems, as it is based on an understanding of diffusive exchange, which operates at all temperatures in all materials, though at different rates (Freer, 1981).

7.2. Implications of permeability variation in magmatic, volcanic and geothermal systems

The development and longevity of fractures influences the circulation of fluids in magmatic, volcanic and geothermal systems. For instance, as shown in Chapter 4, I demonstrated how the proportion of fluid carried by a macro-fracture decreases with porosity, and how mechanical closure of a fracture is insufficient to retrieve the permeability of the intact rock. This has important implications for the circulation of deep hydrothermal fluids (Benderitter and Elsass, 1995), where the presence of macro-fractures favour fluid flow, in otherwise low permeability, compacted environments. Additionally, the direction of the fracture plane with respect to that of the pressure gradient driving fluid flow is equally important. For instance, fractures sub-perpendicular to the pressure gradient can drain the fluids away, affecting convection. In turn, this may influence geothermal energy production, (re-)activate a fault plane thus generating slip and seismicity (Calò et al., 2016). If slip takes place, a fault may further develop a gouge that may seal the permeable pathway (Faoro et al., 2009; Faulkner and Rutter, 2003). Hence, understanding the development and longevity of macro-fractures is beneficial during the exploitation of geothermal energy. Indeed, targeting zones of enhanced permeability (fractured rocks), or inducing damage in high pore pressure regions by hydrofracture, could increase the production rate of geothermal wells (Capuano Jr et al., 2008; Majer et al., 2007) and reduce both drilling time, maintenance and costs (Wyering et al., 2017).

Volcanic edifices are complex and highly anisotropic (Acocella, 2015) as a result of the successive emplacement of lava flows and/ or fragmented material deposits. This results in the formation of a variably porous and mechanically heterogeneous stratigraphic sequence that, under mechanical loading, repetitive injection of pressurised fluids and physico-chemical alteration (i.e. thermal stressing, weathering), heterogeneously compacts and develops damage zones. Consequently, the fluid flow within the edifice becomes localised, contributing to the formation of low and high pore pressure regions that can trigger flank instabilities in the weakest, most permeable rocks (Day, 1996; Reid, 2004).

Importantly for both volcanic and geothermal systems, repetitive fracturing events contribute to the weakening of the rocks, affecting the stability of the system. As previously discussed, increasing the effective pressure (or reducing pore pressure) in a fractured system is not sufficient to recover the permeability of the pre-fracturing event rocks. Alternatively, the same statement can be inferred regarding the strength of the system if no fracture sealing through mineral precipitation or healing through chemical diffusion can occur. This can result in temporal weakening of the rocks (Burdine, 1963; Erarslan and Williams, 2012), enhancing the efficiency of a geothermal field or increasing the risk of flank instability of a volcanic edifice. However, the circulation of saturated hydrothermal fluids through these fractures are can force the system to recover both strength and permeability of the intact rock (Beeler and Hickman, 2004; Olsen et al., 1998; Yasuhara et al., 2004).

In volcanic conduits, concomitant gas exsolution and crystallisation of ascending magmas result in a viscosity increase. The subsequent eruptive style results from the competition between gas exsolution rate and the viscosity of the magma. Effusive eruptions are favoured 1) when the viscosity of the melt is able to accommodate the strain from gas exsolution and 2) allow for rapid bubble coalescence, creating permeable pathways for the gases to escape the system. Explosive eruptions result from magmatic fragmentation in cases where the viscosity of the magma is too high to relax the stress imposed by the volumetric expansion of exsolving gases. Naturally, volcanic eruptions can switch from one style to the other, and as such, the development and effusive emplacement of a relatively degassed, low permeability viscous plug at the top of the magmatic column is commonplace in silicic volcanic systems. The presence of a plug can allow for the build-up of an overpressure near the top of the magmatic column, that eventually must overcome the tensile strength of the plug to trigger failure and permit gas escape (passively or explosively). When the gas can be bled out of the

system the overpressure declines slowly, resulting in the relaxation of stresses accumulated in the magmatic conduit (and plug). In this type of system, repetitive fracture and healing cycles in the plug may create strength and permeability variations. From the relict healing textures in both natural and synthetic samples, I suggest that while the strength recovery is mostly controlled by diffusion of elements across the fracture interface, the shutting of permeable pathways occurs during the wetting regime. Indeed, as permeability depends on the connectivity of pores and fractures in the medium, the isolation of pores/ micro-cracks along a healing interface could occur as early as during viscous relaxation of the fracture interface (wetting regime). Further relaxation of the pores, along with diffusion, then create the characteristic linear trails of unconnected pores often seen in erupted lavas. This implies that in volcanic systems, the overpressure can start building up as soon as the characteristic timescale for fracture healing (defined in Chapter 6) is overcome.

At Santiaguito volcano (Guatemala), regular inflation-deflation cycles conclude with gas-rich, relatively ash-poor eruptions (De Angelis et al., 2016; Johnson et al., 2014), suggesting minimal fragmentation of the magmatic column (De Angelis et al., 2016) that may be sacrificial, contributing to the structural stability of the dome (Lavallée et al., 2015). Here, I suggest that the cyclicity observed at Santiaguito can result from the interaction between cyclic gas supply (Johnson et al., 2014; Michaut et al., 2013) and strength recovery in the plug due to fracture healing. In this scenario, the eruptive mechanics of Santiaguito volcano would initiate (shortly after the termination of an outgassing event or an explosion) with 1) fracture closure, associated with the final fraction of gas escaping the conduit, leading to local volcano deflation (seen in tilt signals; Lavallée et al., 2015); 2) progressive fracture healing would seal the permeable pathway in the plug and permit fault strength recovery, both of which would conspire to trap gas, which would pressurise within the edifice, causing local ground inflation (Fig. 7-1a). 3) Once the gas accumulation overcomes the tensile strength gained by fracture healing, tensile and shear fractures may develop, liberating the accumulated gases, and in some cases ash resulting from fragmentation (Fig. 7-1b), which may trigger seismicity, at the onset of a deflation period, which sees the cycle starting again. The time and event size regularity exhibited at Santiaguito suggests that the healing of fractures is comparable between events, and that the degassing at the top of the magmatic column remains relatively constant, resulting in regularly spaced eruptions liberating the same energy.
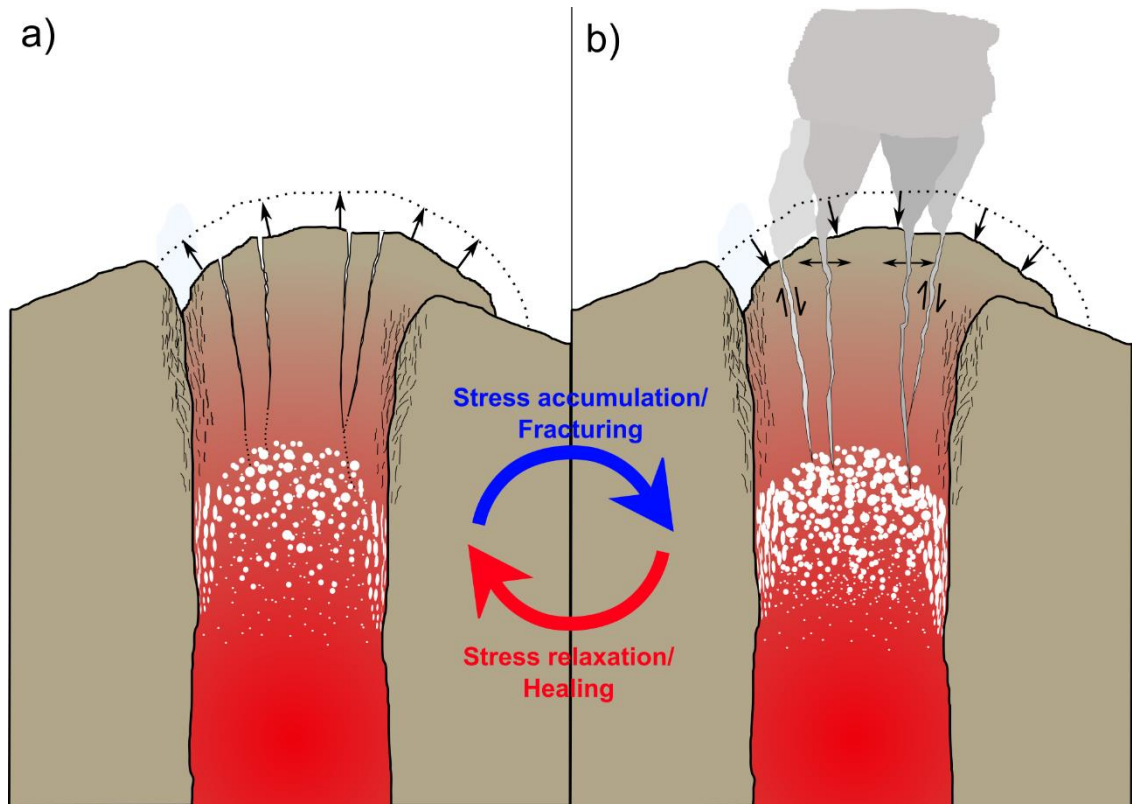
Figure 7-1. a) Stress accumulation due to gas exsolution beneath an impermeable plug generates inflation in the edifice (black arrows) and creates fractures that trigger an explosive eruption. **b)** The stress accumulated is released, the edifice undergoes deflation (black arrows) and fractures heal. The associated permeability reduction and strength recovery allow for new stress build up, and another fracture and healing cycle to start.

7.3. Suggestions for future work

In this thesis, I discuss the importance of better constraining fluid flow in the magmatic, volcanic and geothermal environments. Using novel types of experiments in Chapters 5 and 6, I determined 1) the temperature window of columnar jointing and 2) the mechanics and kinetics of fracture healing in silicate liquids. Being the first of their kind, these studies concentrated on simple materials (e.g., homogeneous glass, presence of one fracture, fracturing in single-phase material) with applicability to simple systems. This has led to the creation of new models, which may be further tested against more complex scenarios and I foresee that these experimental procedures will be used to enhance the applicability of these models to a wider range of geological processes. Hereunder, I suggest a list of potential improvements to this work.

In the columnar jointing study, the temperature window was thermo-mechanically defined and modelled for one particular basalt. Applying the same method to other rocks, with different thermo-mechanical properties would consolidate the columnar jointing model and ensure its general applicability. Additionally, applying this method to a more silicic system (for example a rheomorphic ignimbrite, in which columnar jointing is common) where interstitial melt is present at high temperatures, would help determine cooling conditions that lead to that the formation of columnar joints by crossing the glass transition. Extending the description of joint formation to the spectrum of magmatic compositions and scales would help resolve a long-lasting debate on the development of these spectacular features, and would contribute to the interplay between composition, deposit size, cooling history and column spacing which controls the permeability evolution of a cooling magmatic body.

Here, I examined the permeability of the materials using distilled (non-reactive) water at flow rates controlled to avoid turbulence. While this provides insights on the controls of the porous medium on fluid flow, neither the porous medium, nor the permeating fluid are allowed to change in this experimental setup. Further work with other fluids (e.g. brines) could help understanding the permeability evolution while minerals precipitate and seal the permeable, porous medium. Additionally, work at high temperature, where either the nature of the fluid (e.g. gaseous or liquid) or the compressibility of the porous medium are changed could prove insightful for the true understanding of the permeability development in magmatic, volcanic and geothermal settings.

Furthermore, the fractures here were created in tension to form a simple macro-fracture, and permeability was measured under hydrostatic conditions and as such, the fractures did not experience any shear, nor develop any gouge. Further work on the impact of pores and crystals (size, abundance) on comminution, resulting gouge characteristics (grain size, shapes) and compactional behaviour effects on permeability evolution during shear stress could help characterise fluid flow localisation in shear stress regimes. Additionally, understanding how gouges with different characteristics sinter (i.e. healing in granular media) at high temperatures, and interact with fracture healing in shear regimes would help improve the knowledge of the processes occurring in volcanic conduits.

The experiments designed in Chapter 6 provide the basis to continue exploring the process of fracture healing. By examining a simple, single-phase, dry system with uniform contact to establish a relationship between wetting and diffusion across a spectrum of viscosities, we can now begin to integrate the complexity of natural fracture in multiphase suspensions.

In natural materials, asperities along fracture planes result in more tortuous fluid pathways, and higher fracture roughness would almost certainly affect the relative lengths of the two regimes defined here (wetting and diffusive regimes). For example, higher fracture roughness or the inclusion of fragments (a result of comminution during shear) would require more viscous deformation along the contact interface (wetting regime). This would impact the timescales for fracture closure (and permeability reduction), by viscous flow; at high viscosities, increased roughness or fracture infill could allow fractures to remain open for longer timescales, whereas lower viscosities could accelerate closure of pathways. Understanding of the timescales required for healing and/ or sealing of fractures would also contribute to enhancing the sustainability of geothermal extraction and avoid over exploitation, while also helping to better constrain stress fields in volcanic edifices.

In natural materials the presence of crystals at the fracture interface would also limit the fraction of melt (and hence the surface for melt-melt diffusion), thus slowing down the strength recovery achievable through diffusive exchange. Furthermore, while "crystal to crystal" and "crystal to melt" healing are achieved at much longer timescales (for a given element and temperature) due to slow diffusivity in crystals (Freer, 1981), quantifying the maximum strength recovery of the interface as a function of crystal content could be beneficial for our understanding of stress accumulation and energy release during eruptions.

The work presented here have shown that fundamental mechanisms, known to occur in nature, can be studied with simple experiments that aim to replicate similar conditions. Experiments are crucial for the development our models as they may help provide a quantification of key variables and processes, which may help link geological, chemical and physical observations made in nature. Such experiments will undoubtedly, with time and technological advance, be further developed to constrain yet more complex physico-chemical process and contribute to a better understanding of geological phenomena.

"Ahhh bibliographie! ...Bibliographie…"
Le roi Burgonde, *Kaamelot, Livre I*

Bibliography

Acocella, V., 2015, Great challenges in volcanology: how does the volcano factory work?: Grand Challenges in the Field of Earth Science, p. 11.

Amadei, B., 1996, Importance of anisotropy when estimating and measuring in situ stresses in rock: International Journal of Rock Mechanics and Mining Sciences & Geomechanics Abstracts, v. 33, no. 3, p. 293-325.

Anderson, E. M., 1905, The dynamics of faulting: Transactions of the Edinburgh Geological Society, v. 8, no. 3, p. 387-402.

Anovitz, L. M., and Cole, D. R., 2015, Characterization and Analysis of Porosity and Pore Structures Reviews in Mineralogy and Geochemistry, v. 80, p. 104.

Armitage, P. J., Faulkner, D. R., Worden, R. H., Aplin, A. C., Butcher, A. R., and Iliffe, J., 2011, Experimental measurement of, and controls on, permeability and permeability anisotropy of caprocks from the CO2storage project at the Krechba Field, Algeria: Journal of Geophysical Research, v. 116, no. B12.

Asaro, R. J., 1983, Crystal plasticity: J. appl. Mech, v. 50, no. 4b, p. 921-934.

Ashby, M., and Sammis, C., 1990, The damage mechanics of brittle solids in compression: Pure and Applied Geophysics, v. 133, no. 3, p. 489-521.

Ashby, M. F., and Hallam, S., 1986, The failure of brittle solids containing small cracks under compressive stress states: Acta Metallurgica, v. 34, no. 3, p. 497-510.

Ashwell, P. A., Kendrick, J. E., Lavallée, Y., Kennedy, B. M., Hess, K. U., von Aulock, F. W., Wadsworth, F. B., Vasseur, J., and Dingwell, D. B., 2015, Permeability of compacting porous lavas: Journal of Geophysical Research: Solid Earth, v. 120, no. 3.

ASTM, 2008, Standard test method for splitting tensile strength of intact rock core specimens.

Aydin, A., 2000, Fractures, faults, and hydrocarbon entrapment, migration and flow: Marine and Petroleum Geology, v. 17, p. 797-814.

Bakker, R. R., Violay, M. E., Benson, P. M., and Vinciguerra, S. C., 2015, Ductile flow in sub-volcanic carbonate basement as the main control for edifice stability: New experimental insights: Earth and Planetary Science Letters, v. 430, p. 533-541.

Barton, N., Bandis, S., and Bakhtar, K., 1985, Strength, deformation and conductivity coupling rock joints: International Journal of Rock Mechanics and Mining Sciences, v. 22, no. 3, p. 121-140.

Batzle, M. L., and Simmons, G., 1977, Geothermal systems: Rocks, fluids, fractures: The Earth's Crust, p. 233-242.

Beeler, N. M., and Hickman, H. H., 2004, Stress-induced, time-dependent fracture closure at hydrothermal conditions: Journal of Geophysical Research, v. 109.

Benderitter, Y., and Elsass, P., 1995, Structural control of deep fluid circulation at the Soultz HDR site, France: a review: Geothermal Science and Technology, v. 4, no. 4, p. 227-237.

Benson, P., Schubnel, A., Vinciguerra, S., Trovato, C., Meredith, P., and Young, R. P., 2006a, Modeling the permeability evolution of microcracked rocks from elastic wave velocity inversion at elevated isostatic pressure: Journal of Geophysical Research-Solid Earth, v. 111, no. B4.

Benson, P. M., Meredith, P. G., Platzman, E. S., and White, R. E., 2005, Pore fabric shape anisotropy in porous sandstones and its relation to elastic wave velocity and permeability anisotropy under hydrostatic pressure: International Journal of Rock Mechanics and Mining Sciences, v. 42, no. 7-8, p. 890-899.

Benson, P. M., Meredith, P. G., and Schubnel, A., 2006b, Role of void space geometry in permeability evolution in crustal rocks at elevated pressure: Journal of Geophysical Research: Solid Earth, v. 111, no. B12, p. B12203.

Benson, P. M., Thompson, B. D., Meredith, P. G., Vinciguerra, S., and Young, R. P., 2007, Imaging slow failure in triaxially deformed Etna basalt using 3D acoustic-emission location and X-ray computed tomography: Geophysical Research Letters, v. 34, no. 3, p. L03303.

Berlo, K., Tuffen, H., Smith, V. C., Castro, J. M., Pyle, D. M., Mather, T. A., and Geraki, K., 2013, Element variations in rhyolitic magma resulting from gas transport: Geochimica et Cosmochimica Acta, v. 121, no. 0, p. 436-451.

Bernabe, Y., The effective pressure law for permeability in Chelmsford granite and Barre granite, *in* Proceedings International Journal of Rock Mechanics and Mining Sciences & Geomechanics Abstracts1986, Volume 23, Elsevier, p. 267-275.

Bernabé, Y., Li, M., and Maineult, A., 2010, Permeability and pore connectivity: A new model based on network simulations: Journal of Geophysical Research, v. 115.

Bjørlykke, K., 1993, Fluid flow in sedimentary basins: Sedimentary Geology, v. 86, no. 1-2, p. 137-158.

Blower, J. D., 2001, Factors controlling permeability-porosity relationships in magma: Bulletin of Volcanology, v. 63, no. 7, p. 497-504.

Blundy, J., and Cashman, K., 2001, Ascent-driven crystallisation of dacite magmas at Mount St Helens, 1980-1986: Contributions to Mineralogy and Petrology, v. 140, p. 631-650.

Bobet, A., and Einstein, H., 1998, Fracture coalescence in rock-type materials under uniaxial and biaxial compression: International Journal of Rock Mechanics and Mining Sciences, v. 35, no. 7, p. 863-888.

Bonaccorso, A., Currenti, G., and Del Negro, C., 2013, Interaction of volcano-tectonic fault with magma storage, intrusion and flank instability: A thirty years study at Mt. Etna volcano: Journal of Volcanology and Geothermal Research, v. 251, p. 127-136.

Bourbie, T., and Walls, J., 1982, Pulse decay permeability: Analytical solution and experimental test: Society of Petroleum Engineers Journal, v. 22, no. 05, p. 719-721.

Bourbie, T., and Zinszner, B., 1985, Hydraulic and Acoustic properties as a function of porosity in Fontainebleau Sandstone: Journal of Geophysical Research, v. 90, no. B13, p. 11.

Brace, W. F., Walsh, J. B., and Frangos, W. T., 1968, Permeability of granite under high pressure: Journal of Geophysical Research, v. 73, no. 6, p. 2225-2236.

Brown, R., Kavanagh, J., Sparks, R., Tait, M., and Field, M., 2007, Mechanically disrupted and chemically weakened zones in segmented dike systems cause vent localization: Evidence from kimberlite volcanic systems: Geology, v. 35, no. 9, p. 815-818.

Brown, S. K., Auker, M., and Sparks, R., 2015, Populations around Holocene volcanoes and development of a Population Exposure Index: Global Volcanic Hazards and Risk. Cambridge University Press, Cambridge, p. 223-232.

Brown, S. R., and Bruhn, R. L., 1998, Fluid permeability of deformable fracture networks: Journal of Geophysical Research: Solid Earth, v. 103, no. B2, p. 2489-2500.

Browning, J., Meredith, P., and Gudmundsson, A., 2016, Cooling-dominated cracking in thermally stressed volcanic rocks: Geophysical Research Letters, v. 43, no. 16, p. 8417-8425.

Bubeck, A., Walker, R., Healy, D., Dobbs, M., and Holwell, D., 2017, Pore geometry as a control on rock strength: Earth and Planetary Science Letters, v. 457, p. 38-48.

Budkewitsch, P., and Robin, P. Y., 1994, Modeling the evolution of columnar joints: Journal of Volcanology and Geothermal Research, v. 59, no. 3, p. 219-239.

Burdine, N., 1953, Relative permeability calculations from pore size distribution data: Journal of Petroleum Technology, v. 5, no. 03, p. 71-78.

Burdine, N., 1963, Rock failure under dynamic loading conditions: Society of Petroleum Engineers Journal, v. 3, no. 01, p. 1-8.

Cabrera, A., Weinberg, R. F., Wright, H. M. N., Zlotnik, S., and Cas, R. A. F., 2011, Melt fracturing and healing: A mechanism for degassing and origin of silicic obsidian: Geology, v. 39, no. 1, p. 67-70.

Caine, J. S., Evans, J. P., and Forster, C. B., 1996, Fault zone architecture and permeability structure: Geology, v. 24, no. 11, p. 1025-1028.

Calò, M., Dorbath, C., and Lubrano Lavadera, P., 2016, Can faults become barriers for deep fluid circulation? Insights from high-resolution seismic VSP tomography at the Soultz-sous-Forêts geothermal site: Geophysical Research Letters, v. 43, no. 17, p. 8986-8993.

Capuano Jr, L., Huh, M., Swanson, R., Raymond, D. W., Finger, J. T., Mansure, A. J., Polsky, Y., and Knudsen, S. D., 2008, Enhanced Geothermal Systems (EGS) well construction technology evaluation report: Sandia National Laboratories.

Carman, P. C., 1937, Fluid flow through granular beds: Trans IChemE, v. 15, p. 17.

Carman, P. C., 1956, Flow of gases through porous media, London, Butterworths Scientific.

Carrigan, C. R., 1986, A 2-phase hydrothermal cooling model for shallow intrusions: Journal of Volcanology and Geothermal Research, v. 28, no. 1-2, p. 175-192.

Cas, R., and Wright, J. V., 2012, Volcanic successions modern and ancient: A geological approach to processes, products and successions, Springer Science & Business Media.

Cashman, K., and Blundy, J., 2000, Degassing and Crystallization of ascending andesite and dacite: Philosophical transactions of the Royal Society of London, v. 358 p. 1487-1513.

Castro, J. M., Bindeman, I. N., Tuffen, H., and Ian Schipper, C., 2014, Explosive origin of silicic lava: Textural and – $H2O$ evidence for pyroclastic degassing during rhyolite effusion: Earth and Planetary Science Letters, v. 405, no. 0, p. 52-61.

Castro, J. M., Cordonnier, B., Tuffen, H., Tobin, M. J., Puskar, L., Martin, M. C., and Bechtel, H. A., 2012, The role of melt-fracture degassing in defusing explosive rhyolite eruptions at volcán Chaitén: Earth and Planetary Science Letters, v. 333–334, no. 0, p. 63-69.

Caulk, R. A., Ghazanfari, E., Perdrial, J. N., and Perdrial, N., 2016, Experimental investigation of fracture aperture and permeability change within Enhanced Geothermal Systems: Geothermics, v. 62, p. 12-21.

Chen, M., Bai, M., and Roegiers, J.-C., 1999, Permeability tensors of anisotropic fracture networks: Mathematical Geology, v. 31, no. 4.

Clavaud, J.-B., Maineult, A., Zamora, M., Rasolofosaon, P., and Schlitter, C., 2008, Permeability anisotropy and its relations with porous medium structure: Journal of Geophysical Research, v. 113, no. B1.

Collinson, A. S. D., and Neuberg, J. W., 2012, Gas storage, transport and pressure changes in an evolving permeable volcanic edifice: Journal of Volcanology and Geothermal Research, v. 243–244, no. 0, p. 1-13.

Colombier, M., Wadsworth, F. B., Gurioli, L., Scheu, B., Kueppers, U., Di Muro, A., and Dingwell, D. B., 2017, The evolution of pore connectivity in volcanic rocks: Earth and Planetary Science Letters, v. 462, p. 99-109.

Costa, A., 2005, Viscosity of high crystal content melts: Dependence on solid fraction: Geophysical Research Letters, v. 32, no. 22, p. n/a-n/a.

Costa, A., 2006, Permeability-porosity relationship: A reexamination of the Kozeny-Carman equation based on a fractal pore-space geometry assumption: Geophysical Research Letters, v. 33, no. 2.

Costa, A., and Macedonio, G., 2003, Viscous heating in fluids with temperature-dependent viscosity: Implications for magma flows: Non linear processes in geophysics, v. 241, no. 3, p. 234-247.

Curewitz, D., and Karson, J. A., 1997, Structural settings of hydrothermal outflow: Fracture permeability maintained by fault propagation and interaction: Journal of Volcanology and Geothermal Research, v. 79, no. 3, p. 149-168.

Darcy, H., 1856, Les fontaines publiques de la ville de Dijon, Paris, Dalmont.

Darcy, H., 1857, Recherches expérimentales relatives au mouvement de l'eau dans les tuyaux, École impériale polytechnique de Paris, Mallet-Bachelier.

Dasgupta, R., Shashwati, R., and Tarafdar, S., 2000, Correlation between porosity, conductivity and permeability of sedimentary rocks - a ballistic deposition model: Physica A, v. 275, p. 10.

Day, S., 1996, Hydrothermal pore fluid pressure and the stability of porous, permeable volcanoes: Geological Society, London, Special Publications, v. 110, no. 1, p. 77-93.

De Angelis, S., Lamb, O., Lamur, A., Hornby, A., Aulock, F., Chigna, G., Lavallée, Y., and Rietbrock, A., 2016, Characterization of moderate ash-and-gas explosions at Santiaguito volcano, Guatemala, from infrasound waveform inversion and thermal infrared measurements: Geophysical Research Letters, v. 43, no. 12, p. 6220-6227.

Degraff, J. M., and Aydin, A., 1993, Effect of thermal regime on growth increment and spacing of contraction joints in basaltic lava: Journal of Geophysical Research-Solid Earth, v. 98, no. B4, p. 6411-6430.

Deubelbeiss, Y., Kaus, B. J., Connolly, J. A., and Caricchi, L., 2011, Potential causes for the non-Newtonian rheology of crystal-bearing magmas: Geochemistry, Geophysics, Geosystems, v. 12, no. 5.

Dingwell, D. B., and Webb, S. L., 1989, Structural relaxation in silicate melts and Non-Newtonian melt rheology in geologic processes: Physics and Chemistry of Minerals, v. 16, p. 508-516.

Dingwell, D. B., 1996, Volcanic dilemma: Flow or blow?: Science, v. 273, no. 5278, p. 1054-1055.

Dingwell, D. B., 2006, Transport properties of magmas: diffusion and rheology: Elements, v. 2, no. 5, p. 281-286.

Dobson, P. F., Kneafsey, T. J., Hulen, J., and Simmons, A., 2003a, Porosity, permeability, and fluid flow in the Yellowstone geothermal system, Wyoming: Journal of Volcanology and Geothermal Research, v. 123, no. 3-4, p. 313-324.

Dobson, P. F., Kneafsey, T. J., Sonnenthal, E. L., Spycher, N., and Apps, J. A., 2003b, Experimental and numerical simulation of dissolution and precipitation: implications for fracture sealing at Yucca Mountain, Nevada: Journal of Contaminant Hydrology, v. 62, p. 459-476.

Dragoni, M., and Magnanensi, C., 1989, Displacement and stress produced by a pressurized, spherical magma chamber, surrounded by a viscoelastic shell: Physics of the Earth and Planetary Interiors, v. 56, no. 3-4, p. 316-328.

Edmonds, M., Oppenheimer, C., Pyle, D. M., Herd, R. A., and Thompson, G., 2003, SO2 emissions from Soufrière Hills Volcano and their relationship to conduit permeability, hydrothermal interaction and degassing regime: Journal of Volcanology and Geothermal Research, v. 124, no. 1-2, p. 23-43.

Eggertsson, G. H., Lavallée, Y., Kendrick, J. E., and Markússon, S. H., 2017, Enhancing permeability by multiple fractures in the Krafla geothermal reservoir, Iceland, European Geothermal Congress: Strasbourg, France.

Eichelberger, J., Carrigan, C., Westrich, H., and Price, R., 1986, Non-explosive silicic volcanism: Nature, v. 323, no. 6089, p. 598-602.

Elsworth, D., Voight, B., Thompson, G., and Young, S., 2004, Thermal-hydrologic mechanism for rainfall-triggered collapse of lava domes: Geology, v. 32, no. 11, p. 969-972.

Erarslan, N., and Williams, D., 2012, Investigating the effect of cyclic loading on the indirect tensile strength of rocks: Rock mechanics and rock engineering, v. 45, no. 3, p. 327-340.

Fairley, J. P., 2009, Modeling fluid flow in a heterogeneous, fault-controlled hydrothermal system: Geofluids, v. 9, no. 2, p. 153-166.

Faoro, I., Niemeijer, A., Marone, C., and Elsworth, D., 2009, Influence of shear and deviatoric stress on the evolution of permeability in fractured rock: Journal of Geophysical Research: Solid Earth, v. 114, no. B1.

Farmer, C. L., 2002, Upscaling: a review: International Journal for Numerical Methods in Fluids, v. 40, p. 15.

Farquharson, J., Heap, M. J., Baud, P., Reuschlé, T., and Varley, N. R., 2016, Pore pressure embrittlement in a volcanic edifice: Bulletin of Volcanology, v. 78, no. 1, p. 6.

Farquharson, J., Heap, M. J., Varley, N. R., Baud, P., and Reuschlé, T., 2015, Permeability and porosity relationships of edifice-forming andesites: A combined field and laboratory study: Journal of Volcanology and Geothermal Research, v. 297, p. 52-68.

Farrell, N. J. C., Healy, D., and Taylor, C. W., 2014, Anisotropy of permeability in faulted porous sandstones: Journal of Structural Geology, v. 63, p. 18.

Faulkner, D. R., 2004, A model for the variation in permeability of clay-bearing fault gouge with depth in the brittle crust: Geophysical research letters, v. 31, no. 19.

Faulkner, D. R., Mitchell, T., Healy, D., and Heap, M., 2006, Slip on'weak'faults by the rotation of regional stress in the fracture damage zone: Nature, v. 444, no. 7121, p. 922.

Faulkner, D. R., and Rutter, E. H., 2003, The effect of temperature, the nature of the pore fluid, and subyield differential stress on the permeability of phyllosilicate-rich fault gouge: Journal of Geophysical Research-Solid Earth, v. 108, no. B5.

Filomena, C. M., Hornung, J., and Stollhofen, H., 2014, Assessing accuracy of gas-driven permeability measurements: A comparative study of diverse Hassler-cell and probe permeameter devices: Solid Earth, v. 5, no. 1, p. 1-11.

Forbes, A. E. S., Blake, S., and Tuffen, H., 2014, Entablature: fracture types and mechanisms: Bulletin of Volcanology, v. 76, no. 5.

Fortin, J., Stanchits, S., Vinciguerra, S., and Gueguen, Y., 2011, Influence of thermal and mechanical cracks on permeability and elastic wave velocities in a basalt from Mt. Etna volcano subjected to elevated pressure: Tectonophysics, v. 503, p. 15.

Fredrich, J., and Evans, B., Strength recovery along simulated faults by solution transfer processes, *in* Proceedings The 33th US Symposium on Rock Mechanics (USRMS)1992, American Rock Mechanics Association.

Freer, R., 1981, Diffusion in silicate minerals and glasses: a data digest and guide to the literature: Contributions to Mineralogy and Petrology, v. 76, no. 4, p. 440-454.

Fuenkajorn, K., and Phueakphum, D., 2011, Loaboratory assesment of healing of fractures in rock salt: Bulletin of Engineering Geology and the Environment, v. 70, p. 8.

Gaetani, G. A., Ghiorso, M. S., Sack, R. O., Hirschmann, M., and Asimow, P. D., 1998, MELTS: Science, v. 282, no. 5395, p. 1834-1835.

Gardner, J. E., Llewellin, E. W., Watkins, J. M., and Befus, K. S., 2017, Formation of obsidian pyroclasts by sintering of ash particles in the volcanic conduit: Earth and Planetary Science Letters, v. 459, p. 252-263.

Gaunt, H. E., Sammonds, P. R., Meredith, P. G., Smith, R., and Pallister, J. S., 2014, Pathways for degassing during the lava dome eruption of Mount St. Helens 2004–2008: Geology, v. 42, no. 11, p. 947-950.

Gavrilenko, P., and Gueguen, Y., 1998, Flow in fractured media: A modified renormalization method: Water resources journal, v. 34, no. 2.

Gent, A. N., 1960, Theory of the parallel plate viscometer: British Journal of Applied Physics, v. 11, no. 2, p. 85.

Glover, P., Baud, P., Darot, M., Meredith, P., Boon, S., LeRavalec, M., Zoussi, S., and Reuschle, T., 1995, α/β phase transition in quartz monitored using acoustic emissions: Geophysical Journal International, v. 120, no. 3, p. 775-782.

Goehring, L., and Morris, S. W., 2005, Order and disorder in columnar joints: Europhysics Letters, v. 69, no. 5, p. 739-745.

Goehring, L., and Morris, S. W., 2008, Scaling of columnar joints in basalt: Journal of Geophysical Research, v. 113, p. 18.

Gonnermann, H. M., and Manga, M., 2003, Explosive volcanism may not be an inevitable consequence of magma fragmentation: Nature, v. 426, p. 432-435.

Gonnermann, H. M., and Manga, M., 2007, The fluid mechanics inside a volcano: Annual Review of Fluid Mechanics, v. 39, p. 321-356.

Goto, A., 1999, A new model for volcanic earthquake at Unzen Volcano: Melt rupture model: Geophysical Research Letters, v. 26, no. 16, p. 2541-2544.

Gottsmann, J., Harris, A. J. L., and Dingwell, D. B., 2004, Thermal history of Hawaiian pahoehoe lava crusts at the cylass transition: implications for flow rheology and emplacement: Earth and Planetary Science Letters, v. 228, no. 3-4, p. 343-353.

Griffith, A. A., 1920, The phenomena of Rupture and Flow in Solids: Philosophical Transactions of the Royal Society of London, v. 221, p. 36.

Griffiths, L., Heap, M. J., Xu, T., Chen, C.-f., and Baud, P., 2017, The influence of pore geometry and orientation on the strength and stiffness of porous rock: Journal of Structural Geology, v. 96, p. 149-160.

Grossenbacher, K. A., and McDuffie, S. M., 1995, Conductive cooling of lava: Columnar joint diameter and stria width as functions of cooling rate and thermal gradient: Journal of Volcanology and Geothermal Research, v. 69, p. 9.

Grover, D., Savidge, C. R., Townsend, L.,Rosario, O., Hub, L-B., Rizzo, D. M., and Dewoolkar, M. M., 2016, Surface permeability of natural and engineered porous building materials: Construction and Building Materials, v. 112, p. 1088-1100.

Gudmundsson, A., 2006, How local stresses control magma-chamber ruptures, dyke injections, and eruptions in composite volcanoes: Earth Science Reviews.

Gudmundsson, A., and Brenner, L. S., 2009, Local stresses, dyke arrest and surface deformation in volcanic edificesand rift zones, 2009, v. 4.

Gudmundsson, A., and Loetveit, I. F., 2005, Dyke emplacement in a layered and faulted rift zone: Journal of Volcanology and Geothermal Research, v. 144, no. 1, p. 311-327.

Gueguen, Y., and Dienes, J., 1989, Transport properties of rocks frome statistics and percolation: Mathematical Geology, v. 21, no. 1.

Gupta, T. K., 1976, Crack healing and strengthening of thermally shocked alumina: Journal of the American Ceramic Society, v. 59, no. 5-6, p. 4.

Hansen, J., and Skjeltorp, A., 1988, Fractal pore space and rock permeability implications: Physical review B, v. 38, no. 4, p. 2635.

Healy, D., Jones, R. R., and Holdsworth, R. E., 2006, Three-dimensional brittle shear fracturing by tensile crack interaction: Nature, v. 439, no. 7072, p. 64.

Heap, M., Mollo, S., Vinciguerra, S., Lavallée, Y., Hess, K.-U., Dingwell, D. B., Baud, P., and Iezzi, G., 2013, Thermal weakening of the carbonate basement under Mt. Etna volcano (Italy): implications for volcano instability: Journal of volcanology and geothermal research, v. 250, p. 42-60.

Heap, M. J., Farquharson, J. I., Baud, P., Lavallee, Y., and Reuschle, T., 2015a, Fracture and compaction of andesite in a volcanic edifice: Bull Volcanol, v. 77, no. 6, p. 55.

Heap, M. J., Farquharson, J. I., Wadsworth, F. B., Kolzenburg, S., and Russell, J. K., 2015b, Timsecales for permeability reduction and strength recovery in densifying magma: Earth and Planetary Science Letters, v. 429, p. 11.

Heap, M. J., and Kennedy, B. M., 2016, Exploring the scale-dependent permeability of fractured andesite: Earth and Planetary Science Letters, v. 447, p. 11.

Heap, M. J., Kolzenburg, S., Russell, J. K., Campbell, M. E., Welles, J., Farquharson, J. I., and Ryan, A., 2014a, Conditions and timescales for welding block-and-ash flow deposits: Journal of Volcanology and Geothermal Research, v. 289, p. 8.

Heap, M. J., Lavallée, Y., Petrakova, L., Baud, P., Reuschlé, T., Varley, N. R., and Dingwell, D. B., 2014b, Microstructural controls on the physical and mechanical properties of edifice-forming andesites at Volcán de Colima, Mexico: Journal of Geophysical Research: Solid Earth, p. 2013JB010521.

Heap, M. J., Russell, J. K., and Kennedy, L. A., 2016, Mechanical behaviour of dacite from Mount St. Helens (USA): A link between porosity and lava dome extrusionmechanism (dome or spine)?: Journal of Volcanology and Geothermal Research.

Hess, K.-U., Cordonnier, B., Lavallée, Y., and Dingwell, D. B., 2008, Viscous heating in rhyolite: An in situ experimental determination: Earth and Planetary Science Letters, v. 275, no. 1–2, p. 121-126.

Hess, K. U., and Dingwell, D. B., 1996, Viscosities of hydrous leucogranitic melts: A non-Arrhenian model: American Mineralogist, v. 81, no. 9-10, p. 1297-1300.

High Pressure Technology Association, 1975, High pressure safety code, The Association.

Huppert, H. E., and Sparks, R. S. J., 1989, Chilled margins in igneous rocks: Earth and Planetary Science Letters, v. 92, no. 3-4, p. 397-405.

Isida, M., and Nemat-Nasser, S., 1987, On mechanics of crack growth and its effects on the overall response of brittle porous solids: Acta metallurgica, v. 35, no. 12, p. 2887-2898.

ISRM, 1978, Suggested Methods for determing tensile strength of rock materials: Int. J. Rock Mech. Min. Sci. Geochem. Abstract, v. 15, no. 3, p. 4.

Jaeger, J. C., Cook, N. G., and Zimmerman, R., 2009, Fundamentals of rock mechanics, John Wiley & Sons.

Johnson, J. B., Lyons, J., Andrews, B., and Lees, J., 2014, Explosive dome eruptions modulated by periodic gas-driven inflation: Geophysical Research Letters, v. 41, no. 19, p. 6689-6697.

Jud, K., Kausch, H. H., and Williams, J. G., 1981, Fracture mechanics studies of crack healing and welding of polymers: Journal of Material Science, p. 7.

Kantha, L. H., 1981, Basalt fingers - Origin of columnar joints: Geological Magazine, v. 118, no. 3, p. 251-&.

Kasting, J. F., 1993, Earth's early atmosphere: Science, p. 920-926.

Kavanagh, J. L., Menand, T., and Sparks, R. S. J., 2006, An experimental investigation of sill formation and propagation in layered elastic media: Earth and Planetary Science Letters, v. 245, no. 3, p. 799-813.

Kavanagh, J. L., and Pavier, M. J., 2014, Rock interface strength influences fluid-filled fracture propagation pathways in the crust: Journal of Structural Geology, v. 63, p. 68-75.

Kendrick, J., Lavallée, Y., Hirose, T., Di Toro, G., Hornby, A., De Angelis, S., and Dingwell, D., 2014a, Volcanic drumbeat seismicity caused by stick-slip motion and magmatic frictional melting: Nature Geoscience, v. 7, no. 6, p. 438-442.

Kendrick, J. E., Lavallée, Y., Hess, K. U., De Angelis, S., Ferk, A., Gaunt, H. E., Meredith, P. G., Dingwell, D. B., and Leonhardt, R., 2014b, Seismogenic frictional melting in the magmatic column: Solid Earth, v. 5, no. 1, p. 199-208.

Kendrick, J. E., Lavallée, Y., Hess, K. U., Heap, M. J., Gaunt, H. E., Meredith, P. G., and Dingwell, D. B., 2013, Tracking the permeable porous network during strain-dependent magmatic flow: Journal of Volcanology and Geothermal Research, v. 260, no. 0, p. 117-126.

Kendrick, J. E., Lavallée, Y., Mariani, E., Dingwell, D. B., Wheeler, J., and Varley, N. R., Accepted, Crystal plasticity as an indicator of the viscous-brittle transition in magmas: Nature communications.

Kendrick, J. E., Lavallee, Y., Varley, N. R., Wadsworth, F. B., Lamb, O. D., and Vasseur, J., 2016, Blowing Off Steam: Tuffisite Formation As a Regulator forr Lava Dome Eruptions: Frontiers in Earth Science, v. 4.

King, J., Williams-Jones, A. E., van Hinsberg, V., and Williams-Jones, G., 2014, High-Sulfidation Epithermal Pyrite-Hosted Au (Ag-Cu) Ore Formation by Condensed Magmatic Vapors on Sangihe Island, Indonesia: Economic Geology, v. 109, no. 6, p. 1705-1733.

Klinkenberg, L., The permeability of porous media to liquids and gases, *in* Proceedings Drilling and production practice1941, American Petroleum Institute.

Klug, C., and Cashman, C., 1996, Permeability development in vesiculating magmas: Implications for fragmentation: Bulletin of Volcanology, v. 58, p. 87-100.

Knapp, R. B., and Knight, J. E., 1977, Differential thermal expansion of pore fluids: Fracture propagation and microearthquake production in hot pluton environments: Journal of Geophysical Research, v. 82, no. 17, p. 2515-2522.

Kozeny, J., 1927, Uber kapillare Leitung der wasser in boden: Sitzungsber. Akad. Wiss. Wien, v. 136, p. 36.

Kushnir, A. R. I., Martel, C., Bourdier, J.-l., Heap, M. J., Reuschlé, T., Erdmann, S., Komorowski, J. C., and Cholik, N., 2016, Probing permeability and microstructure: Unravelling the role of a low-permeability dome on the explosivity of Merapi (Indonesia): Journal of Volcanology and Geothermal Research, v. 316, p. 16.

Laboulais-Lesage, I., 2004, Seeing, combining and describing: physical geography according to Nicolas Demarest: Revue D Histoire Moderne Et Contemporaine, v. 51, no. 2, p. 38-57.

Lamur, A., Kendrick, J., Eggertsson, G., Wall, R., Ashworth, J., and Lavallée, Y., 2017, The permeability of fractured rocks in pressurised volcanic and geothermal systems: Scientific Reports, v. 7.

Laumonier, M., Arbaret, L., Burgisser, A., and Champallier, R., 2011, Porosity redistribution enhanced by strain localization in crystal-rich magmas: Geology, v. 39, no. 8, p. 4.

Lavallée, Y., Benson, P. M., Heap, M. J., Flaws, A., Hess, K. U., and Dingwell, D. B., 2012a, Volcanic conduit failure as a trigger to magma fragmentation: Bulletin of Volcanology, v. 74, no. 1, p. 11-13.

Lavallée, Y., Benson, P. M., Heap, M. J., Hess, K. U., Flaws, A., Schillinger, B., Meredith, P. G., and Dingwell, D. B., 2013, Reconstructing magma failure and the degassing network of dome-building eruptions: Geology, v. 41, no. 4, p. 515-518.

Lavallée, Y., Meredith, P., Dingwell, D., Hess, K., Wassermann, J., Cordonnier, B., Gerik, A., and Kruhl, J., 2008, Seismogenic lavas and explosive eruption forecasting: Nature, v. 453, no. 7194, p. 507.

Lavallée, Y., Varley, N., Alatorre-Ibargüengoitia, M., Hess, K. U., Kueppers, U., Mueller, S., Richard, D., Scheu, B., Spieler, O., and Dingwell, D., 2012b, Magmatic architecture of dome-building eruptions at Volcán de Colima, Mexico: Bulletin of Volcanology, v. 74, no. 1, p. 249-260.

Lee, S. H., Lough, M. F., and Jensen, C. L., 2001, Hierarchical modeling of flow in naturally fractured formations with multiple length scales: Water resources journal, v. 37, p. 13.

Li, D., and Wong, L. N. Y., 2013, The Brazilian disc test for rock mechanics applications: Review and new insights: Rock mechanics and rock engineering, v. 46, no. 2, p. 269-287.

Lister, C. R. B., 1977, Qualitative models of spreading-center processes, including hydrothermal penetration: Tectonophysics, v. 37, no. 1-3, p. 203-218.

Lister, J. R., and Kerr, R. C., 1991, Fluid-mechanical models of crack propagation and their application to magma transport in dykes: Journal of Geophysical Research: Solid Earth, v. 96, no. B6, p. 10049-10077.

Loaiza, S., Fortin, J., Schubnel, A., Gueguen, Y., Vinciguerra, S., and Moreira, M., 2012, Mechanical behavior and localized failure modes in a porous basalt from the Azores: Geophys. Res. Lett., v. 39.

López, D. L., and Williams, S. N., 1993, Catastrophic volcanic collapse: relation to hydrothermal processes: Science, v. 260, no. 5115, p. 1794-1796.

Lore, J., Gao, H., and Aydin, A., 2000a, Viscoelastic thermal stress in cooling basalt flows: Journal of Geophysical Research, v. 105, no. B10, p. 23695-23709.

Lore, J., Gao, H., and Aydin, A., 2000b, Viscoelastic thermal stress in cooling basalt flows: Journal of Geophysical Research, v. 105, no. B10, p. 15.

Lucia, F. J., 1983, Petrophysical parameters estimated from visual descriptions of carbonate rocks: A field classification of carbonate pore space: Journal of petroleum technology, p. 629-637.

Maccaferri, F., Bonafede, M., and Rivalta, E., 2011, A quantitative study of the mechanisms governing dike propagation, dike arrest and sill formation: Journal of Volcanology and Geothermal Research, v. 208, no. 1, p. 39-50.

Mader, H., Llewellin, E., and Mueller, S., 2013, The rheology of two-phase magmas: A review and analysis: Journal of Volcanology and Geothermal Research, v. 257, p. 135-158.

Magee, C., Jackson, C. A.-L., and Schofield, N., 2013, The influence of normal fault geometry on igneous sill emplacement and morphology: Geology, v. 41, no. 4, p. 407-410.

Mahabadi, O. K., Cottrell, B. E., and Grasselli, G., 2010, An Example of Realistic Modelling of Rock Dynamics Problems: FEM/DEM Simulation of Dynamic Brazilian Test on Barre Granite: Rock Mechanics and Rock Engineering, v. 43, no. 6, p. 707-716.

Majer, E. L., Baria, R., Stark, M., Oates, S., Bommer, J., Smith, B., and Asanuma, H., 2007, Induced seismicity associated with enhanced geothermal systems: Geothermics, v. 36, no. 3, p. 185-222.

Marsh, B. D., 1989, Magma chambers: Annual Review of Earth and Planetary Sciences, v. 17, no. 1, p. 439-472.

Martin, W., Baross, J., Kelley, D., and Russell, M. J., 2008, Hydrothermal vents and the origin of life: Nature reviews. Microbiology, v. 6, no. 11, p. 805.

Mastin, L. G., 2005, The controlling effect of viscous dissipation on magma flow in silicic conduits: Journal of Volcanology and Geothermal Research, v. 143, no. 1, p. 17-28.

Matthäi, S. K., and Belayneh, M., 2004, Fluid flow partitioning between fractures and a permeable rock matrix: Geophysical Research Letters, v. 31, no. 7.

Mattsson, H. B., Caricchi, L., Almqvist, B. S. G., Caddick, M. J., Bosshard, S. A., Hetenyi, G., and Hirt, A. M., 2011, Melt migration in basalt columns driven by crystallization-induced pressure gradients: Nature Communications, v. 2.

Melnik, O., and Sparks, R., 1999, Nonlinear dynamics of lava dome extrusion: Nature, v. 402, no. 6757, p. 37.

Menéndez, B., David, C., and Darot, M., 1999, A study of the crack network in thermally and mechanically cracked granite samples using confocal scanning laser microscopy: Physics and Chemistry of the Earth, Part A: Solid Earth and Geodesy, v. 24, no. 7, p. 627-632.

Meredith, P. G., and Atkinson, B. K., 1983, High-temperature tensile crack propagation in quartz: experimental results and application to time-dependent earthquake rupture: Earthquake Prediction Research, v. 1, no. 4, p. 377-391.

Meredith, P. G., Knight, K. S., Boon, S. A., and Wood, I. G., 2001, The microscopic origin of thermal cracking in rocks: An investigation by simultaneous time-of-flight neutron diffraction and acoustic emission monitoring: Geophysical research letters, v. 28, no. 10, p. 2105-2108.

Michalske, T. A., and Fuller, E. R. J., 1985, Closure and repropagation of healed cracks in silicate glass: Journal of American Ceramic Society, v. 68, no. 11.

Michaut, C., Ricard, Y., Bercovici, D., and Sparks, R. S. J., 2013, Eruption cyclicity at silicic volcanoes potentially caused by magmatic gas waves: Nature Geosci, v. 6, no. 10, p. 856-860.

Milazzo, M. P., Keszthelyi, L. P., Jaeger, W. L., Rosiek, M., Mattson, S., Verba, C., Beyer, R. A., Geissler, P. E., McEwen, A. S., and Hi, R. T., 2009, Discovery of columnar jointing on Mars: Geology, v. 37, no. 2, p. 171-174.

Mollo, S., Heap, M. J., Iezzi, G., Hess, K. U., Scarlato, P., and Dingwell, D. B., 2012, Volcanic edifice weakening via decarbonation: A self-limiting process?: Geophysical Research Letters, v. 39, no. 15.

Morrow, C., Zhang, B. C., and Byerlee, J., 1986, Effective pressure law for permeability of Westerly granite under cyclic loading: Journal of Geophysical Research: Solid Earth, v. 91, no. B3, p. 3870-3876.

Mourzenko, V. V., Thovert, J.-F., and Adler, P. M., 2011, Permeability of isotropic and anisotropic fracture networks, from the percolation threshold to very large densities: Physical Review, v. 84.

Mueller, S., Melnik, O., Spieler, O., Scheu, B., and Dingwell, D. B., 2005, Permeability and degassing of dome lavas undergoing rapid decompression: An experimental determination: Bulletin of Volcanology, v. 67, no. 6, p. 526-538.

Mueller, S., Scheu, B., Spieler, O., and Dingwell, D. B., 2008, Permeability control on magma fragmentation: Geology, v. 36, no. 5, p. 399-402.

Nakamura, M., Otaki, K., and Takeuchi, S., 2008, Permeability and pore-connectivity variation of pumices from a single pyroclastic flow eruption: Implications for partial fragmentation: Journal of Volcanology and Geothermal Research, v. 176, no. 2, p. 302-314.

Nara, Y., Meredith, P. G., Yoneda, T., and Kaneko, T., 2011, Influence of macro-fractures and micro-fractures on permeability and elastic wave velocities in basalt at elevated pressure: Tectonophysics, v. 503, p. 8.

Nasseri, M. H. B., Goodfellow, S. D., Lombos, L., and Young, R. P., 2014, 3-D transport and acoustic properties of Fontainebleau sandstone during true-triaxial deformation experiments: International Journal of Rock Mechanics and Mining Sciences, v. 69.

Neuberg, J. W., Tuffen, H., Collier, L., Green, D., Powell, T., and Dingwell, D., 2006, The trigger of low-frequency earthquakes on Monsterrat: Journal of Volcanology and Geothermal Research, v. 153, p. 14.

Nguyen, G. D., El-Zein, A., and Bennett, T., 2014, A conceptual approach to two-scale constitutive modelling for hydro-mechanical coupling, 7th International Congress on Environmental Geotechnics.

Nichols, A. R. L., Potuzak, M., and Dingwell, D. B., 2009, Cooling rates of basaltic hyaloclastites and pillow lava glasses from the HSDP2 drill core: Geochimica Et Cosmochimica Acta, v. 73, no. 4, p. 1052-1066.

Okumura, S., Nakamura, M., Nakano, T., Uesugi, K., and Tsuchiyama, A., 2010, Shear deformation experiments on vesicular rhyolite: Implications for brittle fracturing, degassing, and compaction of magmas in volcanic conduits: Journal of Geophysical Research: Solid Earth, v. 115, no. B6, p. n/a-n/a.

Olsen, M. P., Scholz, C. H., and Léger, A., 1998, Healing and sealing of a simulated fault gouge under hydrothermal conditions: Implications for fault healing: Journal of Geophysical Research: Solid Earth, v. 103, no. B4, p. 7421-7430.

Parry, W., 1998, Fault-fluid compositions from fluid-inclusion observations and solubilities of fracture-sealing minerals: Tectonophysics, v. 290, no. 1, p. 1-26.

Paterson, M. S., and Wong, T.-F., 2005, Experimental rock deformation - The brittle field, Springer-Verlag Berlin Heidelberg.

Phillips, J. C., Humphreys, M. C. S., Daniels, K. A., Brown, R. J., and Witham, F., 2013, The formation of columnar joints produced by cooling in basalt at Staffa, Scotland: Bulletin of Volcanology, v. 75, p. 17.

Potuzak, M., Nichols, A. R. L., Dingwell, D. B., and Clague, D. A., 2008, Hyperquenched volcanic glass from Loihi Seamount, Hawaii: Earth and Planetary Science Letters, v. 270, no. 1-2, p. 54-62.

Quane, S. L., Russell, J. K., and Friedlander, E. A., 2009, Time scales of compaction in volcanic systems: Geology, v. 37, no. 5, p. 5.

Rabbani, A., and Jamshidi, S., 2014, Specific surface and porosity relationship for sandstones for prediction of permeability: International Journal of Rock Mechanics and Mining Sciences, v. 71, p. 25-32.

Reid, M. E., 2004, Massive collapse of volcano edifices triggered by hydrothermal pressurization: Geology, v. 32, no. 5, p. 373-376.

Rieter, M., Barroll, M. W., Minier, J., and Clarkson, G., 1987, Thermomechanical model for incremental fracturing in lava flows: Tectonophysics, v. 142, p. 241-262.

Roedder, E., 1984, Volume 12: Fluid inclusions, Mineralogical Society of America, Reviews in mineralogy.

Rowland, J. V., and Simmons, S. F., 2012, Hydrologic, magmatic, and tectonic controls on hydrothermal flow, Taupo Volcanic Zone, New Zealand: implications for the formation of epithermal vein deposits: Economic Geology, v. 107, no. 3, p. 427-457.

Rust, A. C., Cashman, C., and Wallace, P. J., 2004, Magma degassing buffered by vapor flow through brecciated conduit margins: Geology, v. 32, no. 4, p. 4.

Rutqvist, J., 2015, Fractured rock stress-permeability relationships from in situ data and effects of temperature and chemical-mechanical couplings: Geofluids, v. 15, p. 19.

Ryan, M. P., and Sammis, C. G., 1981a, The glass-transition in basalt: Journal of Geophysical Research, v. 86, no. NB10, p. 9519-9535.

Ryan, M. P., and Sammis, C. G., 1981b, The glass transition in basalt: Journal of Geophysical Research, v. 86, no. B10, p. 17.

Saar, M. O., and Manga, M., 1999, Permeability-porosity relationship in vesicular basalts: Geophysical Research Letters, v. 26, no. 1, p. 111-114.

Saemundsson, K., 1970, Interglacial lava flows in the lowlands of southern Iceland and the problem of two-tiered columnar jointing: Jokull, v. 20, p. 62-77.

Sammis, C., and Ashby, M., 1986, The failure of brittle porous solids under compressive stress states: Acta Metallurgica, v. 34, no. 3, p. 511-526.

Saubin, E., Tuffen, H., Gurioli, L., Owen, J., Castro, J. M., Berlo, K., McGowan, E. M., Schipper, C. I., and Wehbe, K., 2016, Conduit dynamics in transitional rhyolitic activity recorded by tuffisite vein textures from the 2008–2009 Chaitén Eruption: Frontiers in Earth Science, v. 4, p. 59.

Schubnel, A., and Gueguen, Y., 2003, Dispersion and anisotropy of elastic waves in cracked rocks: Journal of Geophysical Research, v. 108.

Shen, B., Stephansson, O., Einstein, H. H., and Ghahreman, B., 1995, Coalescence of fractures under shear stresses in experiments: Journal of Geophysical Research: Solid Earth, v. 100, no. B4, p. 5975-5990.

Shields, J. K., Mader, H. M., Pistone, M., Caricchi, L., Floess, D., and Putlitz, B., 2014, Strain-induced outgassing of three-phase magmas during simple shear: Journal of Geophysical Research: Solid Earth, v. 119, no. 9, p. 6936-6957.

Sibson, R. H., 1994, Crustal stress, faulting and fluid flow, Geofluids: Origin, Migration and Evolution of Fluids in Sedimentary Basins, Volume 78, Special Publications Geological Society London, p. 16.

Sigmundsson, F., Hooper, A., Hreinsdóttir, S., Vogfjörd, K. S., Ófeigsson, B. G., Heimisson, E. R., Dumont, S., Parks, M., Spaans, K., and Gudmundsson, G. B., 2015, Segmented

lateral dyke growth in a rifting event at Bar [eth] arbunga volcanic system, Iceland: Nature, v. 517, no. 7533, p. 191-195.

Sigurdsson, H., Houghton, B., McNutt, S., Rymer, H., and Stix, J., 2015, The encyclopedia of volcanoes, Elsevier.

Simmons, G., and Cooper, H. W., 1978, Thermal cycling cracks in three igneous rocks: International Journal of Rock Mechanics and Mining Sciences, v. 15, p. 145-148.

Simpson, G., Guéguen, Y., and Schneider, F., 2001, Permeability enhancement due to microcrack dilatancy in the damage regime: Journal of Geophysical Research: Solid Earth, v. 106, no. B3, p. 3999-4016.

Smith, D. L., and Evans, B., 1984, Diffusional crack healing in quartz: Journal of Geophysical Research, v. 86, p. 11.

Spieler, O., Kennedy, B., Kueppers, U., Dingwell, D. B., Scheu, B., and Taddeucci, J., 2004, The fragmentation threshold of pyroclastic rocks: Earth and Planetary Science Letters, v. 226, no. 1-2, p. 139-148.

Spry, A., 1962, The origin of columnar jointing, particularly in basalt flows: Journal of the Geological Society of Australia, v. 8, no. 2, p. 27.

Sruoga, P., Rubinstein, N., and Hinterwimmer, G., 2004, Porosity and permeability in volcanic rocks: A case study on the Serie Tobífera, South Patagonia, Argentina: Journal of Volcanology and Geothermal Research, v. 132, no. 1, p. 31-43.

Stauffer, D., and Aharony, A., 1994, Introduction to Percolation theory, Taylor & Francis.

Sukop, M. C., Van Dijk, G.-J., Perfect, E., and Van Loon, W. K. P., 2002, Percolation thresholds in 2-Dimensional Prefractal models of porous medie: Transport in Porous Media, v. 48, p. 22.

Sun, W., Andrade, J. E., Rudnicki, J. W., and Eichhubl, P., 2011, Connecting microstructural attributes and permeability from 3D tomographic images of in situ shear-enhanced compaction bands using multiscale computations: Geophysical Research Letters, v. 38, no. 10.

Symons, D. T. A., 1967, Magnetic and petrologic properties of a basalt: Geophysical Journal of the Royal Astronomical Society, v. 12, no. 5, p. 473-&.

Tang, C., and Kou, S., 1998, Crack propagation and coalescence in brittle materials under compression: Engineering Fracture Mechanics, v. 61, no. 3, p. 311-324.

Tomkeieff, S. L., 1940, The basalt lavas of the Giant's Causeway district of northern Ireland: Bulletin of Volcanology, v. 6, p. 89-143.

Tuffen, H., and Dingwell, D., 2005, Fault textures in volcanic conduits: Evidence for seismic trigger mechanisms during silicic eruptions: Bulletin of Volcanology, v. 67, no. 4, p. 370-387.

Tuffen, H., Dingwell, D. B., and Pinkerton, H., 2003, Repeated fracture and healing of silicic magma generate flow banding and earthquakes?: Geology, v. 31, no. 12, p. 1089-1092.

Turcotte, D., 1982, Magma migration: Annual Review of Earth and Planetary Sciences, v. 10, no. 1, p. 397-408.

Turcotte, D. L., 1997, Fractals and chaos in geology and geophysics, Cambridge university press.

Vasseur, J., Wadsworth, F. B., Lavallée, Y., Bell, A. F., Main, I. G., and Dingwell, D. B., 2015, Heterogeneity: The key to failure forecasting: Scientific reports, v. 5.

Vasseur, J., Wadsworth, F. B., Lavallée, Y., Hess, K.-U., and Dingwell, D. B., 2013, Volcanic sintering: Timescales of viscous densification and strength recovery: Geophysical Research Letters, v. 40, no. 21, p. 5658-5664.

Vinciguerra, S., Trovato, C., Meredith, P. G., and Benson, P. M., 2005, Relating seismic velocities, thermal cracking and permeability in Mt. Etna and Iceland basalts: International Journal of Rock Mechanics and Mining Sciences, v. 42, no. 7-8, p. 900-910.

Wadsworth, F. B., Vasseur, J., Scheu, B., Kendrick, J. E., Lavallee, Y., and Dingwell, D. B., 2016, Universal scaling of fluid permeability during volcanic welding and sediment diagenesis: Geology, v. 44, no. 3, p. 4.

Wadsworth, F. B., Vasseur, J., von Aulock, F. W., Hess, K.-U., Scheu, B., Lavallée, Y., and Dingwell, D. B., 2014, Non-isothermal viscous sintering of volcanic ash: Journal of Geophysical Research: Solid Earth, v. 119, no. 12, p. 8792-8804.

Walsh, J. B., 1981, Effect of pore pressure and confining pressure on fracture permeability: International Journal of Rock Mechanics and Mining Sciences & Geomechanics Abstracts, v. 18, no. 5, p. 7.

Walsh, S. D. C., and Saar, M. O., 2008, Magma yield stress and permeability: Insights from multiphase percolation theory: Journal of Volcanology and Geothermal Research, v. 177, p. 88.

Wang, G., Mitchell, T. M., Meredith, P. G., Nara, Y., and Wu, Z., 2016, Influence of gouge thickness and grain size on permeability of macrofractured basalt: Solid Earth, v. 121, no. 12, p. 8472-8487.

Wannamaker, P. E., 2005, Anisotropy Versus Heterogeneity in Continental Solid Earth Electromagnetic Studies: Fundamental Response Characteristics and Implications for Physicochemical State: Surveys in Geophysics, v. 26, no. 6, p. 733-765.

Webb, S. L., and Dingwell, D. B., 1990, The Onset of Non-Newtonian Rheology of Silicate Melts: A fiber elongation study: Phys Chem Minerals, v. 17.

Wheeler, J., 2014, Dramatic effects of stress on metamorphic reactions: Geology, v. 42, no. 8, p. 647-650.

Whitaker, S., 1996, The Forchheimer equation: A theoretical development: Transport in Porous Media, v. 25, no. 1, p. 27-61.

Wiederhorn, S. M., Fett, T., Rizzi, G., Fuenfschilling, S., Hoffmann, M. J., and Guin, J. P., 2011, Effect of water penetration on the strength and toughness of silica glass: Journal of the American Ceramic Society, v. 94, no. s1.

Wong, T.-F., 1982, Effects of temperature and pressure on failure and post-failure behavior of Westerly granite: Mechanics of Materials, v. 1, no. 1, p. 3-17.

Wool, R. P., and O'Connor, K. M., 1981, A theory of crack healing in polymers: Journal of Applied Physics, v. 52, p. 11.

Wright, H. M. N., Cashman, K. V., Gottesfeld, E. H., and Roberts, J. J., 2009, Pore structure of volcanic clasts: Measurements of permeability and electrical conductivity: Earth and Planetary Science Letters, v. 280, no. 1-4, p. 93-104.

Wyering, L., Villeneuve, M., Kennedy, B., Gravley, D., and Siratovich, P., 2017, Using drilling and geological parameters to estimate rock strength in hydrothermally altered rock–A comparison of mechanical specific energy, R/NW/D chart and Alteration Strength Index: Geothermics, v. 69, p. 119-131.

Xu, T. F., Sonnenthal, E., Spycher, N., and Pruess, K., 2006, TOUGHREACT - A simulation program for non-isothermal multiphase reactive geochemical transport in variably saturated geologic media: Applications to geothermal injectivity and CO2 geological sequestration: Computers & Geosciences, v. 32, no. 2, p. 145-165.

Yanagidani, T., Sano, O., Terada, M., and Ito, I., 1978, The observation of cracks propagating in diametrically-compressed rocks: International Journal of Rock Mechanics and Mining Sciences, v. 15, p. 10.

Yasuhara, H., Elsworth, D., and Polak, A., 2004, Evolution of permeability in a natural fracture: Significant role of pressure solution: Journal of Geophysical Research: Solid Earth, v. 109, no. B3.

Yokoyama, T., and Takeuchi, S., 2009, Porosimetry of vesicular volcanic products by a water-expulsion method and the relationship of pore characteristics to permeability: Journal of Geophysical Research, v. 114, no. B2.

Yoshimura, S., and Nakamura, M., 2010a, Fracture healing in a magma: An experimental approach and implications for volcanic seismicity and degassing: Journal of Geophysical Research: Solid Earth, v. 115, no. B9.

Yoshimura, S., and Nakamura, M., 2010b, Fracture healing in a magma: An experimental approach and implications for volcanic seismicity and degassing: Journal of Geophysical Research-Solid Earth, v. 115.

Zhang, X., and Sanderson, D. J., 2002, Numerical Modelling and analysis of Fluid flow and deformation of fractured rock masses.

Zhang, Y., 1999, H_2O in rhyolitic glasses and melts: measurement, speciation, solubility, and diffusion: Reviews of Geophysics, v. 37, no. 4, p. 493-516.

Zhu, W., and Wong, T.-F., 1997, The transition from brittle faulting to cataclastic flow: Permeability evolution: Journal of Geophysical Research, v. 102, p. 15.
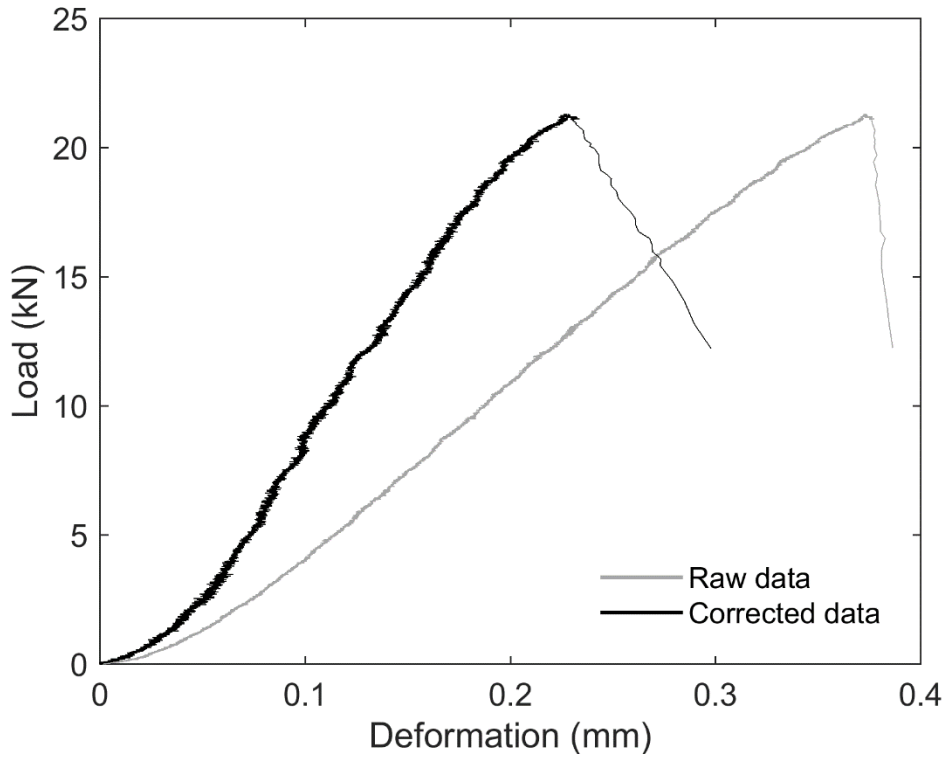
Appendix. I:

Loading column compliance determination

Accurate strain measurements during mechanical testing is essential and understanding how the loading column deforms at it applies stress to the sample is crucial. A compliance test aims at correcting for deformation occurring in the machine upon loading and consists of applying a constant load rate at any operating temperature while monitoring the deformation recorded by the LVDT. In this study, compliance tests were performed on the Instron® 8800 at room temperature between 0 and 60 kN and from 760 to 980 ℃ between 0 and 50 kN (Supplementary Fig. A. I-1) at a load rate of 5000 N.min^{-1}.
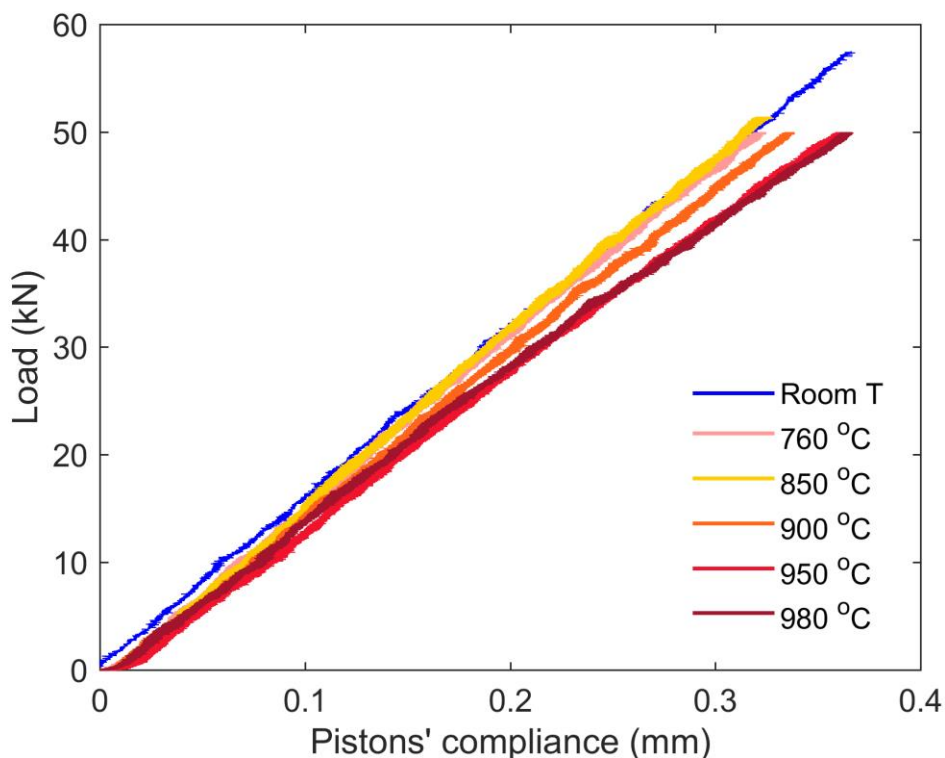
Supplementary Fig. A.I-1. Deformation in the loading column as the load is increased at different temperatures.

Once the deformation in the loading column is known, the instantaneous response of the pistons to the applied load can be removed from to that of the whole system (pistons and sample) to obtain the true deformation of the sample (Supplementary Fig A. I-2).

Supplementary Fig. A.I-2. Sample deformation without removing the deformation in the loading column (grey) and true sample deformation (black).

Appendix. II:

# The permeability of fractured rocks in pressurised volcanic and geothermal systems – Supplementary information

Supplementary Table A.II-1

Volcano	Bulk chemistry	Porosity range (%)	Age (yrs)	Sample name
Ceboruco, Mexico	Andesite	2-4	100-1000	CBD_0
		12-15	100-1000	CBD_9
		14	>1000	CBLF
		19-22	100-1000	CBD_19
		22-26	100-1000	CBD_6
		29-32	100-1000	CBD_7
		37-41	100-1000	CBD_10A
Colima, Mexico	Andesite	11-14	<100	COL_P2
		17-23	<100	COL_P21
Krafla, Iceland	Basalt	11	<100	KRA_BAS
Mount St Helens, USA	Dacite	9-12	<100	MSH_20
Pacaya, Guatemala	Basalt	6-9	>1000	PAC_L_SCARP
		12-14	<100	PAC_2010
		18-23	<100	PAC_BA
		24-30	<100	PAC_J13
Santiaguito, Guatemala	Andesite	19-21	<100	SGLF4
		35-41	<100	SGPF2

Supplementary Table A.II-1. Origin, bulk chemistry, porosity range and age of the samples used in this study. Porosity is given as a range when several samples (2 to 8) were cored and measured from the same rock.
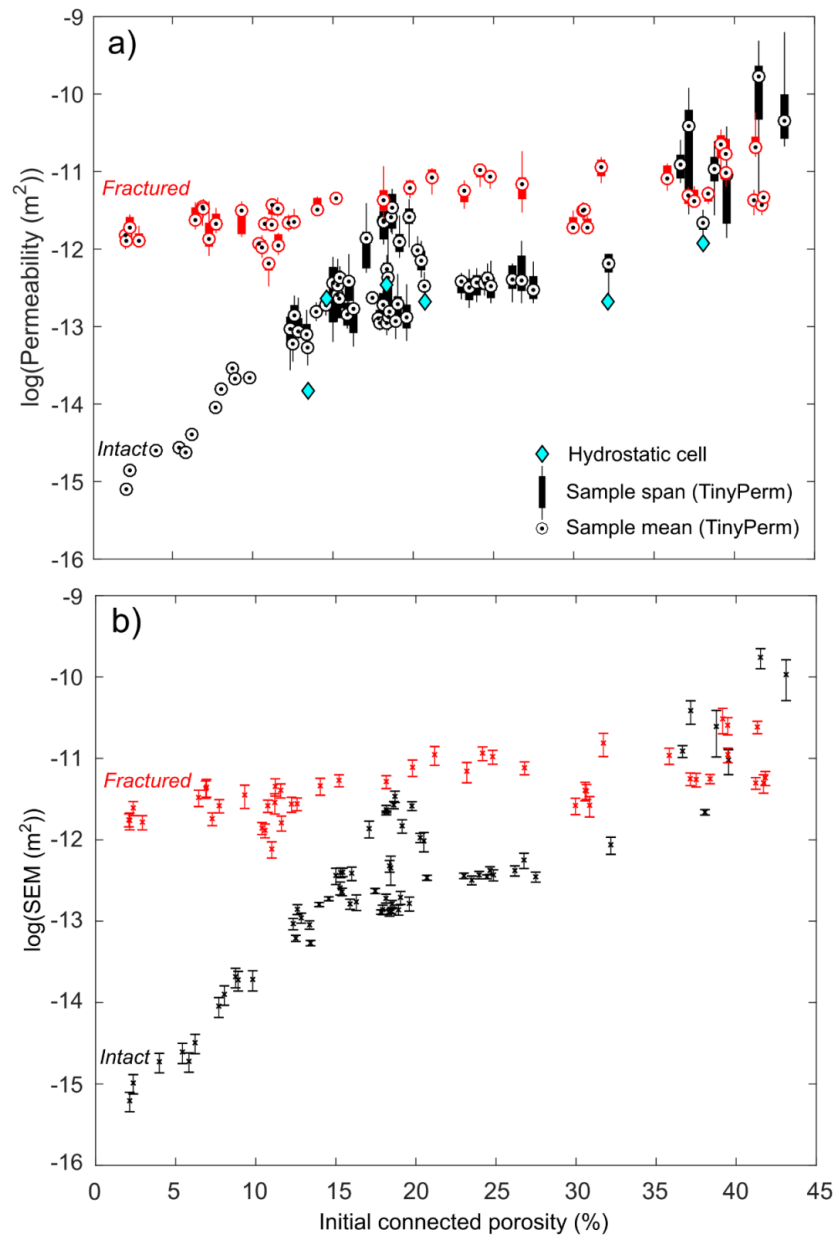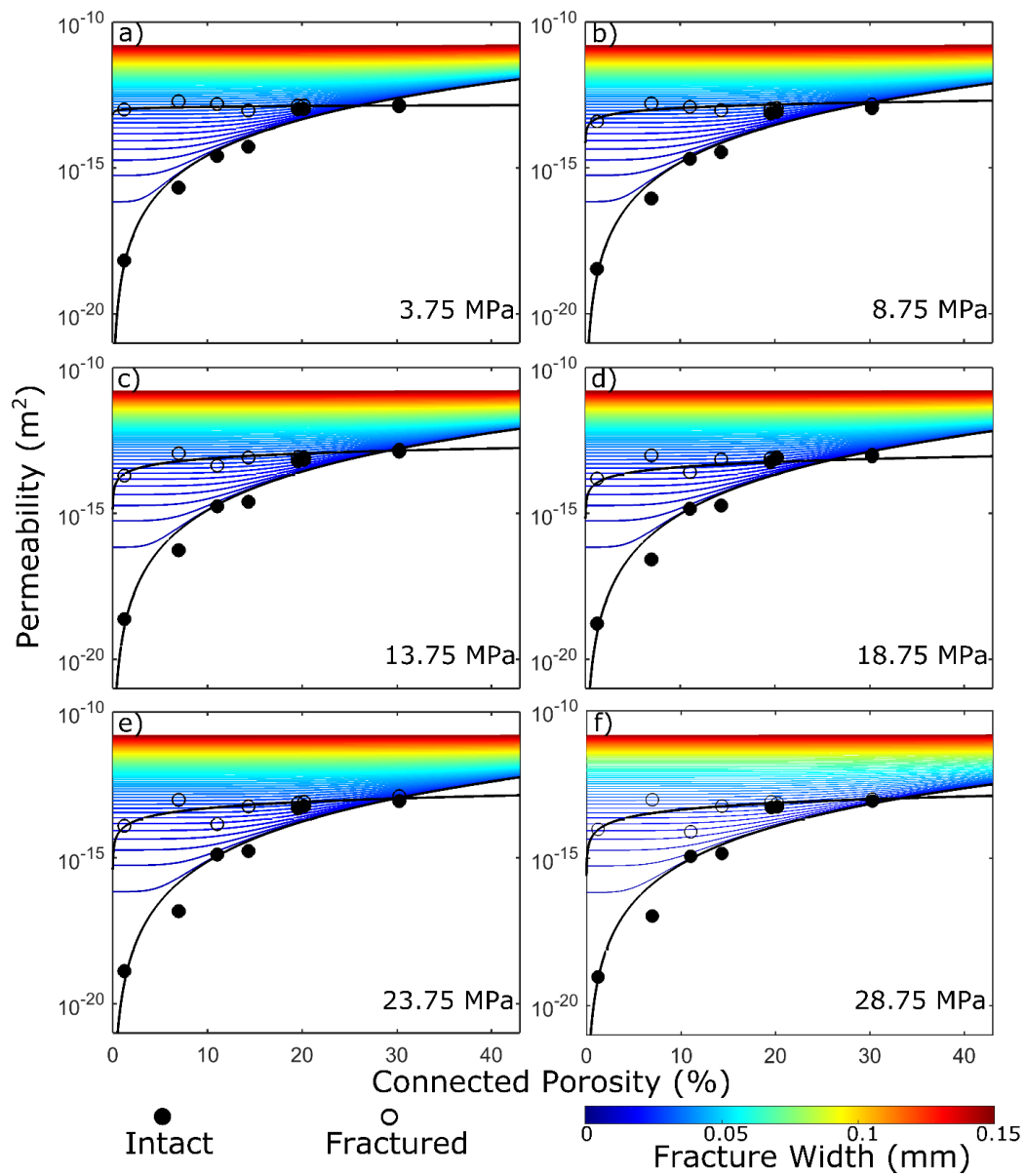
Supplementary Figure A.II-1
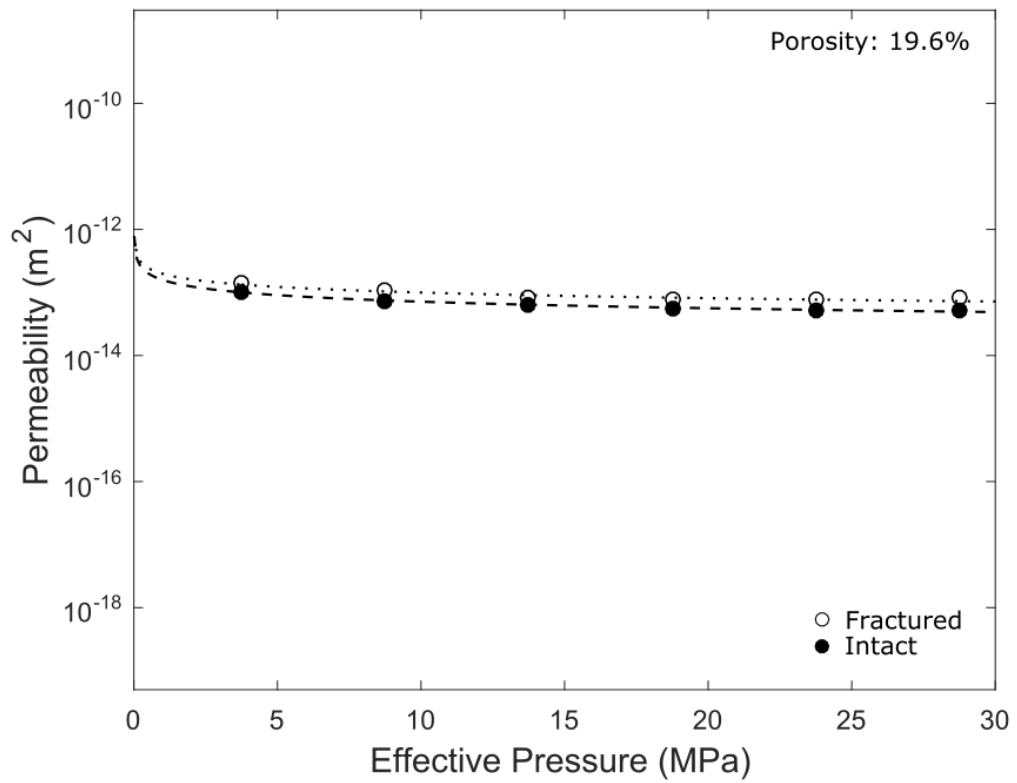
Supplementary Fig. A.II-1. Rock permeability as a function of effective pressure. The data show the relationship between permeability and effective pressure for the 19.6% porosity sample tested in the hydrostatic cell. The results for the intact and fractured sample show similar permeability-effective pressure relationships to those shown in Fig. 6-2e.

Supplementary Figure A.II-2

Supplementary Fig. A.II-2. a) Boxplot showing the span (boxes) and the mean permeability (dotted circles) of 111 samples measured with the TinyPerm. Note that black symbols show the reproducibility of the method on intact samples, while red symbols show measurement variability on fractured samples. Each box represents the span obtained from up to 10 repetitions on fractured and intact samples. Samples with porosity below 10% were measured 6 times due to their high reproducibility (span smaller than the mean symbol) and the time required for 1 measurement. The boxes indicate results within 1 standard deviation of the mean and lines show the 2nd to the 98th percentile of the distribution of measurements. **b)** Shows the Standard Error from the Mean (SEM) for each of the measurements.

Supplementary Fig. A.II-3. Permeability-porosity relationships (black lines) derived from fitting a least-squares function to the intact (solid circles) and fractured (open circles) samples measured in the hydrostatic pressure cell at different effective pressure steps (shown in panels **a-f**). Coloured lines represent the calculated fracture widths as a function of starting porosity, derived from eq. 4.6. (See Chapter 4. Analysis section). This demonstrates that increasing effective pressure reduces the fracture width, and hence permeability, across all starting porosities tested, although the influence is more pronounced at lower porosities.

Empirical solution for Equation 7

All data used to determine an empirical solution can be found in the attached files K_Peff_data.xls and w_Peff_data.xls

$$\kappa_s = \kappa_\Phi + \frac{\rho_f \overline{l} \overline{w}^3}{A_i} \qquad\qquad \text{(AII. S1)}$$

Equation 7 in the manuscript, that expresses the permeability evolution of a fractured system (κ_s) with effective pressure solvable, in terms of the intact rock permeability (κ_Φ), fracture density (ρ_f), average fracture length ($\overline{l}$) and width ($\overline{w}$) over an area of interest (A_i). Hence, equation 7 is solvable when the evolution of κ_Φ is known.

Our dataset however can provide an empirical solution to estimate permeability evolution of laboratory samples as a function of effective pressure and porosity from direct measurements. Furthermore using the fracture width modelling, our results can provide an approximation of fracture closure with depth, necessary to compute the fractured system permeability.

Despite physical modelling, this empirical solution relies on measured data and can aid with modelling the permeability evolution of porous media with depth as well as the impact of fractures on the same systems:

1. Least-squares functions for the permeability evolution of intact porous media and fracture closure as a function of effective pressure:

Peff (Pa)	κ_Φ	w
150000	$9.14 \times 10^{-18} \, \Phi^{3.16}$	$-4.17 \times 10^{-7} \Phi + 7.03 \times 10^{-5}$
3750000	$1.87 \times 10^{-18} \, \Phi^{4.03}$	$-2.48 \times 10^{-7} \Phi + 3.33 \times 10^{-5}$
8750000	$9.41 \times 10^{-18} \, \Phi^{4.15}$	$-4.10 \times 10^{-7} \Phi + 3.31 \times 10^{-5}$
13750000	$6.30 \times 10^{-20} \, \Phi^{4.20}$	$-4.09 \times 10^{-7} \Phi + 2.96 \times 10^{-5}$
18750000	$4.73 \times 10^{-20} \, \Phi^{4.21}$	$-4.29 \times 10^{-7} \Phi + 2.90 \times 10^{-5}$
23750000	$3.77 \times 10^{-20} \, \Phi^{4.17}$	$-4.44 \times 10^{-7} \Phi + 2.87 \times 10^{-5}$
28750000	$3.20 \times 10^{-20} \, \Phi^{4.29}$	$-5.15 \times 10^{-7} \Phi + 2.85 \times 10^{-5}$

Supplementary Table A.II-2. Permeability evolution of intact porous media (κ_Φ) and fracture width (w) with increasing effective pressure.

2. Determining empirical functions for the evolution of the different coefficients for intact rock permeability with effective pressure. (Data in K_Peff_data.xls: Tab Coefficients eq. det.)

The equations determining κ_Φ are all expressed as power laws ($a\ x^b$), with a and b respectively decreasing and increasing with effective pressure following these equations:

$$a = 2.93 \times 10^{-12} P_{eff}{}^{-1.07} \tag{AII. S2}$$

$$b = 1.64 P_{eff}{}^{0.06} \tag{AII. S3}$$

In these equations S2-3, the coefficients have different units: 2.93×10^{-12} m^2.Pa$^{1.07}$ and 1.64 Pa$^{0.06}$. Hence, the evolution of κ_Φ as function of porosity and effective pressure can be expressed by the empirical law:

$$\kappa_\Phi = \left(2.93 \times 10^{-12} P_{eff}{}^{-1.07}\right) \Phi^{\left(1.64 P_{eff}{}^{0.06}\right)} \tag{AII. S4}$$

Where P_{eff} is expressed in Pascals.

3. Determining empirical functions for the evolution of the different coefficients for fracture closure with effective pressure. (Data in w_Peff_data.xls: Tab Coefficients eq. det.)

Similarly, we can see that for each effective pressure tested, w follows a linear law ($c\,x + d$) as a function of porosity, where c expresses the fracture closure and d the fracture width for theoretical samples with 0 % porosity. The evolution of c across our range of porosities follows a second order polynomial function with increasing effective pressure, suggesting that the amount of closure with increasing effective pressure is more important at higher porosities. On the other, d shows a power law dependence with increasing effective pressure.

$$c = 2.33 \times 10^{-22} P_{eff}{}^2 - 2.67 \times 10^{15} P_{eff} + 3.39 \times 10^{-7} \tag{AII. S5}$$

$$d = 5 \times 10^{-4} P_{eff}{}^{-0.174} \tag{AII. S6}$$

In these equations S5-6, the coefficients have different units: 2.33×10^{-22} m.Pa^{-2}, 2.67×10^{-15} m.Pa^{-1}, 2.23×10^{-7} m, 5×10^{-4} m.Pa$^{0.174}$. The evolution of fracture width with increasing effective pressure can then be expressed as a function of porosity and effective pressure:

$$w = \left(2.33 \times 10^{-22}P_{eff}^{2} - 2.67 \times 10^{15}P_{eff} + 3.39 \times 10^{-7}\right)\Phi^{\left(5 \times 10^{-4}P_{eff}^{-0.174}\right)} \quad \text{(AII. S7)}$$

Considering a constant fracture length (in our case 0.0026 m), or a fracture aspect ratio (w/l), we can then empirically solve equation 7:

$$\kappa_s = \left(2.93 \times 10^{-12}P_{eff}^{-1.07}\right)\Phi^{\left(1.64P_{eff}^{0.06}\right)} +$$

$$\frac{\rho_f \times l \times \left[\left(2.33 \times 10^{-22}P_{eff}^{2} - 2.67 \times 10^{15}P_{eff} + 3.39 \times 10^{-7}\right)\Phi^{\left(5 \times 10^{-4}P_{eff}^{-0.174}\right)}\right]^3}{A_i} \quad \text{(AII. S8)}$$

Where A_i expresses the size of the pore pressure source and ρ_f is defined by:

$$\rho_f = \frac{\overline{lw}}{A_i} \quad \text{(AII. S9)}$$

This empirical formulation, allows resolution of the permeability evolution of a fractured porous medium with increasing effective pressure. We draw the reader's attention to the fact that by being empirical, this formulation, while providing a first order approximation of permeability, should be carefully tested and calibrated by changing experimental conditions.
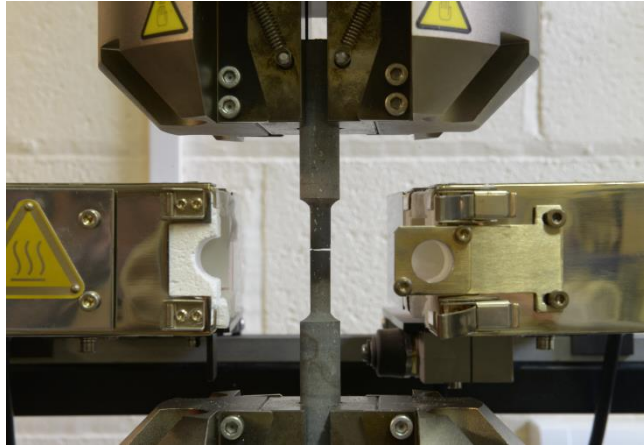
Appendix. III:

Disclosing the temperature for columnar jointing in lavas – Supplementary information

Method

A   B

Supplementary Fig. A.III-1. Photograph of experimental setup and sample assembly. A) The sample is mounted between two grips held in an Instron® 5969 uniaxial press (max. load 50 kN). The narrow central portion of the sample is enclosed in a Severn Thermal Solution split furnace housing a 16-mm diameter sapphire window to allow observation of cracking. B) Photograph of a post-experiment, jointed sample in the assembly (the split furnace is visible on each side of the sample).

Material
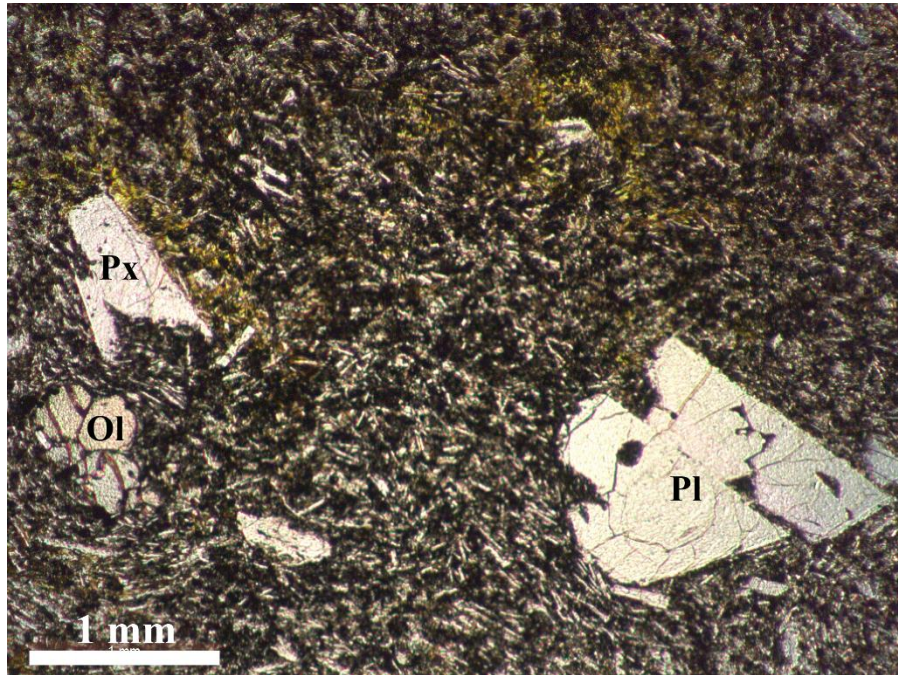
Supplementary Fig. A.III-2. Photomicrograph of the basalt from Seljavellir (Iceland), showing Olivine (Ol), Plagioclase (Pl) and Pyroxene (Px) crystals in a fine-grained groundmass containing plagioclase (light colour), pyroxene (dark grey) and iron oxides (black).

| Oxides	Abundance (wt.%)	Standard deviation
SiO_2	48.40	0.24
Al_2O_3	14.35	0.14
Fe_2O_3	14.60	0.15
MgO	4.58	0.05
CaO	9.12	0.09
Na_2O	3.81	0.04
K_2O	1.00	0.01
TiO_2	3.70	0.04
MnO	0.22	0.02
P_2O_5	0.59	0.06
SO_3	0.01	0.01
LOI	-0.69	0.001

Supplementary Table A.III-1. Bulk rock chemistry as obtained by x-ray fluorescence, performed at the University of Leicester (United Kingdom). LOI stands for loss on ignition and shows a minor weight gain associated with oxidation.

Brazilian tensile strength
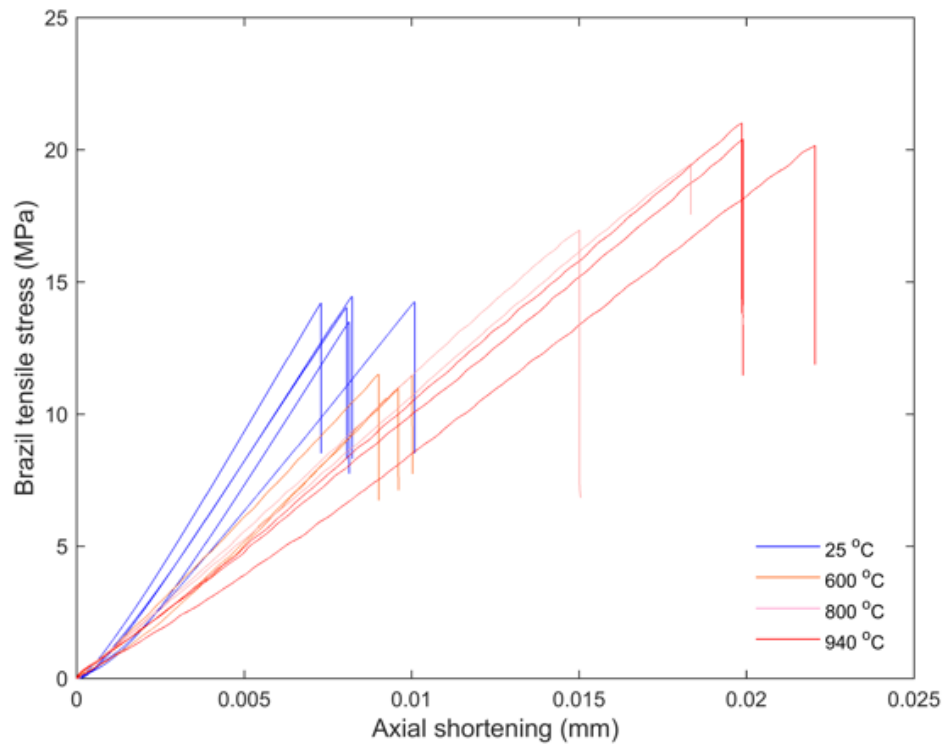
Supplementary Fig. A.III-3. Stress – axial shortening curves for Brazilian disc samples (40 mm diameter, 20 mm thickness) deformed diametrically at a rate of 0.4 mm.s^{-1} at room temperature (blue), 600 ºC (orange), 800 ºC (pink) and 940 ºC (red). The peak tensile stresses achieved determine lower (12 MPa) and upper (20 MPa) strength bounds for Seljavellir basalts.
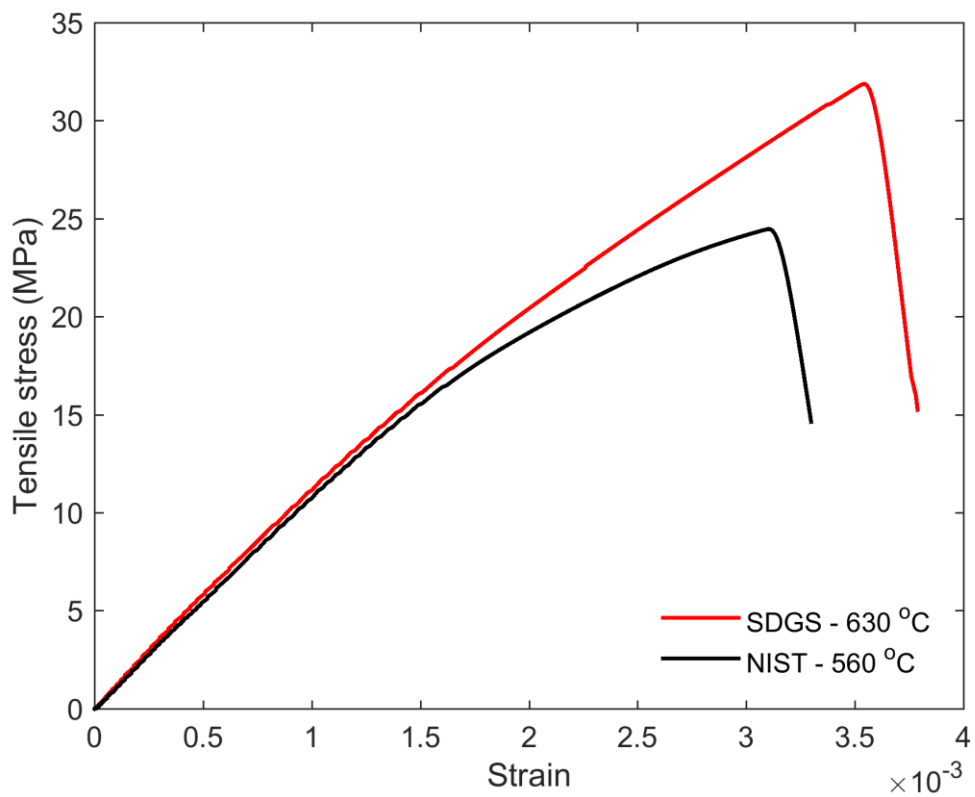
Permeability model
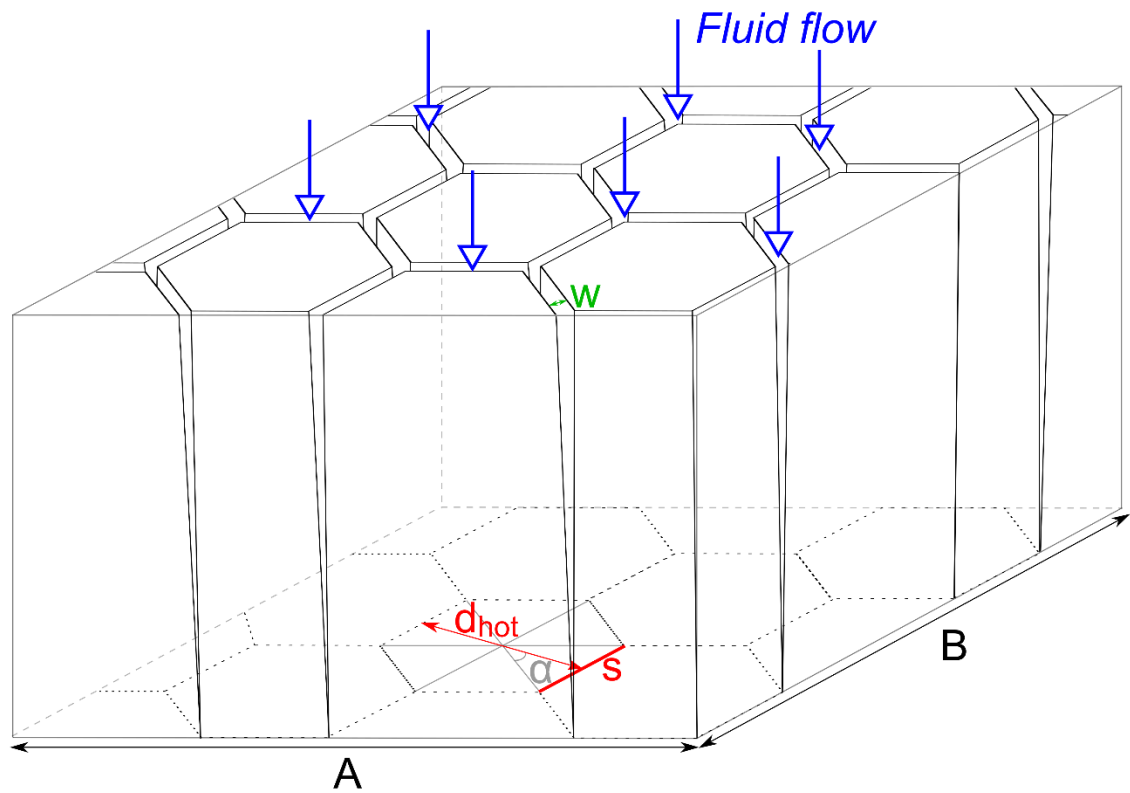
Supplementary Fig. A.III-4. Schematic depicting the different parameters used to model the permeability evolution with fracture width and cooling.

Appendix. IV:

Timescales of fracture healing and strength recovery in magmatic liquids – Supplementary information

INTACT GLASS SAMPLES TENSILE STRENGTHS

Supplementary Fig. A.IV-1. Tensile stress – strain curves for two intact glass samples. The red curve shows a maximum tensile strength of 32.2 MPa for the SDGS at 630 ºC, while the maximum tensile strength of the NIST reaches 25 MPa, as shown by the black line.